Transport and Separatrices in Time-Dependent Flows

Thesis by

Philip C. du Toit

In Partial Fulfillment of the Requirements

for the Degree of

Doctor of Philosophy

California Institute of Technology

Pasadena, California

2010

(Defended July 9, 2009)

To my parents,
Herman and Sandy,
for following a dream so that
their children could live theirs.

Acknowledgments

This thesis is written foremost with the intent to provide a meaningful contribution to the scientific community; but for the author, it also represents an opportunity to create a "scientific scrapbook" of all the beneficial and congenial collaborations I have enjoyed during my years of study at Caltech – and in many ways the writing of it is sweeter because of the friendships found and enjoyed during the development of the scientific results.

The most significant and cherished influence over my studies has been the kind and gentle tutoring of Dr. Jerrold Marsden. I have learned during my travels to conferences worldwide, that when I introduce myself as a student of Dr. Marsden, I am immediately afforded friendship and respect far beyond that merited by my contributions or virtues of character. Indeed, I feel that regardless of my future achievements, my greatest career honor, and the honor that I can reflect upon with the warmest of memories, will be to say: "I was a student of Dr. Jerry Marsden."

The opportunity to learn from Dr. Marsden (as well as from his amiable collaborators - a veritable School of Athens!) is personally exhilirating. Dr. Marsden's breadth of insight and contributions, and his willingness to share these with students, are rare in a scientific community where research is evermore narrowed, splintered, and hurried; and, in my opinion, place him in company with the great Fathers of our field. In my mind's eye, I can imagine in the world of sprits "across the bar," a salon frequented by Euler, Poincaré, Lie, Hamilton, Whittaker, Jacobi, and Cartan, where they are all seated around a table discussing and comparing, all the while leaving a chair open for Jerry Marsden. We all hope and trust that they will have to wait many more years yet, before he will have the opportunity to join them!

Wherever Jerry Marsden is, one will find Wendy McKay making sure that everything is running perfectly. I thank Wendy for all her help in making it possible for us to occupy our minds entirely with science, and to forget all the details of planning and organization.

The work of this thesis could not have been possible without the assistance and collaboration of many scientists. Yi Chao, Igor Schulman, and Peirre Lermusiaux were all very helpful in formatting and providing data from their respective ocean models. Claire Newman provided wind model data for the atmosphere of Titan, and Shuyi Chen provided wind velocity data from her high-resolution hurricane models. Velocity data for the global ocean was kindly provided by the Mercator global ocean modeling project. Bob Ecke generously shared data from his laboratory experiments for the work on overflows in the North Atlantic scarcely minutes after our first acquaintence. I also thank Mark Petersen and Beth Wingate for providing data from the Antarctic Circumpolar Current channel model, and for their interest in making connections within the oceanographic community. Igor Mezić provided many helpful discussions with regard to the work on coupled oscillator models. I have also benefitted from collaboration with Alina Chertock, Jose Miguel Pasini, Sujit Nair, Katalin Grubits, and Marin Kobilarov on research topics not covered in this thesis.

Shawn Shadden, a former student of Dr. Marsden, provided helpful discussions as well as encouraging support from a student's perspective.

I have been fortunate to be joined by talented undergraduate students during summer research projects including Evan Gawlik, who provided excellent work on the elliptic three-body problem, and Benjamin Bastide, who worked with me during our first discoveries of homoclinic tangles in hurricanes.

Tapio Schneider kindly provided access to the supercomputer in the Division of Geological and Planetary Sciences at Caltech, without which the computations would not have been practicable. I thank Aaron Mckinnon and Naveed Near-Ansari for their instant computer support – especially on late nights and weekends.

I also thank Tony Bloch for his mentorship during my studies at the University of Michigan, and Peter Smereka for first introducing me to the Smale horseshoe.

During my graduate studies, I have received generous funding from DARPA, the National Science Foundation, the Office of Naval Research, the Air Force Office of Scientific Research, the ARCS Foundation, the Society for Industrial and Applied Mathematics, the Center for the Mathematics of Information, and the Office of the Dean of Graduate Studies at Caltech through various funded projects and awards.

Most importantly, I wish to thank my wife, Patricia, for her love, support, and encouragement. As Mother to our four boys, she has performed far more difficult, rigorous, noble, and rewarding work than any of the challenges I have faced in my research – and in a far more loving way!

If there are mistakes in this thesis, they are of my own imagination. From the long list of acknowledgments, it is easy to see that if there is anything of great scientific value contained herein, that these results have come through me, and not because of me.

Abstract

The method of using Finite Time Liapunov Exponents (FTLE) to extract Lagrangian Coherent Structures (LCS) in aperiodic flows, as originally developed by Haller, is applied to geophysical flows, and flows in the phase space of second order dynamical systems. In this approach, the LCS are identified as surfaces of greatest separation that parse the flow into regions with different dynamical behavior. In this way, the LCS reveal the underlying skeleton of turbulence. The time-dependence of the LCS provides insight into the mechanisms by which fluid is transported from one region to another. Of especial interest in this study, is the utility with which the FTLE-LCS method can be used to reveal homoclinic and horseshoe dynamics in aperiodic flows.

The FTLE-LCS method is applied to turbulent flow in hurricanes and reveals LCS that delineate sharp boundaries to a storm. Moreover, intersections of the LCS define lobes that mediate transport into and out of a storm through the action of homoclinic lobe dynamics. Using FTLE-LCS, the same homoclinic structures are seen to be a dominant transport mechanism in the Global Ocean, and provide insights into the role of mesoscale eddies in enhancing lateral mixing.

Beyond geophysical flows, we also study transport in the phase space of a coupled oscillator model for biomolecules. Before we can analyze transport in this model, we first introduce an appropriate model reduction that captures the relevant statistics of the full system. In the reduced model, we see that transport is again mediated by the process of horseshoe dynamics in a perturbed homoclinic tangle.

We also consider some theoretical aspects of FTLE-LCS, including the relationship between LCS and stable/unstable manifolds, the invariance of LCS, and the possibility of an evolution equation describing the motion of the LCS. A parallelized

software for computing FTLE is also introduced.

Contents

Chapter 1

Introduction

This thesis investigates flows defined by the system of ordinary differential equations,

$$\dot{\mathbf{x}}(t) = \mathbf{f}(\mathbf{x}(t), t)\,. \tag{1.1}$$

The flows to be studied arise in a wide array of applications. Of particular interest in this work are geophysical fluid flows including global oceanic circulation, and the intense atmospheric flows of hurricanes. We shall also study flow generated in the phase space of a second order dynamical system, such as three bodies under mutual gravitational attraction, or a chain of coupled oscillators.

The approach will be geometric and qualitative. We are not so concerned about the motion or accurate description of an individual trajectory, as we are about uncovering global structures that govern the motion of entire regions in the flow.

In satelite imagery of geophysical fluid flows, it is plain to see that, despite the manifestly turbulent flow of the ocean and atmosphere, large-scale coherent structures are present – the imagery of hurricanes in the Atlantic being a declarative case in point. The visual evidence for coherent structures begs for a deeper understanding of their dynamical properties. How should these coherent structures be described from a dynamical systems perspective? Given that the imagery of intense cloud bands indicates the presence of a hurricane, what are the corresponding structures in the underlying velocity field that delineate the hurricane's dynamical structure? Can we uncover structures in the flow that define the mechanisms by which fluid is transported

in and around the hurricane? For aperiodic flows, even the simplest of questions can have ill-defined answers. For example, "How do we define the dynamically relevant boundary of a hurricane?".

These questions can be applied equally well to eddies in the global ocean. Important questions that are not yet well-understood by the oceanography community include: "What process controls the rate of mixing at the ocean surface?", and "Why are eddies leaky?" Nascent Lagrangian analysis of ocean flows is starting to yield answers; however, the studies most commonly involve direct visualization of tracer trajectories. Nevertheless, the insight that Lagrangian descriptions provide is now more widely recognized, and experiments are underway to directly observe Lagrangian evolution of dye patches and regularly spaced grids of drifters in the ocean in order to uncover the important dynamic transport structures.

Over the last several years, varied techniques have been developed within the dynamical systems community to study coherent structures in aperiodic flows. The underlying goal of these methods is to identify key structures within the flow that govern transport and mixing. For the purposes of the present study, we will adopt the FTLE-LCS method first proposed by [Haller 2000, Haller 2001], which uses Finite Time Liapunov Exponents (FTLE) to identify Lagrangian Coherent Structures (LCS). A precise definition of the method and an initial discussion of the properties of the LCS is provided by [Shadden 2005] and [Lekien 2007].

The underlying premise of the FTLE-LCS approach is that coherent structures in a flow are best represented by visualizing the surfaces of greatest separation. Defined in this way, the LCS act as barriers to transport, and parse the flow into regions with different dynamical behavior and outcomes. Most important for our purposes, the motion of the time-dependent LCS reveals the mechanisms that mediate transport from one region of the flow to another. The method has several variants, including the Finite Size Liapunov Exponent (FSLE) approach [Aurell 1997, d'Ovidio 2004], but all are in the same spirit. A different method, that is not used in this thesis, is the Distinguished Hyperbolic Trajectory approach, which identifies coherent structures as the most hyperbolic trajectories emanating from "instantaneous stagnation points"

[Ide 2002].

The utility of the FTLE-LCS method lies in the fact that it can be applied without impediment to flows with arbitrary time-dependence. The flows in question may arise from an analytical model, or a finite data set of discrete flow data originating from a numerical simulation (a direct simulation of Navier-Stokes equation, for example), or from observations of the flow (such as radar measurements of ocean surface currents) that may be interpolated to determine the velocity field during the period of interest.

The number of applications to which the FTLE-LCS method is now being applied is steadily increasing. Recent studies include bio-mechanics [Shadden 2008, Tanaka 2008], bio-locomotion[Shadden 2007, Peng 2009], laboratory flows, naval search and rescue, and oil spill mitigation.

The overarching advantage of the FTLE-LCS method is that it systematically and succinctly encodes Lagrangian data into a single visualization. Whereas human temporal perception struggles with untangling chaotic trajectories in a turbulent flow, the FTLE-LCS presents the same Lagrangian information in a single intuitive image. Without access to the FTLE, researchers are often tempted to use the Eulerian velocity field, or streamlines to determine coherent structures; however, this yields very little insight into Lagrangian transport mechanisms, and can often lead to erroneous conclusions about flow structure (the time-dependence plays havoc with Eulerian conclusions!). Furthermore, an attempt to uncover Lagrangian information about the flow by simply integrating particle trajectories at different locations and times very quickly leads to "spaghetti" plots that are also not helpful. In contrast, the LCS method provides a systematic and concise approach for analyzing aperiodic flows and extracting the coherent structures that govern transport.

1.1 Main contributions of this thesis

This thesis continues the development of the FTLE-LCS method for studying aperiodic flows. In summary, the main contributions are as follows:

- The FTLE-LCS method is applied to several example flows yielding insight into

the major structures that guide transport. The example flows include coastal oceans, planetary atmospheres, laboratory flows, and the three-body problem. (Chapter 3)

- The FTLE-LCS method is used to demonstrate that homoclinic tangles and the attendant transport mechanism of 'lobe dynamics' are a dominant transport structure in *aperiodic* geophysical flows – most notably in hurricanes, and mesoscale ocean eddies. (Chapters 5, 6, and 7).

- A study of global conformation change in a system of coupled oscillators provides a method for model reduction so that the statistics of the full system with many degrees of freedom are adequately described by a reduced system with one and a half degrees of freedom. (Chapter 8).

- The structures that govern transport from one conformation to another in the previously mentioned coupled oscillator model are visualized using surfaces of greatest separation (a slight modification of the FTLE-LCS method) and provides the appropriate reduced coordinates in which to reveal the presence of lobe dynamics and a homoclinic tangle in the high-dimensional flow. (Chapter 8).

- A study is made of the relationship between FTLE-LCS and stable/unstable manifolds of classical dynamical systems theory. A criterion is proposed for determining when FTLE-LCS and stable/unstable manifolds coincide. (Chapter 9).

- An algorithm is provided for determining evolution equations for the LCS. In light of this result, the motion of the LCS can be thought of as 'deterministic' (the result of an underlying evolution equation written in terms of the given velocity field), rather than 'emergent' (the result of extracting the LCS motion from multiple visualization frames in time). (Chapter 9).

- Software has been developed for large-scale computations of FTLE in flows

of any dimension on parallel processors at unprecedented resolution. The software provides many features especially designed for analyzing geophysical flows. (Chapter 10).

1.2 Research topics not covered in this thesis

The central penetrating theme of this thesis is the discovery of transport mechanisms, and in particular the homoclinic tangle, in aperiodic flows. The author's research interests, however, are not as narrowly defined, and during my graduate research, I have pursued several unrelated research areas. A brief summary of this research that is not included in the body of the thesis is presented here.

1.2.1 Fast parallelized particle methods for PDEs

A particle method is developed for obtaining numerical solutions of the EPDiff-equation – the Euler-Poincaré equation associated with the diffeomorphism group [Chertock 2009]. For vectors in $\mathbb{R}^n$, the EPDiff-equation is

$$\frac{\partial \mathbf{m}}{\partial t} + \mathbf{u} \cdot \nabla \mathbf{m} + \nabla \mathbf{u}^T \cdot \mathbf{m} + \mathbf{m}(\operatorname{div} \mathbf{u}) = 0. \tag{1.2}$$

Here the momentum $\mathbf{m}$ and velocity $\mathbf{u}$ are vector functions of space and time, and are related by the second-order Helmholtz operator,

$$\mathbf{m} = \mathbf{u} - \alpha^2 \Delta \mathbf{u}, \tag{1.3}$$

where α is a constant parameter. As shown in [Holm 2005], the particle approach reduces the partial differential equation to a finite-dimensional Hamiltonian system that can be implemented with geometry-preserving integrators that respect the symmetries of the particle system. The particle method is efficiently implemented on a parallel computing cluster using a spatial decomposition method that scales linearly with the number of particles. As depicted in Figure 1.1(a), the extremely low

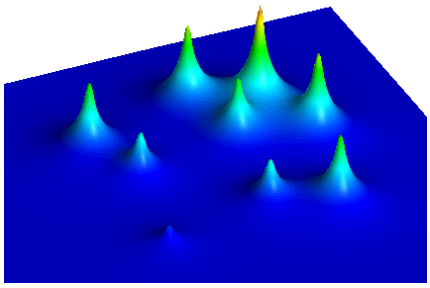

(a) Nonlinear interactions between peakons in the EPDiff-equation are simulated using an efficient particle method.

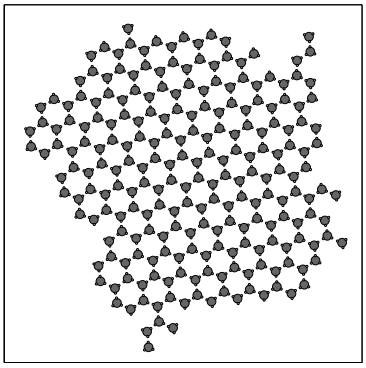

(b) An interaction potential is designed so that a honeycomb lattice forms via self-assembly as the system of particles is cooled.

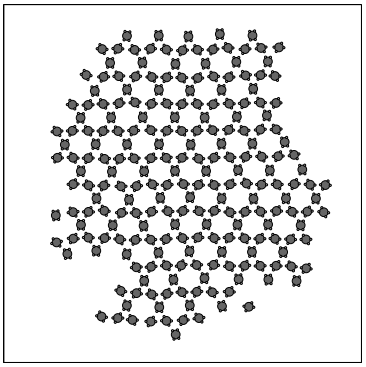

(c) The use of anisotropic potentials allows for the formation of the kagome lattice.

(d) Underactuated vehicles with uncertain sensors perform a coordinated search over complex terrain.

Figure 1.1: Some of the applications addressed in my current research.

numerical diffusion of the particle method allows for sharp reproduction of *peakon* solutions, as well as interesting nonlinear *peakon-peakon* interactions. *Peakons* are solitary traveling wave solutions that are distinguished from soliton solutions by a discontinuity in their derivative that leads to a sharp peak at the crest of the wave.

1.2.2 Self-Assembly by design

Self-Assembly is the process by which constituents organize *themselves* into a globally ordered configuration without the influence of external factors [Whitesides 2002]. Order in the global superstructure is predicated on the local interactions between the individual constituents. Studies of self-assembly have typically examined the types of ordered superstructures that arise from a given fixed interaction potential; however, recent interest in fabrication of nanomaterials and photonic crystals with desired material properties motivates the inverse problem: *design* the short-range interaction in order to induce self-assembly of the components into a target lattice structure. We consider the specific problem of designing short-range pairwise interaction potentials between particles on a planar surface so that the particles self-assemble into a desired lattice.

New methods (a fast geometric method as well as a robust trend optimization method based on the rigorous Surrogate Management Framework [Booker 1999]) have been developed for the design of isotropic interaction potentials that lead to the formation of high quality honeycomb lattices as the system of particles is cooled (as shown in Figure 1.1(b)) [Du Toit 2009b]. The geometric method is also extended to the case of anisotropic potentials which allow for the formation of the more exotic kagome lattice (Figure 1.1(c)).

1.2.3 Coordinated Search with under-actuated vehicles

Motivated by recent advancements in unmanned aerial vehicles, we have considered the problem of using multiple vehicles equipped with sensors to find a target in a large complex terrain. An important feature of the problem description is that the vehicles

are modeled as rigid bodies with *under-actuated* helicopter dynamics and limited control authority, and that the sensors are uncertain with probabilities for both missed detection and false alarm (Figure 1.1(d)). Hence, there is strong coupling between the vehicle dynamics and the design of the search strategy to be employed. We have developed a framework for vehicle control that uses motion primitives to dynamically generate trajectories that are consistent with the under-actuated dynamics of the search vehicle. The vehicle trajectories are updated dynamically as the sensors receive measurements using a Bayesian scheme to locally maximize the likelihood of target detection [Du Toit 2009c]. The algorithm is robust to changes in the terrain, limited communication range, and vehicle failure.

Chapter 2

Homoclinic Points and the Horseshoe Map - A Reprise

As mentioned in the introduction, a central contribution of this thesis is the identification and visualization of *homoclinic tangles* and *horseshoes* in turbulent geophysical flows. This chapter provides an overview of the theoretical development of homoclinic and horseshoe dynamics. To this end, this chapter will not provide new results, but will rather furnish the mathematical setting and context for results that follow in later chapters.

Beyond simply providing background information, a review of this mathematical foundation will aid in identifying and appreciating the structures that will be subsequently demonstrated for turbulent flows in the ocean and atmosphere. Emphasis will be placed on the contributions of Poincaré and Smale; although, as will be seen, there are many participants, each of whose contributions are interwoven to produce a delightful panorama of mathematics. The narrative of the mathematical results will be historical in nature – the historical development of the ideas is too rich a story not to tell, and the appreciation of which heightens understanding of the main results.

A further reason for providing this introductory survey of homoclinic and horseshoe dynamics is to ensure that this thesis is self-contained and accessible to a broad audience of oceanographers and atmospheric scientists. For more mathematical details, the reader is directed to the texts of [Guckenheimer 1983] and [Wiggins 2003]. An excellent mathematical overview is provided in the survey of [Holmes 1990], and

the discussion here follows a similar progression of ideas. A detailed mathematical account from a historical perspective is provided by [Barrow-Green 1996] (also see the less technical account of [Szpiro 2007]). Of course, greatest appreciation for the beauty of these ideas is best obtained by studying the primary texts of [Poincaré 1899] and [Smale 1967].

This chapter will also help to provide definitions and notation that will be used uniformly throughout the thesis.

2.1 Poincaré and homoclinic points

The mathematical contribution of Poincaré that will concern us most in the present treatise is the discovery of homoclinic points and asymptotic solutions – a theory he developed during his study of the restricted three-body problem. Poincaré used a geometric and qualitative approach. In the introduction to his original memoir, he instructs his readers that [Barrow-Green 1996]:

> These theorems have been given in a geometric form which has to my eyes the advantage of making clearer the origin of my ideas ...

Poincaré's approach signaled the birth of geometric mechanics, and his initial exposition would be extended by the topological approach to dynamics of Birkhoff and Smale.

First we demonstrate the method Poincaré used to reduce a two-degree of freedom Hamiltonian system to a time-dependent Hamiltonian system with a single degree of freedom. The procedure uses two main ingredients: (1) the Hamiltonian integral, and (2) the replacement of time by a time-like coordinate. The particulars of the restricted three-body problem addressed by Poincaré are not essential to our purpose, and consequently we shall omit details and consider a general Hamiltonian system (see [Szebehely 1967] for a detailed treatment of the restricted three-body problem).

Consider the time-independent Hamiltonian of a system with two degrees of freedom:

$$H(q_1, q_2, p_1, p_2)\,. \tag{2.1}$$

Hamilton's equations of motion are

$$\dot{q}_1 = \frac{\partial H}{\partial p_1} \qquad\qquad \dot{p}_1 = -\frac{\partial H}{\partial q_2} \tag{2.2}$$

$$\dot{q}_2 = \frac{\partial H}{\partial p_2} \qquad\qquad \dot{p}_2 = -\frac{\partial H}{\partial q_2}\,. \tag{2.3}$$

The derivative of the Hamiltonian with respect to time is:

$$\frac{dH}{dt} = \frac{\partial H}{\partial q_1}\dot{q}_1 + \frac{\partial H}{\partial q_2}\dot{q}_2 + \frac{\partial H}{\partial p_1}\dot{p}_1 + \frac{\partial H}{\partial p_2}\dot{p}_2 = 0\,, \tag{2.4}$$

so that we may immediately conclude that the Hamiltonian is constant:

$$H(q_1, q_2, p_1, p_2) = h = \text{constant}\,. \tag{2.5}$$

The availability of this integral relationship implies that we can solve for one of the coordinates as a function of the remaining three coordinates and the constant h. That is,

$$p_1 = p_1(q_1, q_2, p_2; h)\,. \tag{2.6}$$

Our next step is to replace time by another of the coordinates, q_1. In this way, the coordinate q_1 becomes an independent time-like variable. In doing so, we lose the true time parameterization of the trajectories and retain only the geometry of the solution – the time parameterization can always be reconstructed after solving the reduced system.

Using the identities:

$$\dot{q}_2 = \frac{dq_2}{dq_1}\dot{q}_1\,, \qquad \dot{q}_2 = \frac{\partial H}{\partial p_2}\,, \quad \text{and} \quad \dot{q}_1 = \frac{\partial H}{\partial p_1}\,, \tag{2.7}$$

we can write

$$\frac{dq_2}{dq_1} = \frac{\frac{\partial H}{\partial p_2}}{\frac{\partial H}{\partial p_1}}\,, \tag{2.8}$$

so that time has been eliminated in favor of the new independent variable q_1.

Likewise,

$$\frac{dp_2}{dq_1} = -\frac{\frac{\partial H}{\partial q_2}}{\frac{\partial H}{\partial p_1}}\,. \tag{2.9}$$

When evaluating the partial derivatives of H in the right-hand sides of (2.8) and (2.9), we use the expression for p_1 in (2.6) to write the result entirely in terms of the dependent variables q_2 and p_2, the independent variable q_1, and the constant h. Thus, the original Hamiltonian system has been reduced to

$$\frac{dq_2}{dq_1} = f(q_2, p_2; q_1; h) \tag{2.10}$$

$$\frac{dp_2}{dq_1} = g(q_2, p_2; q_1; h)\,, \tag{2.11}$$

a q_1-dependent (think, "time"-dependent), *single* degree of freedom system. What is more, the new system is in fact Hamiltonian, with the q_1-dependent Hamiltonian,

$$\bar{H} := -p_1(q_2, p_2; q_1; h)\,. \tag{2.12}$$

After solving this reduced Hamiltonian system, the full solution can be reproduced by chasing back up through the definitions.

In the restricted three-body problem, Poincaré chose an appropriate change of variables so that the q_1 coordinate corresponded to an angle variable with period 2π. Hence, the problem was reduced to a single degree of freedom Hamiltonian system

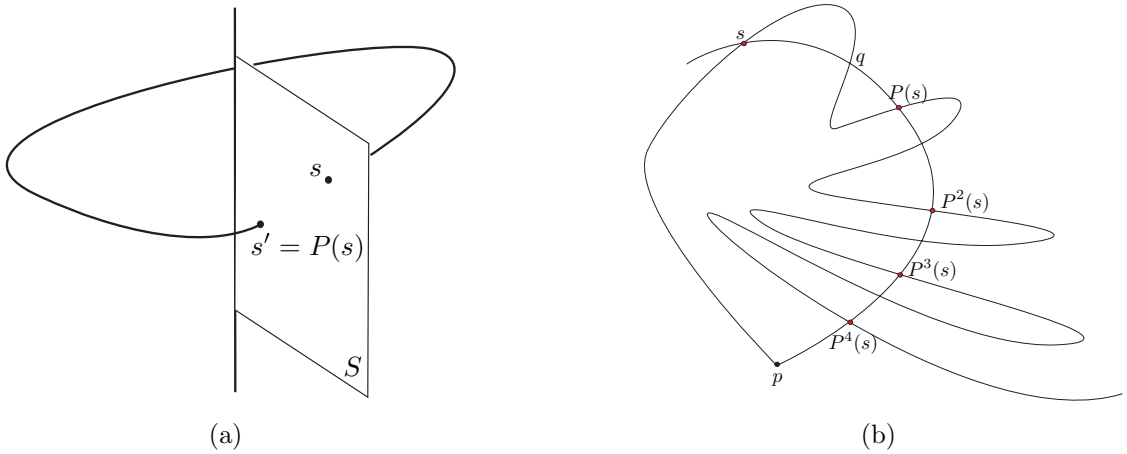

Figure 2.1: (a) The flow of the reduced Hamiltonian, $\bar{H}$, induces a discrete map, $P : S \to S$, on the Poincaré section, S. (b) Intersections of the stable and unstable manifolds of the fixed point p on the Poincaré section S.

with periodic forcing. Many of the examples that we shall encounter in later chapters will be of this form.

The q_1-dependence of the reduced Hamiltonian implies that when viewed in the (q_2, p_2)-plane, trajectories may intersect, and consequently precludes a qualitative geometric analysis. Poincaré's insight was to reduce the system even further to remove the intersections and provide a clearer picture.

In the three-dimensional $(q_2, p_2; q_1)$-space, he introduced a two-dimensional cross-sectional surface, S, (now called a *Poincaré section*) defined by the plane $q_1 = 0$, such that all trajectories pass transversally through the surface. The transverse intersection of a trajectory with S defines a point $s \in S$. Since the system is periodic in q_1, the trajectory returns to the surface S at a point s' after time 2π. In this way, a study of the flow of the dynamical system under the reduced Hamiltonian $\bar{H}$, reduces to a study of a discrete *Poincaré map*, $P : S \to S$, as illustrated in Figure 2.1(a).

Poincaré referred to the locations of forward iterations of the map as *consequents*, and to the locations of iterations of the inverse map, $P^{-1} : S \to S$, as *antecedents*.

If $\bar{H}$ is smooth, then P will be an orientation-preserving map. Furthermore, since the flow under $\bar{H}$ is Hamiltonian and preserves volume, the map P will preserve area.

A *fixed point* of the map $P : S \to S$ is a point $p \in S$ such that $P(p) = p$. Clearly, a fixed point on S corresponds to a periodic trajectory in $(q_2, p_2; q_1)$-space. Just as with fixed points in continuous dynamical systems, we can investigate the *stability* of p under iterations of the map. To do so, we first compute the *linearization* of the map P at p:

$$s \to DP(p) \cdot s\,, \tag{2.13}$$

where $DP(p)$ is represented by a 2-by-2 matrix. Thus, the linearization is a linear map from S to itself. If the two eigenvalues of $DP(p)$, denoted λ_s and λ_u, are such that $|\lambda_s| < 1 < |\lambda_u|$, then the fixed point is said to be *hyperbolic*. The eigenvectors associated with the eigenvalues of the linearization of a hyperbolic fixed point define linear subspaces, E^s and E^u, that are invariant under the flow of the linearization map, $DP(p)$. The stable/unstable manifold theorem for maps states that for the fully nonlinear map $P : S \to S$, in a neighborhood of p, there exist local invariant manifolds W^s_{loc} and W^u_{loc} that are tangent to the linear subspaces E^s and E^u at p, respectively; and are as smooth as the map P. Finally, iterating points on each of these local manifolds reveals the global stable and unstable manifolds:

$$W^s = \bigcup_{k=0}^{\infty} P^{-k}(W^s_{loc}(p)) \quad \text{and} \quad W^u = \bigcup_{k=0}^{\infty} P^{k}(W^u_{loc}(p))\,. \tag{2.14}$$

Successive consequents of a point s on the stable manifold will asymptote to p along W^s, while successive antecedents of a point u on the unstable manifold will asymptote to p along W^u.

It should be made clear that these asymptotic manifolds, associated with the fixed point p, cannot self-intersect since this would violate the smoothness condition of the mapping P. Nevertheless, the two asymptotic manifolds *may intersect each other*. In his memoir, Poincaré refers to these points of transverse intersection as *doubly asymptotic* points, referring to the manner in which they asymptote to the same fixed point in both forward and backward time. Later, in the third volume of *Method Nouvelles* [Poincaré 1899], he referred to these points as *homoclinic points*, and also

introduced the concept of *heteroclinic points* — points whose consequents asymptote toward a fixed point p_+, but whose antecedents asymptote toward a different fixed point p_-.

The remaining discussion in this chapter is essentially an attempt to mathematically describe the implications resulting from the fact that these asymptotic manifolds intersect. A first consequence that is trivial to derive, yet has dizzying implications, is the fact that a single intersection implies infinitely many intersections. Starting with a homoclinic point $s \in W^s \bigcap W^u$, we realize that by definition, $P(s)$ also lies on both the stable and unstable manifolds. Repeated applications of the map reveal an infinite number of intersections.

An important point is that since the map P is orientation preserving, the unstable manifold will have to double-back and intersect at an intermediate point q, before intersecting again at the point $P(s)$ as shown in Figure 2.1(b). Geometrically, we begin to envision the unstable manifold doubling back repeatedly across the stable manifold as the points of intersection asymptote toward the periodic point. In a similar way, when we consider antecedents, the stable manifold doubles back across the unstable manifold as they asymptote toward the fixed point in backward time.

The intersections and doubling back of the manifolds define closed regions in the section S, called *lobes*. As the iterated map takes successive consequents closer and closer to the fixed point, the distance between intersections that define the base of the lobe becomes arbitrarily small. Consideration of the fact that the map is area-preserving implies that the lobe must become longer and longer after each iteration while never intersecting neighboring lobes. Hence, the manifold that outlines the lobes oscillates wildly as it doubles back and forth across the other manifold. Lobes from each of the manifolds will inevitably intersect one another creating even more homoclinic points yielding a complicated picture that is referred to today as a *homoclinic tangle*. It is noteworthy that the map need not be area-preserving in order for the tangle to form – the linear rate of compression and expansion along the stable and unstable linear subspaces associated with the hyperbolic fixed point are sufficient

to produce the tangle.

In his memoir, Poincaré declined to draw the homoclinic tangle, but his oft-quoted description of the situation is provided here [Poincaré 1899]:

> If one seeks to visualize the pattern formed by these two curves and their infinite number of intersections, each corresponding to a doubly symptotic solution, these intersections form a kind of lattice-work, a weave, a chain-link network of infinitely fine mesh; each of the two curves can never cross itself, but it must fold back on itself in a very complicated way so as to recross all the chain-links an infinite number of times.
>
> One will be struck by the complexity of this figure, which I am not even attempting to draw. Nothing can give us a better idea of the intricacy of the three-body problem, and of all the problems of dynamics in general, when there is no uniform integral and the Bohlin series[1] diverge.

The homoclinic tangle is considered the trademark of *chaos*. Although the map is both differentiable and deterministic, the effect of its repeated action is to tear apart nearby trajectories in such a way that the trajectories can have arbitrarily different outcomes and may have arbitrarily complicated behavior. For instance, Poincaré showed in *Method Nouvelle* Volume I [Poincaré 1899] that given any particular solution, there exists a periodic solution of a sufficiently large period that is arbitrarily close to the particular solution for an arbitrary long period of time. The full implications of the homoclinic point will be discussed later in the context of the Smale horseshoe map which provides an elegant description of the chaotic dynamics near the homoclinic point.

Amongst the mathematical community, homoclinic points were not thoroughly investigated after Poincaré, and became largely forgotten. Smale described the situation in this way [Smale 1998]:

> Unfortunately, the scientific community soon lost track of the important ideas surrounding the homoclinic points of Poincaré. In the conferences in differential equations and dynamics that I attended in the late 50's, there was no awareness of this work. Even Levinson never showed in his book, papers, or correspondence with me that he

[1] Bohlin had published a series method just before the submission of his memoir.

> was aware of homoclinic points. It is astounding how important scientific ideas can get lost, even when they are exposed by leading mathematicians of the preceeding decades.

This being said, there were several mathematicians who were influenced by Poincaré's work, and kept his ideas alive.

Soon after the death of Poincaré, Birkhoff, a young American mathematician, proved Poincaré's "Last Geometric Theorem," and continued to develop the theory of dynamics from this geometric perspective. Morse, a student of Birkhoff, developed the theory of *symbolic dynamics* in which the motion of a trajectory is abstracted as a sequence of labels, a key to the topological treatment of chaotic trajectories.

Hadamard, a French mathematician, greatly admired Poincaré's work and studied geodesics on curved surfaces using many of the tools Poincaré had developed. He used Poincaré's Recurrence Theorem and the Poincaré section to analyze geodesics. He showed that in the neighborhood of every bounded geodesic, there were infinite unbounded geodesics. Thus, small changes in the initial condition could lead to geodesics of entirely different character. Hadamard observed this *sensitivity to initial conditions* (a hallmark of chaos encoded in the homoclinic tangle), and realized that it was nonsensical to discuss stability of the solar system, for example, since outcomes were not continuous with respect to initial conditions [Barrow-Green 1996].

2.2 Smale and the horseshoe map

The work of Poincaré and Birkhoff continued with Smale who provided an elegant topological description of the chaotic nature of the trajectories in the homoclinic tangle. By abstracting the dynamics of the tangle as a differentiable map, he showed conjugacy between the chaotic trajectories envisioned by Poincaré, and a shift automorphism on a sequence of binary symbols. In essence, he showed that the trajectories in a homoclinic tangle are as chaotic as a repeated coin flipping experiment.

At the time of his discovery of the horseshoe map and its relationship to homoclinic solutions, Smale was a postdoctoral scholar at IMPA in Brazil [Smale 1998]. In

the IMPA library, he browzed the collected works of Birkhoff[2] and started to work in the area of topological dynamics. After publishing a paper in which he claimed "chaos cannot exist", he received a letter from Levinson that caused him to rethink his conclusion. Levinson directed him to one of his papers that provided a counterexample to Smale's claims. Levinson's paper [Levinson 1949] provided an analysis of a simplified model for radar circuits that had been studied previously during the second world war by Cartwright and Littlewood. Cartwright and Littlewood investigated the anomalous behavior of radar circuits that had hampered military field operations. A study of the solutions of the differential equations governing the circuitry revealed "a rich variety of behaviour, some of it very bizarre" [Cartwright 1945]. Their analysis showed that the system possessed an infinite number of periodic motions of "a great variety of structures." They were in fact observing the complicated dynamics associated with a homoclinic tangle. In his study, Levinson provided a similar result although on a somewhat simpler system in an attempt to clarify their results.

Smale assimilated these results from Birkhoff, Levinson, Littlewood, and Cartwright, and developed the Smale horseshoe map to provide a complete description of these chaotic trajectories.

The horseshoe map is an abstraction of the flow near a homoclinic tangle. First, consider what happens to a rectangular patch on the surface of section S in the vicinity of a hyperbolic fixed point under the iterated application of the map. In Figure 2.2, a rectangular patch, consisting of three strips colored red, blue, and green, is mapped forward around the tangle. (Figure 2.2(a) contains three iterates of the map, after which, Figure 2.2(b) illustrates an additional three iterates of the map.) In the immediate vicinity of the fixed point, the linearized flow dominates, and we see that the patch is squeezed in one direction and lengthened in the other. Under repeated action of the map, the patch is eventually brought again into the region near the fixed point. Thus for some positive integer m, the map $Q := P^m$ is a map from the patch into itself. A single iteration of the map, Q, yields an interesting outcome.

[2]Smale's PhD advisor was Bott, a student of Duffin, in turn a student of Bourgin, who was a student of Birkhoff.

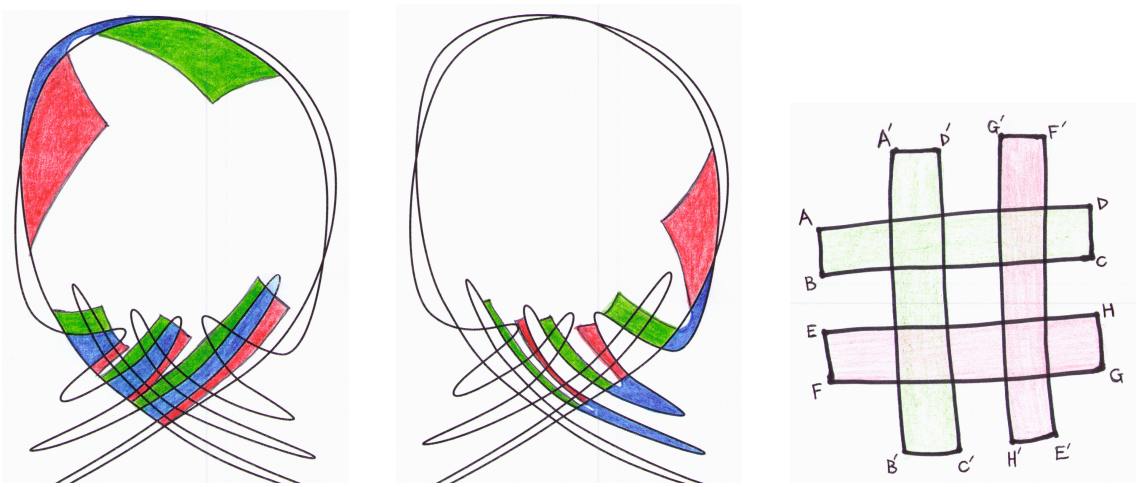

(a) (b) (c)

Figure 2.2: The action of the homoclinic tangle on a rectangular patch is illustrated here. The patch consists of three stripes colored red, blue, and green. Figure (a) shows the first three iterates of the map, and Figure (b) shows the last three. The red and green strips are returned to the patch, while the blue strip is removed. The initial and final orientation of the red and green strips is shown in (c), where A' is the consequent of A. Both strips return with a vertical orientation, and the red strip is turned upside down.

First we notice that the middle blue "third" of the patch has been removed entirely, while the red and green "thirds" are reorientated. The portion of the patch that remains inside the tangle will be mapped again under the action of the dynamics. The crux of this exercise is to carefully observe which points remain inside the tangle.

Carefully keeping track of the red and green strips during the mapping around the tangle, allows us to determine their orientation once they return to the patch. Figure 2.2(c) shows the initial horizontal orientation of the strips, overlaid with the final vertical orientation of the strips. Not only have the strips been squeezed and stretched – the red strip has been turned upside down!

The action of the homoclinic tangle just described is abstracted as the *horseshoe map* $Q : S \to \mathbb{R}^2$ acting on the square $[0,1] \times [0,1] \subset \mathbb{R}^2$ and is shown graphically in Figure 2.3. Again, we consider three horizontal strips of the square: the first labelled A, the third C, while the middle strip B does not return to the square under the action of the map.

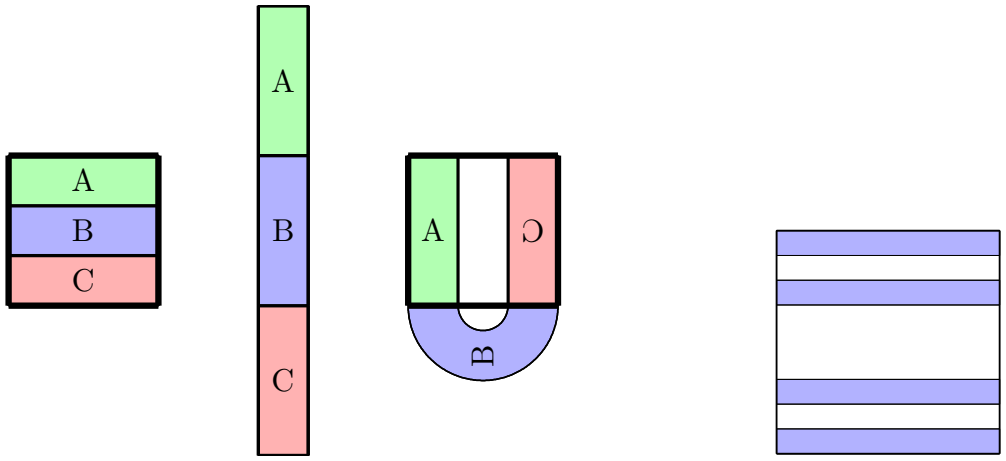

Figure 2.3: (a) Forward iteration of the Smale horseshoe map. (b) The set that remains in the square after two iterations of the *forward* map is colored blue.

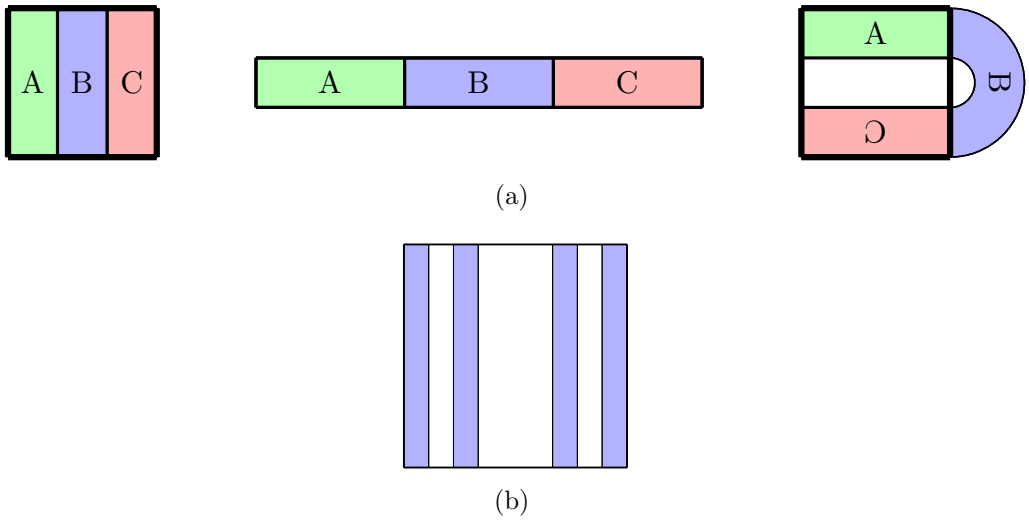

Figure 2.4: (a) Backward iteration of the Smale Horseshoe map. (b) The set that remains in the square after two iterations of the *backward* map is colored blue.

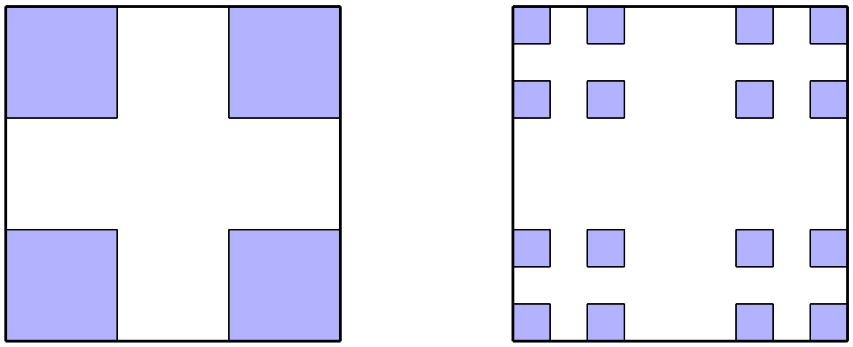

(a) The set that remains invariant under one iteration of both forward and backward maps.

(b) The invariant set after two iterations of both the forward and backward maps.

Figure 2.5: In the limit as the number of iterations of both the forward and backward maps approaches infinity, the invariant set approaches the Cantor set.

We may also consider the backward iteration of the map (Figure 2.4). In this case, a vertical "third" of the patch is removed upon each iteration. In the limit as the number of iterations both forward and backward becomes infinite (Figure 2.5), the invariant set of points that remain, denoted $\Lambda := \bigcap_{k=-\infty}^{\infty} Q^k(S)$, is a *Cantor set*. The set Λ contains uncountably infinite points, but has measure zero.

We assign to each point in Λ, a symbolic representation of its entire bi-infinite trajectory. We begin with the map $\varphi : \Lambda \to \{0, 1\}$ that assigns to a point, $q \in \Lambda$, a symbol, either 0 or 1, according to the rule:

$$\varphi(q) = 0 \quad \text{if} \quad q \in A\,, \qquad \text{and} \qquad \varphi(q) = 1 \quad \text{if} \quad q \in C\,. \tag{2.15}$$

Next, using this symbol assignment map φ, we define the map $\phi : \Lambda \to \Sigma$ that maps a point $q \in \Lambda$ to the space of all possible bi-infinite sequences of the symbols 0 and 1 according to:

$$\phi(q) = \left[\varphi(P^k(q))\right]_{k=-\infty}^{\infty}\,. \tag{2.16}$$

By this construction, we now have a representation for every trajectory under P as a bi-infinite ordered sequence of symbols that describes precisely how the trajectory

$$\begin{array}{ccc} \Lambda & \xrightarrow{P} & \Lambda \\ \downarrow{\scriptstyle \phi} & & \downarrow{\scriptstyle \phi} \\ \Sigma & \xrightarrow{\sigma} & \Sigma \end{array} \tag{2.18}$$

Figure 2.6: The dynamics of P on the invariant set Λ is conjugate to a shift map on the space of bi-infinite sequences, Σ.

meanders back and forth between A and C. The action of the map results in a simple shift on the sequence of symbols. That is,

$$\phi(P(q)) = \sigma(\phi(q))\,, \tag{2.17}$$

where $\sigma : \Sigma \to \Sigma$ simply shifts the list of symbols one space to the left. Furthermore, the fact that both the images and pre-images of A lie in both A and C (and *vice versa*), implies that to every bi-infinite sequence of symbols, we may assign a trajectory in Λ. Thus, $\phi : \Lambda \to \Sigma$ is a homeomorphism (continuous, invertible mapping) between the set of trajectories in Λ, and the set of bi-infinite sequences, Σ. By providing this construction, Smale showed that the two sets, Λ and Σ, are *topologically conjugate*. The commutation diagram that illustrates the conjugacy between the map $P : \Lambda \to \Lambda$ and $\sigma : \Sigma \to \Sigma$ through $\phi : \Lambda \to \Sigma$ is shown in Figure 2.6.

The upshot of this construction is that the morass of complicated trajectories in the homoclinic tangle envisioned by Poincaré is completely and elegantly described by a consideration of the shift map on the space of bi-infinite sequences of two symbols. Specifically, Smale was then able to use this conjugacy to describe the possible orbits in Λ, and by considering all possible sequences of symbols, conclude that Λ has

1. a countable infinity of periodic orbits with arbitrarily high period,

2. an uncountable infinity of periodic orbits, and

3. a dense orbit.

The dense orbit is obtained by considering the concatenation of all possible finite

sequences. Moreover, given any finite trajectory, it is easy to see how repeating the sequence produces a periodic orbit that is arbitrarily close.

The (Poincaré)-Smale-Birkhoff Homoclinic Theorem is stated precisely as follows:

Theorem: (Smale-Birkhoff Homoclinic Theorem)
Suppose q is a transversal homoclinic point of $P \in Diff(S)$. Then there is a Cantor set $\Lambda \in S$, and $N \in \mathbb{Z}^+$ such that $P^N(\Lambda) = \Lambda$, and $P^N(\cdot)$ restricted to Λ is topologically a shift automorphism.

The value of N is chosen large enough, precisely to ensure that the square patch in S is returned by the map P to S after its journey around the homoclinic tangle.

In sum, the conjugacy of the horseshoe map with a shift automorphism provides a succint framework in which to understand homoclinic dynamics. For instance, we see the existence of sensitivity to initial conditions: there exist two sequences with identical histories, but with very different futures.

The lobes defined by the intersections of the stable and unstable manifolds, and their evolution under the action of the Poincaré map, reveal the transport mechanism of *lobe dynamics*, that is responsible for entraining and detraining lobes both into and out of the homoclinic tangle, as illustrated in Figure 2.7. This transport mechanism will feature prominently in the time-dependent flows we shall consider in later chapters.

Finally, in terms of our present study it is important to note that the framework provided here by Poincaré and Smale is for a system that exhibits time periodic forcing. In fact, it is precisely this fact that allows for abstraction of the dynamics as the repeated application of a differentiable map. Some work has been done for analogs of this theory in quasi-periodic flows [Beigie 1991]; however, no concrete theory is currently available for aperiodic turbulent flows.

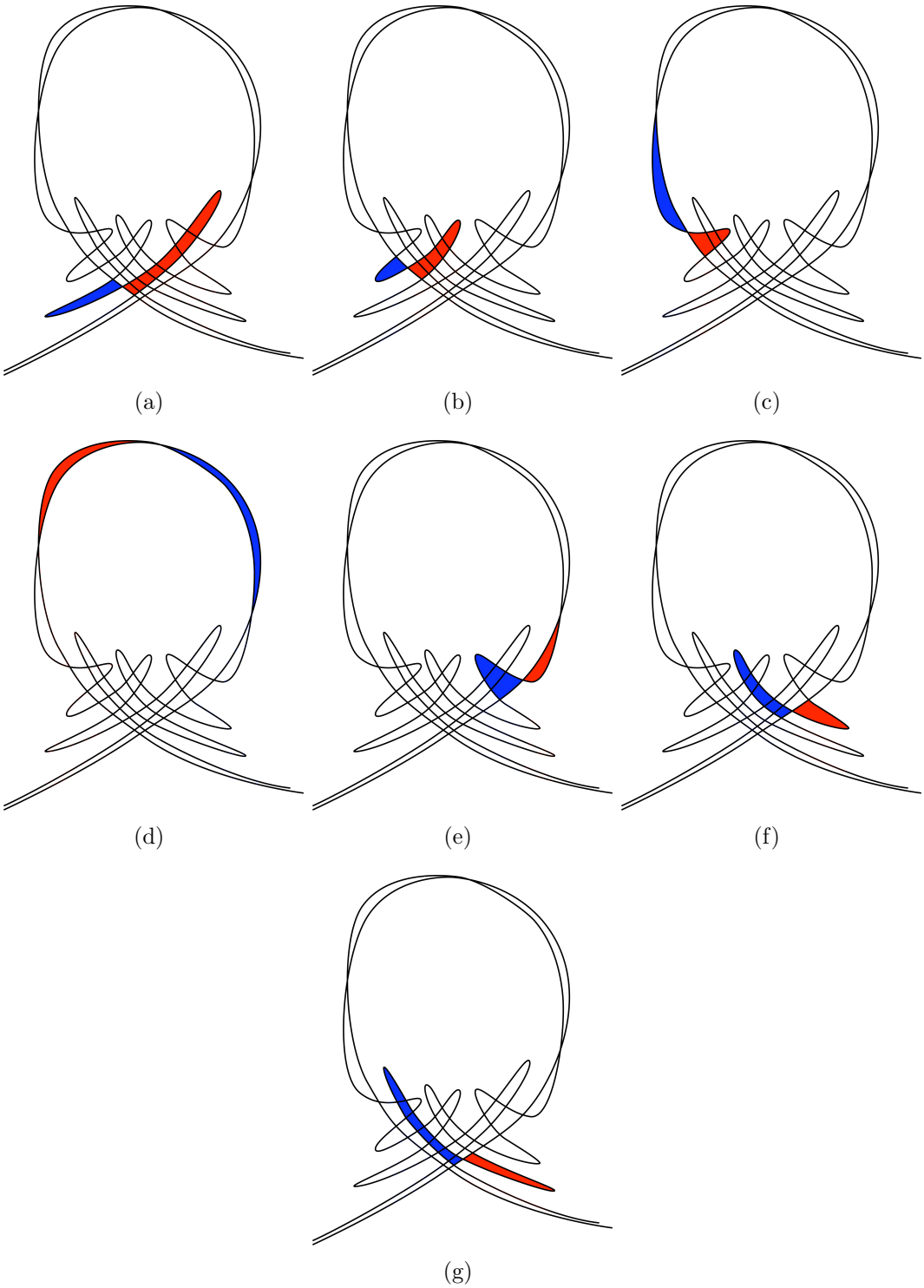

Figure 2.7: Transport via lobe dynamics in a homoclinic tangle. Under the action of the Poincaré map, the blue lobe is entrained into the vortex, while the red lobe is detrained.

Chapter 3

FTLE, LCS, and Five Examples

Here we review the method of extracting Lagrangian Coherent Structures (LCS) using the method of Finite Time Liapunov Exponents (FTLE). The method was first developed by Haller [Haller 2000], and further references that provide more detail include [Shadden 2005] and [Lekien 2007]. The underpinning premise in the FTLE method is that coherent structures in a turbulent flow are best characterized and identified by the surfaces of greatest separation. This Lagrangian approach, which uses particle trajectories that necessarily encode the time-dependence in the velocity field, is more effective in identifying persistent coherent structures than methods that utilize only Eulerian criteria. The method has the advantages that it is directly applicable to aperiodic flows, and to flows that are defined by discrete data sets over a finite time interval.

After reviewing the basic definitions, we will briefly examine five examples that illustrate various features of the method for a variety of flows.

3.1 FTLE and LCS

The discussion here will be with regard to two-dimensional flows in the plane, although this can be generalized to flows in n-dimensions, and to flows on manifolds [Lekien 2007]. We take the approach that the Eulerian velocity field describing the flow is given at the outset, either as an explicit analytical model, or as the result of integrating primitive equations for the flow (Navier-Stokes, for example), or from

interpolations of direct observations and measurements of the flow. The flow may correspond to an actual fluid flow, or the flow in the phase space of a dynamical system.

Since the FTLE method is a Lagrangian approach, we will need to compute the flow map that maps particles forward along their trajectories. Differentiation of the flow map will provide a measure of separation under the action of the flow. Finally, we define the LCS to be the surfaces in the flow on which separation is locally maximal.

Let the open set $D \subset \mathbb{R}^2$ be the domain of interest in the flow, and let $\mathbf{v}(\mathbf{x}, t)$ be a smooth time-dependent vector field on D that we refer to as the *velocity field*. At each time t, the velocity field assigns to each point $\mathbf{x} \in D$, a tangent vector from $T_{\mathbf{x}}D$. A *trajectory*, $\mathbf{q}(t; \mathbf{x}_0, t_0)$, is the unique curve in D parametrized by time that passes through the initial condition $\mathbf{x}_0 \in D$ at time t_0, and whose tangent vectors satisfy the vector field $\mathbf{v}$:

$$\frac{d\mathbf{q}(t; \mathbf{x}_0, t_0)}{dt} = \mathbf{v}(\mathbf{q}(t; \mathbf{x}_0, t_0), t)$$

for all times t. In the applications, the trajectory is obtained by numerically integrating the velocity field, using a Runge-Kutta scheme, for example.

Let $\phi_{t_0}^{t_0+t} : D \to D$ be the *flow map* associated with the vector field, so that

$$\phi_{t_0}^{t_0+t}(\mathbf{x}_0) := \mathbf{q}(t_0 + t; \mathbf{x}_0, t_0)\,.$$

For a smooth velocity field, $\phi_{t_0}^{t_0+t} : D \to D$ is a smooth map that depends on both the time, t_0, and the time of integration, t. Clearly, $\phi_{t_0}^{t_0} : D \to D$ is the identity map on D.

The flow map encodes the Lagrangian paths of particles, and provides access to the amount of local stretching in the flow. To this end, we use the linearization of the flow map,

$$\mathbf{x} \to D\phi_t^{t+T}(\mathbf{x})\,, \tag{3.1}$$

represented by a 2×2 matrix, to define the Cauchy-Green deformation tensor:

$$\Delta := \left[D\phi_t^{t+T}(\mathbf{x})\right]' D\phi_t^{t+T}(\mathbf{x}) \,, \tag{3.2}$$

where A' indicates the transpose of the matrix A. The adorning symbols on Δ have been dropped to avoid notational clutter, but it is understood that Δ assigns to each point in the domain D a time-dependent 2×2 matrix. Furthermore, Δ is everywhere positive definite and hence has positive eigenvalues. The deformation tensor contains information about the amount of (linearized) stretching in the flow. If the largest eigenvalue of Δ is greater than unity, then the eigenvector associated with this eigenvalue provides the direction in which the largest separation will occur. Thus, the eigenvalues of Δ provide a measure of the rate of separation. Accordingly, the Finite Time Liapunov Exponent, $\sigma_T(\mathbf{x}, t)$, is a time-dependent scalar field defined using the maximum eigenvalue of Δ:

$$\sigma_T(\mathbf{x}, t) := \frac{1}{2|T|} \ln \lambda_{\max}(\Delta) \,. \tag{3.3}$$

When convenient, we sometimes drop the notation indicating the dependencies, and write just σ. The FTLE defined in this way is a measure of the separation of trajectories induced by the flow over the interval of time $(t, t+T)$ with values of the FTLE greater than zero representing separation.

Following [Shadden 2005], we define the LCS to be locally maximizing surfaces, or "ridges", in the scalar field σ_T. In practice, the intuitive definition of "ridge" suffices to identify the LCS; however, in order to provide a precise mathematical definition, we must first introduce the notion of curvature of the surface σ, by defining the 2×2 Hessian matrix Σ:

$$\Sigma := D^2 \sigma_T(\mathbf{x}, t) \,. \tag{3.4}$$

By equality of mixed partial derivatives, Σ is a real symmetric matrix, and consequently has real eigenvalues and orthogonal eigenvectors. We label the smallest eigenvalue of Σ, $\lambda_{\mathbf{n}}$, and the associated eigenvector, $\mathbf{n}$. Then, we define the LCS to

be the set of all points in the domain for which the following two conditions hold:

C1. $\lambda_{\mathbf{n}} < 0\,,$

C2. $\nabla\sigma \cdot \mathbf{n} = 0\,.$

Taken together, these conditions define a curve in D that moves in time. As we shall see in the forthcoming examples, the LCS defined in this way for a wide range of flows are remarkably sharp, indicating that separation is generally not a diffuse property and is concentrated along LCS curves.

The definition of FTLE admits both positive and negative flow times T. For positive values of T, the FTLE measures separation forward in time and yields LCS that act as *repelling* surfaces; while for negative values of T, the FTLE measures separation backward in time, and hence yields LCS that act as *attracting* surfaces in forward time.

The LCS as defined above are co-dimension one surfaces of greatest separation. From a broader perspective, it is understood that these LCS curves are then used to identify the relevant coherent structures in a flow. For instance, the LCS may define the boundaries of an ocean eddy, whereas from the user's point of view, the eddy itself is the coherent structure of interest.

From a practical standpoint, the FTLE is computed numerically by placing a Cartesian grid of particles covering the flow region D. The flow map is then approximated by integrating all the particle trajectories forward in time. Differentiation of the flow map is performed via finite differencing to yield the FTLE at each point in D. The procedure is then repeated at subsequent time intervals in order to discover the time evolution of σ.

Increasing the integration time T tends to sharpen the ridges and extend their length in space. Typically, choosing a value for T is motivated by the relevant time-scales in the flow; T must be chosen long enough so that the important dynamics in the flow have sufficient time to induce separation. Choosing a value of T too large leads to too many LCS to be sensible. The choice of the integration time T is thus also tied to the relevant length scales that are most active in the flow. In practice, if the

given velocity field covers the temporal and spatial scales of interest, then choosing a suitable value of T is seldom an issue.

To complete this overview of LCS, we now provide five examples of FTLE fields and their corresponding LCS for a wide range of flow regimes.

3.2 The simple pendulum

To begin, we investigate the FTLE for the flow in the phase space of the simple pendulum. This is an elementary example (the flow is not even time-dependent!), but will be illustrative of the main features of LCS, and will also raise important non-trivial issues that will be addressed in later chapters.

The state of the simple pendulum is described by the angle of the pendulum with the vertical, θ, and its angular velocity, ω. The evolution of the flow through (θ, ω)-phase space is given by:

$$\begin{aligned} \dot{\theta}(t) &= \omega(t) \\ \dot{\omega(t)} &= -\sin\theta(t)\,, \end{aligned}$$

and the velocity field is shown in Figure 3.1(a).

The corresponding repelling FTLE field for an integration time of 11 time units is shown in Figure 3.1(b). The LCS are easily discernible ridges in the FTLE, and separate regions in which the pendulum motion is a back-and-forth oscillation, from regions of running windmill behavior. Computing the FTLE for integration backward in time yields the attracting FTLE field in Figure 3.1(c). Taken together, the repelling LCS and the attracting LCS enclose the region of oscillating motion. Thus, the LCS act as *separatrices* in that they separate regions of the flow with qualitatively different behavior. Also, we observe that increasing the integration time "grows" the manifold, since more trajectories that begin closer to the unstable vertical equilibrium point will have the opportunity to separate.

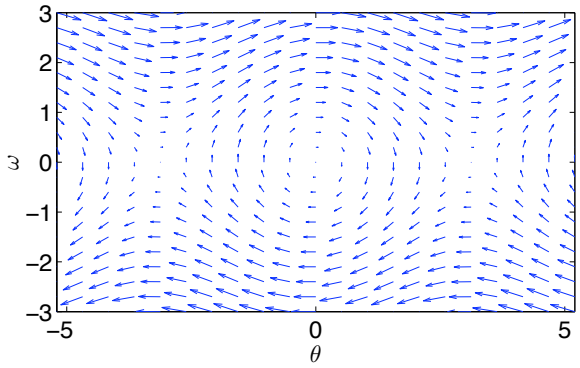

(a) Velocity field for the simple pendulum.

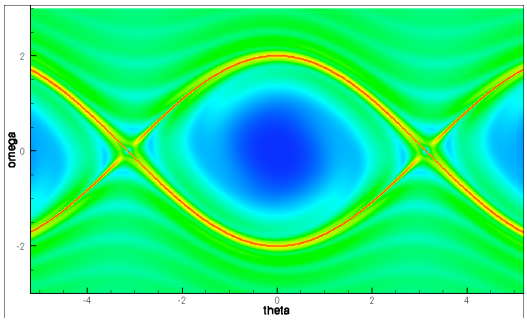

(b) Repelling FTLE for the simple pendulum flow. The LCS are sharp ridges that separate regions of oscillatory motion from regions of "running" motion.

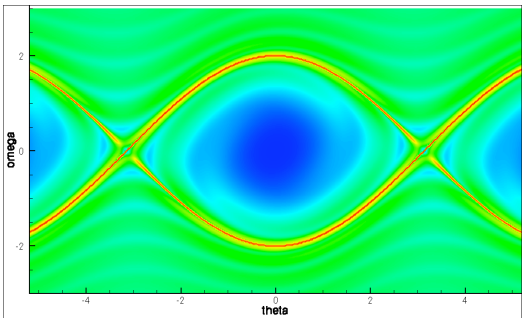

(c) When combined with the LCS in the attracting FTLE field shown here, the LCS fully enclose the region of oscillatory motion.

Figure 3.1: FTLE and LCS in the flow of the simple pendulum.

3.3 Monterey Bay

In this example, we analyze the flow defined by output from a nested ocean model for two-dimensional surface flow in a coastal region near Monterey Bay, California provided by Chao (see [Li 2008] for details of the model). In the figures below, the FTLE scalar fields in both forward and backward time directions have been computed, and then plotted as an overlaid filled contour plot using windowing of the fields to reveal only the regions of strongest repulsion and attraction. Colored drifters are also placed in the flow to indicate their motion relative to LCS.

The sequence of images reveals properties of the LCS that recur for a wide-range of flows. These are:

- The LCS delineate regions that have different dynamical fates – brown drifters re-circulate near the coast, while green drifters are flushed out to sea.
- Intersections of the attracting and repelling LCS define strongly hyperbolic points in the flow.
- The LCS are almost inariant, in that very little fluid crosses the LCS.
- The LCS act as barriers to transport, and reveal pathways by which transport occurs.

The LCS computed for coastal regions can be used to guide the placement of drifters for measuring ocean data so that the drifters recirculate within the region of interest and achieve better coverage. An experiment to implement this approach is being conducted in July and August, 2009, in Prince William Sound, Alaska, where the modeling of the transport of oil spills due to ocean currents in the sound is of particular interest. The LCS can also be used to recognize persistent structures in coastal waters such as eddies separating off coastal protrusions. In a separate study, [Lekien 2005] has investigated the use of LCS to mitigate the effect of pollution discharges by ensuring that effluent is released at times when there are no transport barriers to prevent pollutants from being quickly flushed out to sea.

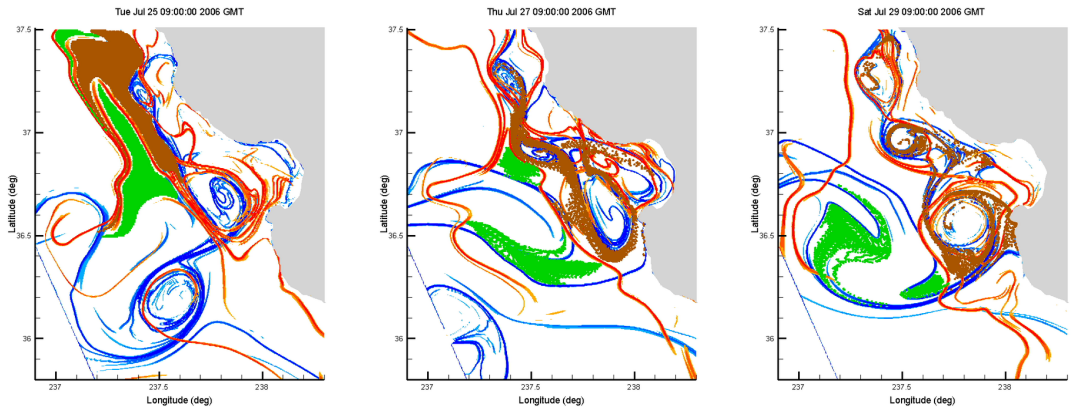

Figure 3.2: LCS near Monterey Bay are depicted here at 48 hour intervals. The attracting LCS (blue curves) and the repelling LCS (red curves) define the boundaries of vortices as well as lobes colored green and brown. Since no fluid crosses the LCS, transport and mixing occurs via the motion of the lobes. The green lobes are flushed out to sea while the brown lobes recirculate near the coast.

3.4 The atmosphere of Titan

Images recently returned from the Cassini and Huygens missions to Saturn's moon, Titan, have spurred great interest in further exploring the meteorology of Titan's dense atmosphere, hydrological cycle, and hydrocarbon lakes. Designs for Montgolfiere balloons are currently under consideration as the observing platform of choice for exploring the Titan environment. With limited onboard propulsion, the venturing capabilities of a balloon will depend largely on the transport structures present in the Titan atmosphere. Consequently, design engineers will need to consider whether, for example, there are barriers to transport into and out of the polar regions, or if there are regions of potential entrapment, or if wind reversals as a function of altitude will allow for navigation with the aid of a small amount of vertical control authority.

We have computed three-dimensional LCS using the velocity fields in a Titan wind model provided by the authors of [Richardson 2007]. Figure 3.3(a) shows a sample constant-height section through the FTLE field. We observe turbulent structures in the mixing region between the retrograde equatorial flow, and the zonal flow in the upper latitudes. Furthermore, a strong repelling LCS encircles the northern polar region, indicating that travel to the pole during this time period will be impossible

using ambient winds alone. Blue and red drifters placed on either side of this separatrix enter different dynamical regimes: the blue drifters continue to rapidly circle the pole, while the red drifters enter a quiescent pocket closer to the equator. In a similar manner to the pendulum example, the LCS delineates a separation between regions with different dynamical outcomes.

3.5 Overflows in the North Atlantic

The thermohaline circulation is oceanic flow driven by buoyancy effects due to differences in temperature and salinity, and leads to global circulation of the oceans. The circulation transports and distributes large amounts of energy, and hence has paramount influence on the global climate. Indeed, conjectures have been made that global warming could cause the thermohaline circulation to cease, drastically affecting global climates - most especially the climate of Northern Europe [Vellinga 2002]. Thus, accurate global climate forecasting requires a through understanding of the transport mechanisms at play in the thermohaline circulation.

An important element of thermohaline transport is mixing that occurs in oceanic *overflows*, a process in which cold dense saline water descends below warmer less dense fresh water causing instability and mixing at the interface. Current global climate models have grid scales too large to resolve these mixing processes, and must resort to a parametrized model to capture their effects.

Odier has conducted laboratory experiments described in [Odier 2007] to replicate oceanic overflows and characterize the resulting turbulent mixing processes so that these effects may be included in global models. (For practical purposes, the experimental setup actually investigates the ascension of less dense fluid against an inclined plate, rather than the sinking of a cold dense fluid.) The fluid is initially passed over a propeller to induce turbulent flow and the flow field is imaged using particle image velocimetry.

In order to characterize mixing, the interface between the two fluids must first be determined, and then the amount of flux across this boundary must be measured.

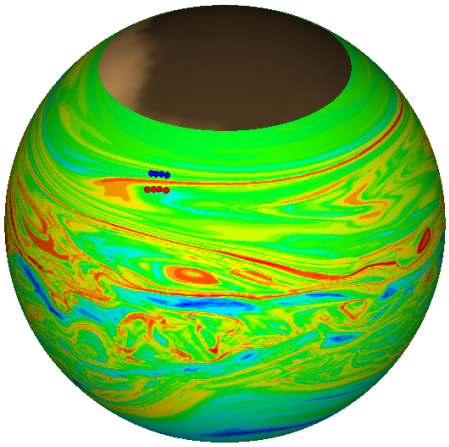

(a) The FTLE for the atmosphere of Titan. A repelling LCS acts as a barrier to transport to the North Pole.

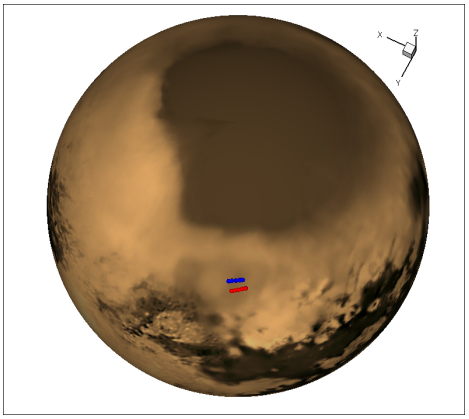

(b) Four particles are placed on either side of the repelling LCS.

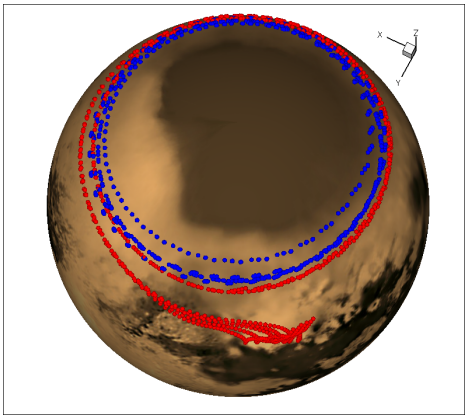

(c) The blue and red drifters separate. The blue drifters continue to circle the pole, while the red drifters enter a different flow regime closer to the equator.

Figure 3.3: LCS in the atmosphere of Titan.

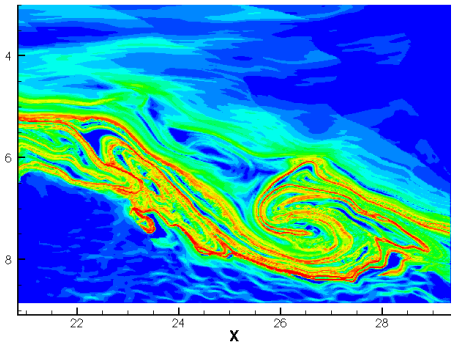

(a) Repelling FTLE. The LCS indicates the interface between the layers. Furthermore, the LCS indicates the lobe that will be *detrained* from the overflow above to the quiescent flow beneath.

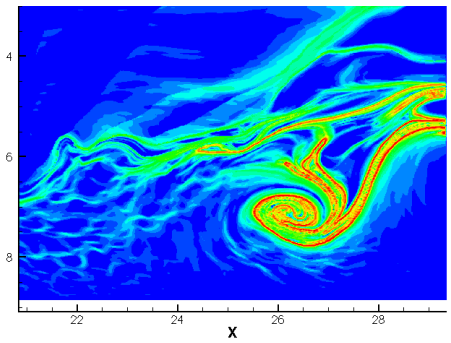

(b) Attracting FTLE. The LCS indicates a lobe that will be *entrained* into the overflow above.

Figure 3.4: LCS in experimental realizations of ocean overflows.

Not surprisingly, the identification of this boundary for the turbulent flow is not easily performed by viewing plots of traditional Eulerian fields. Velocity and vorticity plots are unhelpful and misleading.

We have computed LCS for flow data obtained during the overflow experiment with promising results. The repelling LCS shown in Figure 3.4(a) captures the turbulent mixing layer and shows the boundary between the less dense overflow moving to the right above the quiescent more dense fluid below. In Figure 3.4(a), we see that the LCS reveals not only the interface, but also the mechanisms by which mixing occurs: the LCS outlines a narrow tendril-shaped lobe that will be detrained into the quiescent flow beneath, while fluid exterior to the lobe will exit the flow at top right. Similarly, the attracting LCS plotted in Figure 3.4(b) demarcates a lobe in the quiescent flow that will be entrained into the overflow above. In this way, LCS can be used to quantify detrainment and entrainment. In fact, to the extent that the flow is planar, the areas of the lobes correlate with the amount of mixing occuring across the interface.

3.6 The elliptic three-body problem

Koon has shown that careful consideration and utilization of invariant manifolds in the circular restricted three-body problem can reveal energy efficient pathways for transport in the solar system [Koon 2000]. Specifically, the stable and unstable manifolds of the periodic orbits, associated with Lagrange points in the restricted three-body problem, form tubes through which trajectories traveling from one region of phase space to another must pass. Desired itineraries are obtained by finding intersections between tubes traveling to and from the relevant regions.

Computing these invariant manifolds typically requires intensive computation of high order normal forms (above 20^{th} order for example), inserting initial conditions infinitesimally displaced in the stable and unstable directions, and then integrating forward and backward in time in accordance with the classical dynamical systems definition of stable and unstable manifolds. Adopting a different approach, we utilize the property that the invariant manifolds are also separatrices in the flow. Hence, we can compute the LCS to directly discover the tubes through which trajectories must pass. The versatility of the LCS method allows for computations of these manifolds even in the case of the elliptic restricted three-body problem in which the eccentricity of the primary orbits yields non-autonomous equations of motion [Gawlik 2009]. Moreover, the LCS method allows for the computation of these manifolds for the solar system using the aperiodic flow induced by the entire ephemeris.

Since the Jacobi integral is absent in the elliptic problem, we cannot project onto an energy surface and must integrate trajectories in the full four-dimensional phase space. To compute the LCS, we initialize trajectories on a three-dimensional Poincaré section ($y = 0$), integrate them forward in the four-dimensional space, and compute the FTLE. Figure 3.5(a) shows a still image of the time-dependent FTLE on this three-dimensional section, while Figure 3.5(b) is yet another section through this three-dimensional space onto the $(x, \dot{x})$-plane. The resulting LCS demarcate pockets of initial conditions that undergo different dynamical behavior – for instance, those outside the pocket remain in an orbit interior to Jupiter, while those inside the pocket

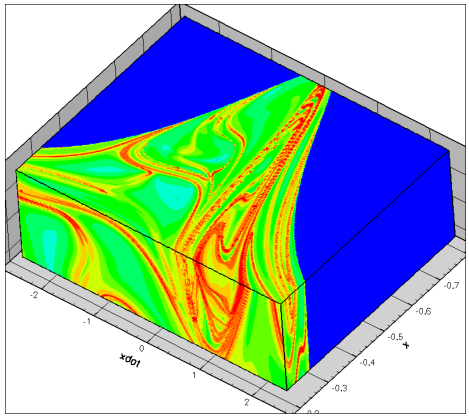

(a) A 3D section of the 4D FTLE for the elliptic three-body problem.

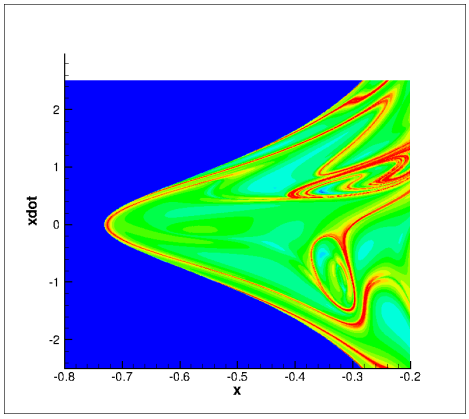

(b) A 2D section of the 4D FTLE for the elliptic three-body problem. Notice that the LCS cut out regions, or "tubes," in phase space.

Figure 3.5: LCS for the elliptic three-body problem.

escape Jupiter's orbit to an exterior orbit.

Chapter 4

LCS and the Perturbed Pendulum

We are now at a point where we can introduce the use of the FTLE-LCS method for identifying homoclinic tangles in time-dependent flows. Our main goal will be to identify these tangle structures in atmospheric and oceanic flows, but as a first example, it is instructive to apply the method to the case of the simple pendulum.

Consider the flow generated by the coupled differential equations

$$\begin{aligned} \dot{\theta}(t) &= \omega(t)\,, \\ \dot{\omega}(t) &= -\sin t - 0.65\omega(t)\sin \pi t\,. \end{aligned} \tag{4.1}$$

This flow is identical to the simple pendulum investigated in Section 3.2, but now an extra periodic forcing term has been added. We shall see that chaotic trajectories emerge from the existence of homoclinic points and a homoclinic tangle. However, our approach to obtain this understanding will be from a different perspective than that of Poincaré.

To appreciate the effect of the periodic forcing, it is instructive to first view an animation of the velocity field and then ask the questions: "Where do trajectories go now?", "How are portions of phase space transported?", "What happens to the separatrix between windmill and oscillating motions?". In short, the time-dependent velocity field provides very little intuition in answering these questions. Furthermore, plots of instantaneous streamlines in a snapshot of the velocity field are misleading in determining the important Lagrangian structures and transport mechanisms (Figure

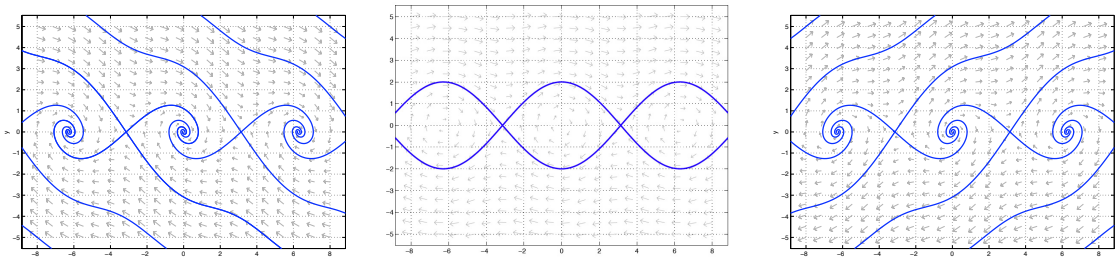

(a) (b) (c)

Figure 4.1: Snapshots of streamlines plotted in the time-dependent velocity field of the perturbed pendulum do not reveal the underlying transport mechanisms.

4.1).

Since the perturbation is periodic, we can follow the insight of Poincaré by considering t as a periodic variable with period 2π, and introducing a Poincaré section at $t = 0$. As described in Chapter 2, this reduces the flow to a discrete map on the two-dimensional section. Plotting iterates of this map produces the static plot in Figure 4.2 in which we recognize *resonance islands* that persist under the perturbation, and the *chaotic sea* corresponding to chaotic trajectories.

When we compute the LCS for this perturbed pendulum, we use a different approach that elucidates the time-dependent transport mechanism in the flow. Multiple intersections of the repelling and attracting LCS reveal a *homoclinic tangle*, and the time-dependence of the LCS reveals the continuous motion of the lobes defined by these intersections. Figures 4.3(a) through 4.3(d) show how lobes defined by the intersection of the repelling and attracting LCS delineate precisely the areas of phase space transported from one region to another via the mechanism of *lobe dynamics*: the green lobes are entrained into the region of oscillatory motion while yellow lobes are detrained. The action of lobe dynamics has previously been observed in laboratory flows [Shadden 2007] and in bio-propulsion flows [Franco 2007].

If we replace the periodic sinusoidal forcing in Equation (4.1) with a chaotic aperiodic forcing, the Poincaré section analysis can no longer be applied – there is no sensible definition for the Poincaré section. However, we can still proceed to compute the time-dependent LCS to understand the effect of the aperiodic perturbation

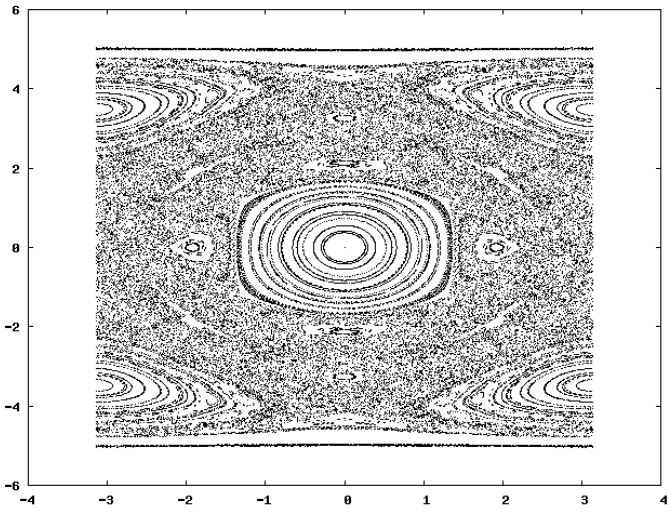

Figure 4.2: The Poincaré section for the periodically-forced pendulum reveals resonance islands and the chaotic sea.

on transport. Figure 4.4 shows the lobe structures present when the pendulum is perturbed with forcing obtained by coupling the pendulum to chaotic trajectories in the Lorenz equations. The lobes are now irregularly spaced in accordance with the irregularity of the time-dependence in the forcing, but they nevertheless persist as the important structures that indicate the passages to transport.

In this way, the FTLE-LCS method provides a technique for revealing homoclinic trajectories in aperiodic flows. The identification of lobes, and their subsequent entrainment and detrainment, will be a repeated theme in the study of geophysical flows in the remaining chapters.

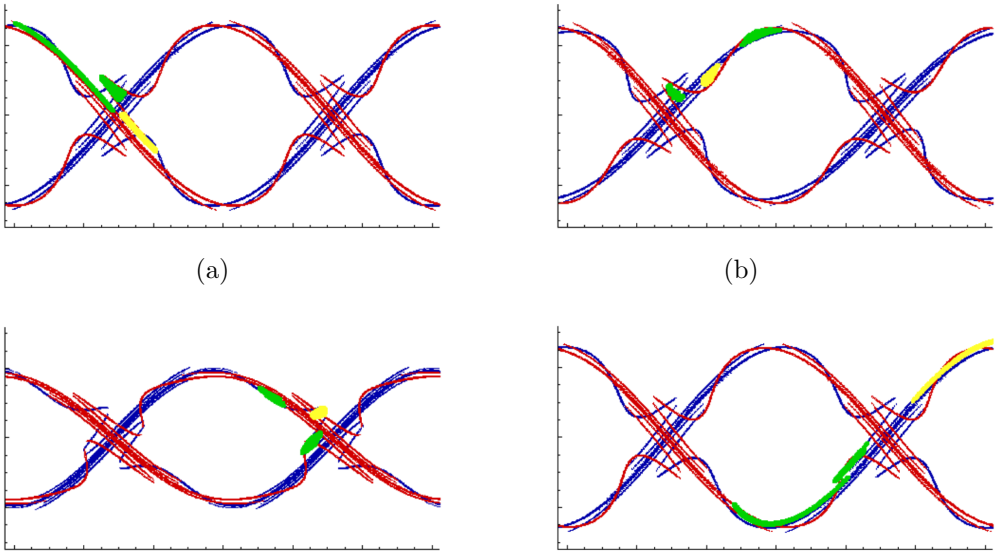

Figure 4.3: LCS analysis of the perturbed pendulum reveals that transport occurs through the action of *lobe dynamics*. Panes (c) through (f) illustrate the entrainment and detrainment of lobes: green lobes are entrained, yellow lobes are detrained.

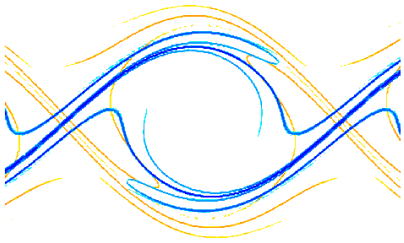

Figure 4.4: The LCS method can be applied to a chaotically forced aperiodic flow, and reveals the aperiodic lobe structures that govern transport. Here, the pendulum is chaotically forced by coupling to the Lorenz attractor.

Chapter 5

LCS in a Model for Mediterranean Eddies

We now use the FTLE-LCS method, and in particular the utility of the method for identifying homoclinic tangles, to study kinematic models for geophysical flows. We begin with the elliptic Kida vortex, an exact solution to Euler's equations for incompressible flow, that provides a model for flow in a storm on Neptune. Next, we study a generalization of the Kida vortex to a three-dimensional quasi-geostrophic flow that provides an ellipsoidal model that faithfully captures motion of Mediterranean eddies. In both cases, computation of the LCS reveals a tangle structure and its consequent chaotic dynamics in the flow surrounding the vortex.

5.1 The Kida vortex

The Kirchoff ellipse is a particular solution to Euler's equations for an incompressible fluid in two-dimensions [Kirchhoff 1876]. Kirchhoff's solution is obtained by placing an elliptical patch of uniform vorticity in an otherwise quiescent fluid. The ellipse rotates about its center at a rate proportional to the strength of the vorticity.

In an otherwise quiescent flow, let the ellipse

$$\frac{x^2}{a^2} + \frac{y^2}{b^2} = 1 \tag{5.1}$$

define a region of constant vorticity, ω, with a and b denoting the lengths of the

principal axes of the ellipse. As shown in [Lamb 1945], the stream function for flow exterior to the ellipse in elliptical coordinates (ξ, η) is

$$\psi_{\text{ext}} = \frac{1}{4} ab\omega e^{-2\xi} \cos 2\eta + \frac{1}{2} \omega ab\xi \,, \tag{5.2}$$

while interior to the ellipse, the stream function is

$$\psi_{\text{int}} = \frac{\omega}{2(a+b)} \left(bx^2 + ay^2 \right) \,. \tag{5.3}$$

The ellipse rotates with constant frequency

$$n = \frac{ab}{(a+b)^2} \omega \tag{5.4}$$

in such a way that a no slip boundary condition is satisfied between the exterior and interior regions.

Morton investigated the character of individual Lagrangian trajectories in this flow for different aspect ratios of the ellipse [Morton 1913]. He uncovered complex Lagrangian trajectories - a notable feat since all the particle integrations were done by hand.

Much later, Kida introduced a more general solution for the case of linear background flow [Kida 1981]. In this case, an elliptical patch of vorticity remains an ellipse, but the aspect ratios of the ellipse evolve over time in such a way that the area of the ellipse is conserved. Moreover, the rotational rate of the ellipse is not constant, and for certain initial conditions the ellipse undergoes nutation.

Given an elliptical patch of constant vorticity, ω, placed in a linear background flow with velocity components described by

$$u = ex - \gamma y \tag{5.5}$$

$$v = -ey + \gamma x \,, \tag{5.6}$$

Kida provided the evolution equations for the *orientation* of the ellipse, described by

the angle, $\theta(t)$, arbitrarily chosen between the major axis and the horizontal; and the *aspect ratio* of the ellipse, denoted $r(t)$, and defined as

$$r(t) := \frac{a(t)}{b(t)}\,. \tag{5.7}$$

Written as a coupled system of ordinary differential equations, the evolution of $r(t)$ and $\theta(t)$ is

$$\dot{r} = 2er\cos 2\theta \tag{5.8}$$

$$\dot{\theta} = -e\frac{r^2+1}{r^2-1}\sin 2\theta + \frac{\omega r}{(r+1)^2} + \gamma. \tag{5.9}$$

The elliptical patch of fluid now has constant vorticity

$$\omega' = \omega + 2\gamma\,, \tag{5.10}$$

and the stream function for determining the velocity of the fluid at any instant is determined using the stream functions as before for the Kirchhoff ellipse. Therefore, during simulation, we first integrate for the motion of the ellipse, and then integrate particle trajectories in the resulting velocity field. Fluid motion within the ellipse is integrable and the fluid particles follow circular trajectories. The flow exterior to the ellipse is not integrable, and trajectories must be computed numerically.

Polvani proposed that the Kida vortex serves as an excellent model for flow surrounding an elliptical storm in the atmosphere of Neptune – a storm known as Neptune's "Great Dark Spot", not unlike the "Great Red Spot" on Jupiter [Polvani 1990].[1] Using spacecraft imagery of the storm, they measured the evolution of the elliptical storm region, and assuming the Kida vortex model as a valid description of the flow, inferred the vorticity within the storm, as well as the background strain rates.

Here, we use the FTLE-LCS method to study the transport structures surrounding the Kida vortex. The system is akin to the perturbed pendulum, in that the Eulerian

[1]Neptune's Great Dark Spot has subsequently disappeared; however, during its lifetime, it exhibited the fastest winds ever recorded in the solar system.

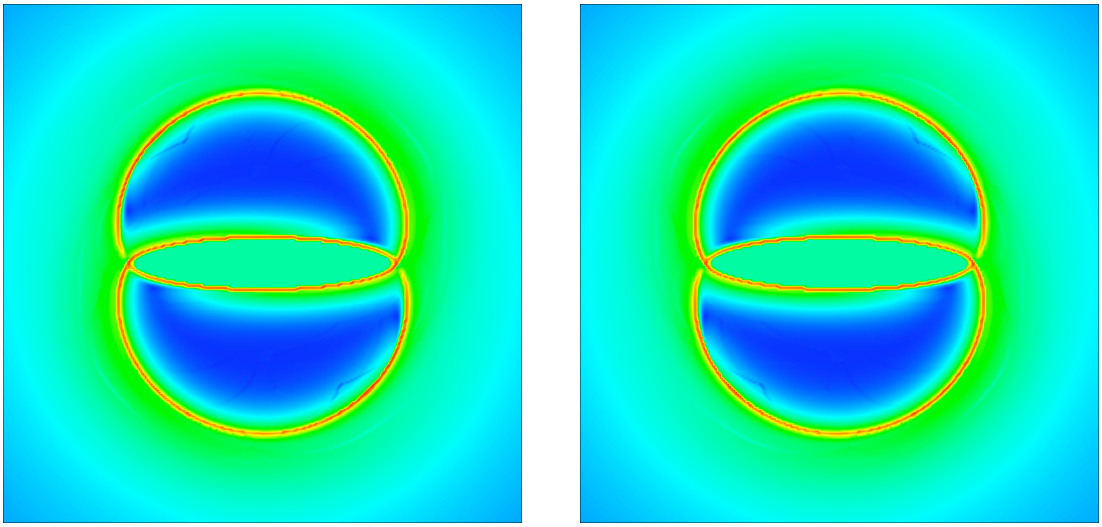

(a) (b)

Figure 5.1: The repelling (a) and attracting (b) FTLE fields for Kirchoff's ellipse. This represents an unperturbed case in which the repelling and attracting LCS coincide, clearly demarcating an interior and exterior region.

velocity and vorticity fields yield little insight into Lagrangian transport structures.

The FTLE computed for the flow of a Kirchoff ellipse are shown in Figure 5.1 – recall that the ellipse remains unchanged in time and rotates with uniform angular velocity. The repelling and attracting LCS coincide to resemble a heteroclinic connection that separates the far-field quiescent flow from the region that rotates with the ellipse. The addition of a background linear flow introduces a perturbation that leads to the LCS in Figure 5.2. The intersection of the repelling and attracting LCS now indicate homoclinic-type points – the number of which goes to infinity as the integration time is increased. The LCS define lobe regions that are entrained and detrained in the flow surrounding the ellipse, indicating that the linear background flow enhances mixing through the mechanism of lobe dynamics.

5.2 The ellipsoidal vortex

We now proceed from the Kida vortex to a three-dimensional ellipsoidal model for a special class of oceanic eddies. Mediterranean eddies (or *meddies* as they are referred

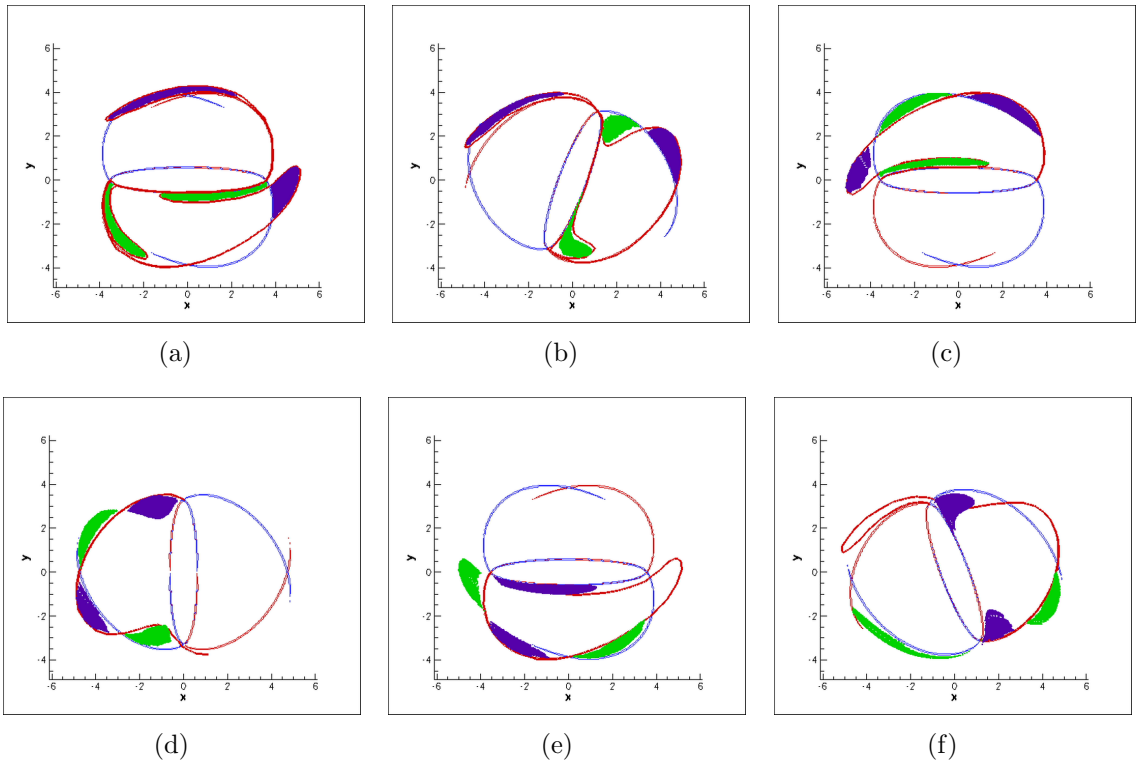

(a) (b) (c)

(d) (e) (f)

Figure 5.2: Snapshots of the repelling and attracting LCS are shown here in red and blue, respectively. The lobes defined by their intersections are filled with drifters: green drifters start inside the vortical region, while purple drifters start outside. Under the action of the time-dependent rotating homoclinic tangle, the green drifters are detrained while purple drifters are entrained.

to in the oceanographic comunity) are an interesting oceanic phenomenon in which dense salty water exits the Mediterranean Sea through the Straits of Gibraltar and descends into deeper water in the North Atlantic. Frictional and Coriolis effects induce rotation, resulting in a coherent eddy of high salinity with a typical radius of 100km at a depth of 1km [Armi 1989]. The three-dimensional eddy has the shape of an oblate ellipsoid, and hence is often referred to as a *salt lens*. The remarkable property of these eddies is that they retain their coherent shape and salinity, and have been tracked for several years as they migrate across the Atlantic toward the Carribbean.

A simple fluid model for the flow of these eddies has been proposed by [Meacham 1994], and an excellent treatment of the model can be found in [McKiver 2003]. The eddy model is a particular solution to a quasi-geostrophic model that approximates flow in rotating stratified flows. In the quasi-geostrophic model, the flow is entirely determined by the advection of a scalar quantity, the potential vorticity: $q(\mathbf{x}, t)$. Assuming constant values for the Coriolis and buoyancy frequencies yields the following simplified system:

$$\frac{dq(\mathbf{x},t)}{dt} = \frac{\partial q(\mathbf{x},t)}{\partial t} + \mathbf{u}\cdot\nabla q(\mathbf{x},t) = 0\,, \tag{5.11}$$

$$\nabla^2\psi = q(\mathbf{x},t)\,, \tag{5.12}$$

$$\mathbf{u}(\mathbf{x},t) = (u,v,w) = \left(-\frac{\partial\psi}{\partial y}, \frac{\partial\psi}{\partial x}, 0\right)\,. \tag{5.13}$$

Meacham has shown that an ellipsoidal patch of constant vorticity placed in a background linear shear flow is an exact solution to this system. Under the action of the background flow, the aspect ratios of the ellipsoid change, but the ellipsoid nevertheless remains ellipsoidal while undergoing chaotic motions of rotation and nutation. The ellipsoidal solution for the three-dimensional quasi-geostrophic equations has an interesting counterpart in the gravitational potential theory of Laplace, and was also treated by Chandresekar [Chandrasekhar 1969].

Our purpose in studying this model with LCS is to understand the geometry

of particle transport surrounding the ellipsoid. Figure 5.3(b) indicates the shape of drifter flow surrounding the ellipse – an animation of which does not immediately reveal insight in the transport mechanism at work.

Figures 5.3(c) and 5.3(d) provide a side and top view of both the attracting and repelling LCS (now two-dimensional surfaces) surrounding the ellipsoid. Immediately, we perceive that the flow surrounding the ellipsoid resembles flow in the perturbed pendulum in that the perturbation provided by the background shear causes the formation of lobes, and that the mechanism by which fluid is transported into the vicinity of the ellipsoid is through the mechanism of lobe dynamics. Computing the volume of the lobes and the rate at which they form provides an indication of the rate at which mixing is occurring in the flow. Again, the background linear flow introduces a perturbation that induces and enhances transport via lobe dynamics.

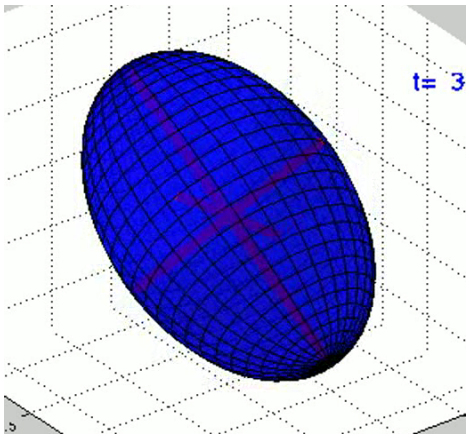

(a) The meddy is modeled as an ellipsoidal patch of constant vorticity in a linear shear flow. The ellipsoid undergoes rotation, nutation, and changes in aspect ratio.

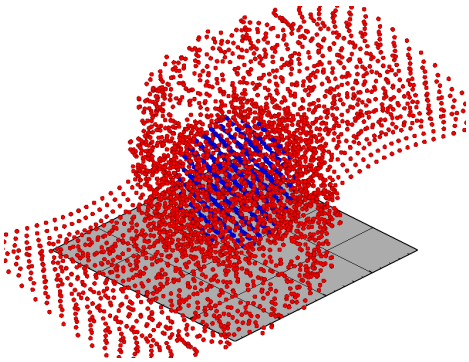

(b) Drifters in the flow surrounding the ellipsoid. Blue particles are inside the ellipsoid and have integrable dynamics. Simply watching the movement of tracers does not reveal the transport mechanism outside the ellipsoid.

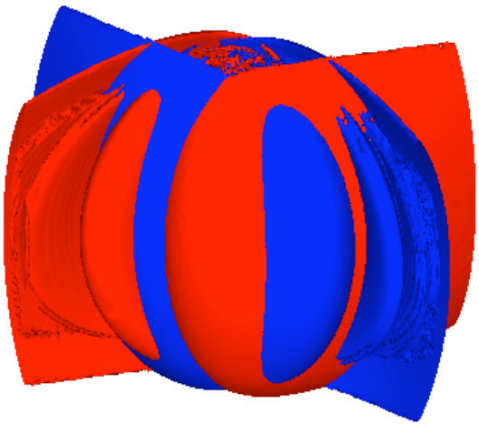

(c) Side view of the repelling (red) and attracting (blue) LCS in the the flow surrounding the ellipsoid. In time, the blue lobes are detrained out of the interior, while red lobes are entrained.

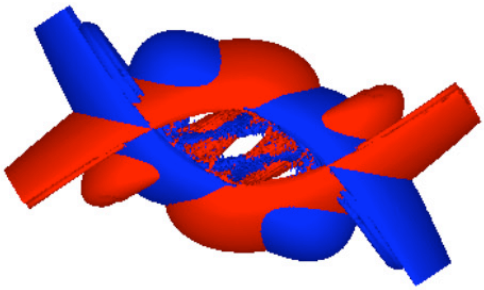

(d) Top view of the LCS in the flow surrounding the ellipsoid.

Figure 5.3: LCS in a quasi-geostrophic model for Mediterranean eddies.

Chapter 6

LCS and Hurricanes

In this chapter, we apply the method of using FTLE to extract Lagrangian Coherent Structures (LCS) in the manifestly turbulent wind-field data for hurricanes. A main result is the discovery of sharply defined surfaces in the flow surrounding the hurricane that govern transport of air both into and out of the storm. Furthermore, the evolution of these surfaces indicate very plainly that transport in the large-scale flow occurs via the mechanism of lobe dynamics, associated with a homoclinic tangle. The LCS method reveals that transport in hurricanes is a low-dimensional process whose salient features are adequately described by a very simple two-dimensional kinematic model that exhibits a chaotic tangle concomitant with a perturbed homoclinic connection.

We begin with an application of the LCS method to a simple kinematic model for hurricane flow. Results for the simple model will provide an insightful visual comparison with the LCS results for the actual hurricane data set. Clear similarities between the LCS in the model, and the LCS in the reanalysis data will underscore the low-dimensionality of the transport process in the hurricane flow.

6.1 Transport in a simple kinematic model

The kinematic model consists of analytic expressions for the velocity field of a single vortex in a two-dimensional uniform background flow. The velocity components of

the background flow are modeled by

$$\begin{aligned} u_b &= -\beta \\ v_b &= 0\,, \end{aligned}$$

with $\beta > 0$ so that the flow is from right to left.

The velocity field for a vortex with counter-clockwise flow centered at y_0 on the y-axis is given by

$$\begin{aligned} u_v &= \frac{-(y-y_0)}{x^2+(y-y_0)^2+\alpha} \\ v_v &= \frac{x}{x^2+(y-y_0)^2+\alpha}\,. \end{aligned}$$

Notice that the influence of the vortex decays like the inverse square of the distance from the vortex center, and that $\alpha > 0$ regularizes the velocity field at the vortex center. For the computations that follow, we take $\alpha = 0.1$.

We also consider a time-dependent forcing term of the form

$$\begin{aligned} u_f &= 0 \\ v_f &= \epsilon\, y \cos 2t\,. \end{aligned}$$

Addition of these three terms yields a very simple kinematic model for a periodically perturbed vortex in a uniform background flow:

$$\begin{aligned} u &= \frac{-(y-y_0)}{x^2+(y-y_0)^2+\alpha} - \beta \\ v &= \frac{x}{x^2+(y-y_0)^2+\alpha} + \epsilon\, y \cos 2t\,. \end{aligned} \tag{6.1}$$

Variations of system (6.1) are often provided in dynamical systems texts to illustrate a system with a homoclinic connection (as shall be verified in the next subsection). Choosing

$$\beta = \frac{1}{\sqrt{1+4\alpha}} \quad \text{and} \quad y_0 = \frac{1+\sqrt{1+4\alpha}}{2}$$

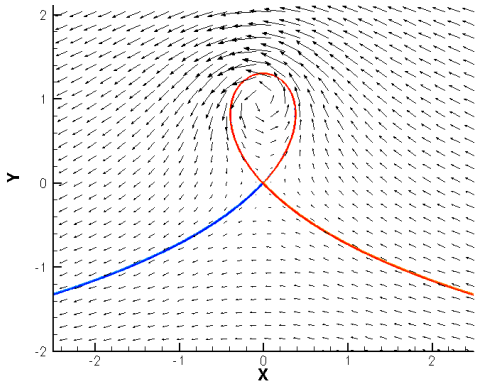

Figure 6.1: The velocity field and LCS for the unforced model. In the homoclinic loop attached to the origin, the repelling LCS (red) and the attracting LCS (blue) are exactly coincident (and hence the attracting LCS is masked by the repelling LCS). We observe here that the LCS reproduce the usual notions of stable and unstable manifolds for time-independent systems.

for a given value of α ensures that the fixed points in the unperturbed flow occur at (0,0) and the point (0,1) as can be easily verified.

6.1.1 Unforced case

In the unforced case ($\epsilon = 0$), the system is time-independent. The velocity field and both the repelling and attracting LCS (computed using an integration time of 10 time units) are plotted in Figure 6.1. The LCS reveal a homoclinic manifold, and coincide with the stable and unstable manifolds associated with the fixed point at the origin.

6.1.2 Forced case

We now include a relatively large forcing term by setting $\epsilon = 0.5$. The perturbation causes the intersection of the stable and unstable manifolds. As we have seen before, a single intersection induces an infinite number of intersections as the integration time is increased, and the intersections of the manifolds define lobes. Transport into and out of the region defined by the homoclinic trajectory is entirely determined by the evolution of these lobes through the action of lobe dynamics.

Figure 6.2 provides snapshots of the velocity field of the forced vortex at $t = \{0, \frac{\pi}{4}, \frac{\pi}{2}, \frac{3\pi}{4}\}$. Here we see another example where inspection of the Eulerian velocity

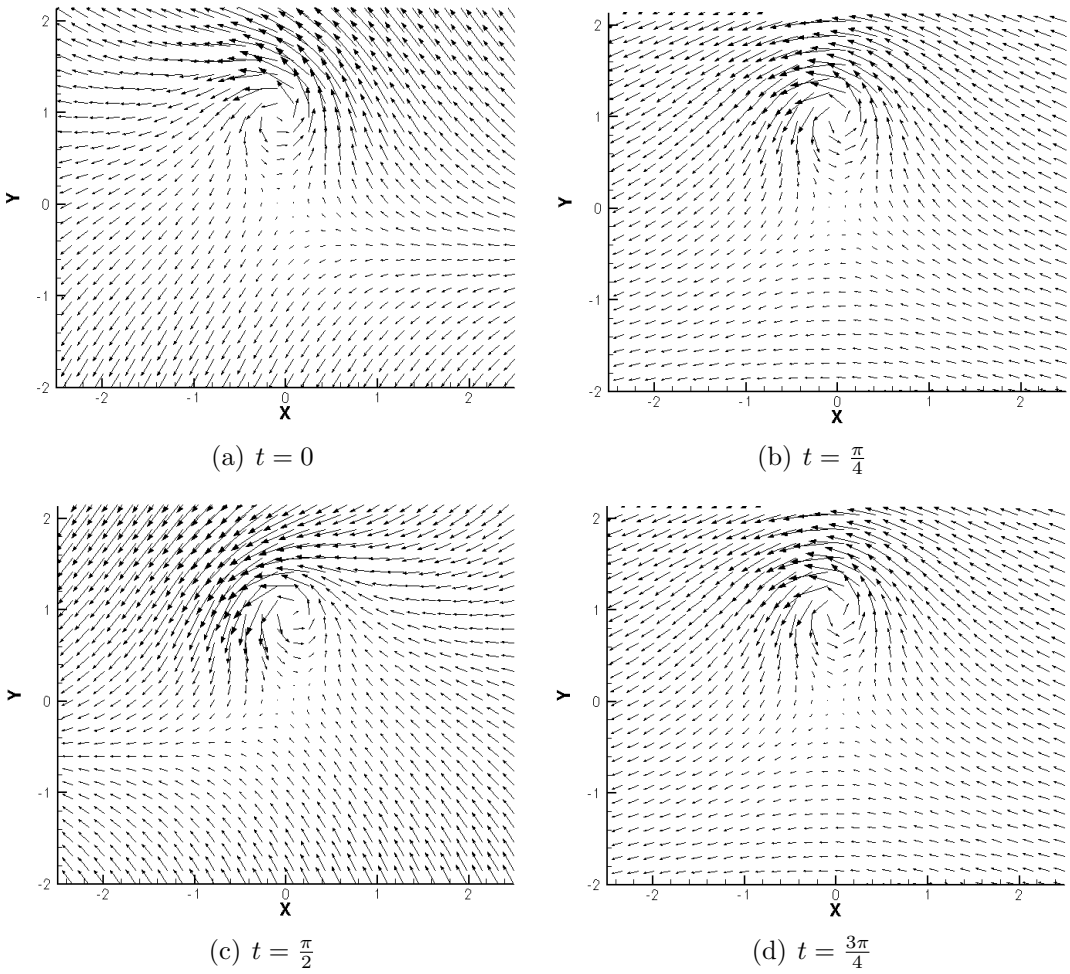

(a) $t = 0$ (b) $t = \frac{\pi}{4}$

(c) $t = \frac{\pi}{2}$ (d) $t = \frac{3\pi}{4}$

Figure 6.2: Snapshots of the velocity field in the forced model at regular intervals in time. Discerning the important transport mechanisms from snapshots of the Eulerian velocity field is not intuitive.

field alone does not elucidate the Lagrangian transport structures induced by the flow. Computation of the LCS for the forced system provides a visualization of the homoclinic tangle and consequently the transport process that occurs via lobe dynamics.

Snapshots of the LCS computed for the forced system using an integration time of 10 time units are shown in Figure 6.3. Placing passive drifters inside a lobe reveals the action of lobe dynamics. The lobe containing blue drifters is detrained out of the vortex, while the lobe containing red drifters is entrained into the vortex.

Since the forcing is periodic, the method of Poincaré maps can also be used to

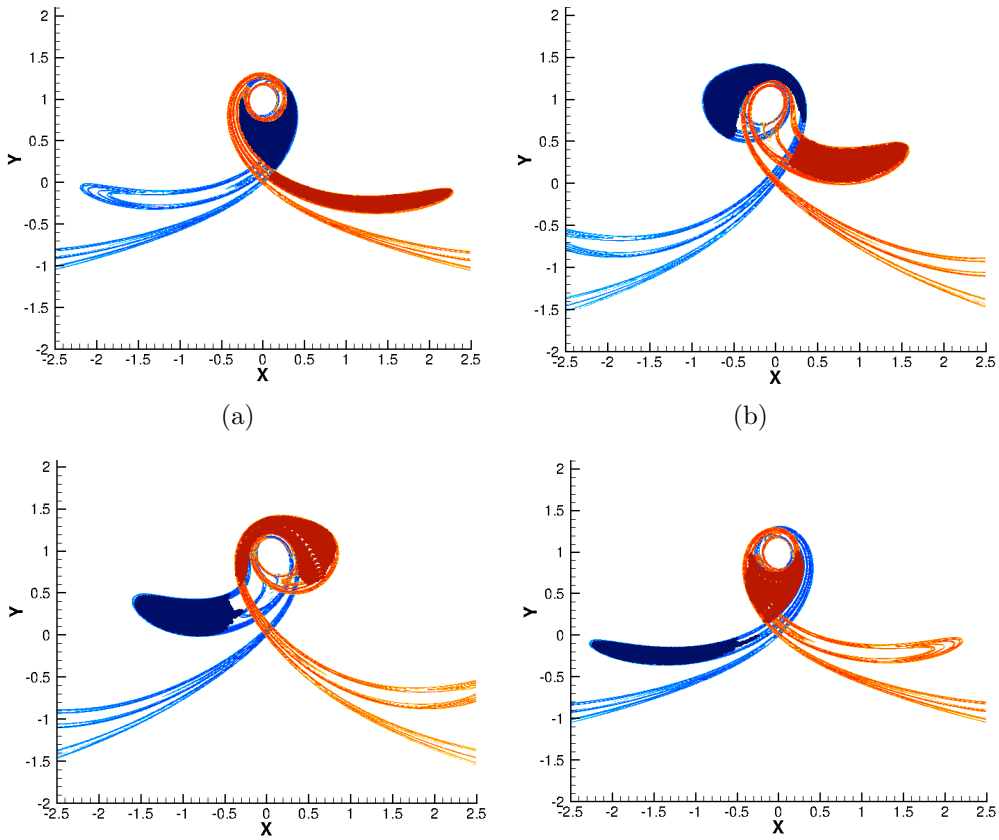

Figure 6.3: The LCS structures computed for the flow in a simple kinematic model for a periodically perturbed vortex in a linear background flow reveals a homoclinic tangle, and that transport occurs via lobe dynamics: the lobe containing red drifters is advected into the vortex, while the lobe containing blue drifters is detrained out of the vortex.

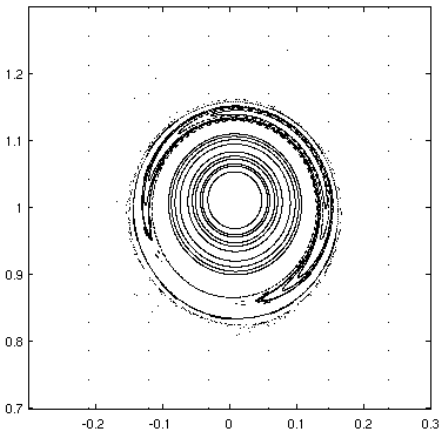

Figure 6.4: The Poincaré map computed for the simple kinematic model reveals the resonant region associated with the "eye" of the vortex as outlined by the LCS in 6.3(a). Outside the resonance region, the action of the lobes induces chaotic flow that leads trajectories to be advected out of the domain by the background flow. The map is visualized by advecting a 15×15 grid of points for 1000 periods of the forcing and plotting their locations.

analyze this flow (Figure 6.4). Analyzing the stable and unstable manifolds of the discrete map provides the intersecting manifolds and consequent lobes. Repeating this procedure over a range of starting times during the period of the perturbation reveals the evolution of the lobes. The LCS method is an entirely different approach that recovers the same result, yet has the important added feature that it can be used for systems with arbitrary time dependence (such as the raw hurricane data to be analyzed next).

The central core of the vortex in Figures 6.3(a) through 6.3(d) remains untouched by the action of the lobes and appears as a *resonance island* in the corresponding Poincaré map. Figure 6.4 shows the Poincaré map computed for this flow and depicts the resonance island that corresponds to the "eye" of the vortex in Figure 6.3(a). The LCS method indicates how the *chaotic sea* surrounding the resonance region in the Poincaré map is formed by the repeated stretching, folding, and intersection of the lobes.

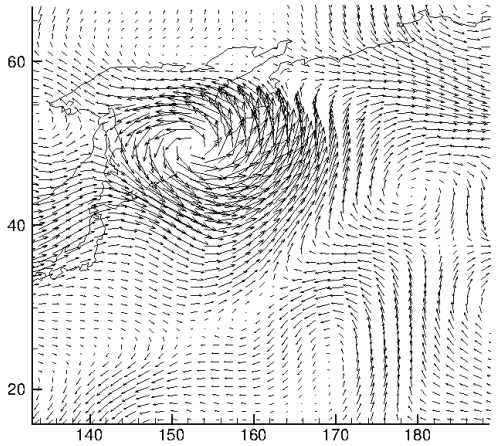

Figure 6.5: Snapshot of the velocity field above the Western Pacific at the 850mb pressure level provided by the NCAR-NCEP reanalysis data set. The prominent vortical flow indicates the flow associated with Typhoon Nabi (2005).

6.2 Transport in Typhoon Nabi

Next, we apply the method of LCS to extract coherent structures in velocity field data for a Pacific typhoon. The data is obtained from the publicly accessible NCAR-NCEP repository at `http://www.cdc.noaa.gov/cdc/data.ncep.reanalysis.html`. Specifically, we use the two-dimensional velocity field at the 850mb pressure level over the Western Pacific for late Summer of 2005. The typhoon of interest during this period is Typhoon Nabi, a category 5 tropical storm, that made landfall in Japan on September 6, 2005. A snapshot of the velocity field provided in the data set is shown in Figure 6.5.

Computation of the FTLE was performed with an integration time $T = 120$ hours. Snapshots depicting both the repelling and attracting LCS are shown in Figure 6.6. Despite the complex flow surrounding the typhoon, we readily observe that the repelling and attracting LCS accurately capture the boundary of the storm vortex, and has the shape of a homoclinic connection seen previously in the simple model. Furthermore, the evolution of the LCS reveals that the transport mechanism that governs entrainment into and detrainment out of the typhoon across this boundary is indeed lobe dynamics. For example, the region of fluid colored brown and enclosed by the intersection of the repelling and attracting LCS is a lobe that will be detrained out

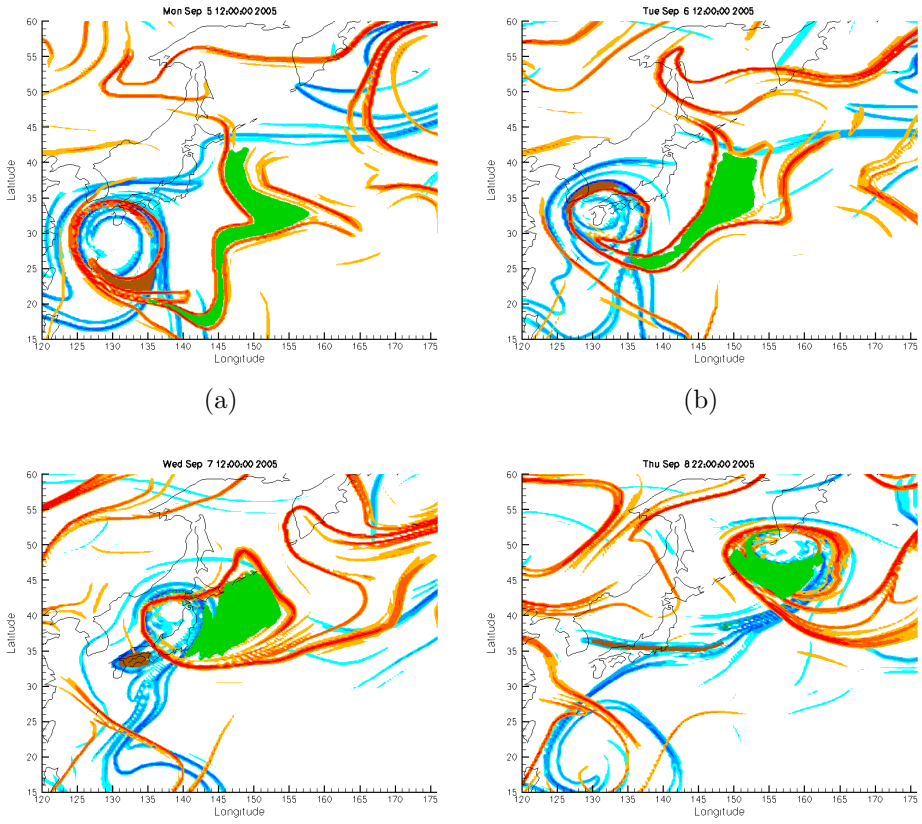

Figure 6.6: LCS for typhoon Nabi, computed from NCEP-NCAR Reanalysis Data at the 850mb pressure level. The intersections of the repelling (red) and attracting (blue) LCS define lobes that enclose regions of fluid that will be either entrained into or detrained out of the cyclone. For clarity, only two lobes have been colored although many more are evident during the animation. The LCS reveals that transport into and out of the cyclone is well-described by lobe dynamics. Indeed, the LCS forms a boundary to the cyclone that is exactly a homoclinic tangle from dynamical systems theory. Over the three day period shown, the green lobe is entrained, while the brown lobe is detrained.

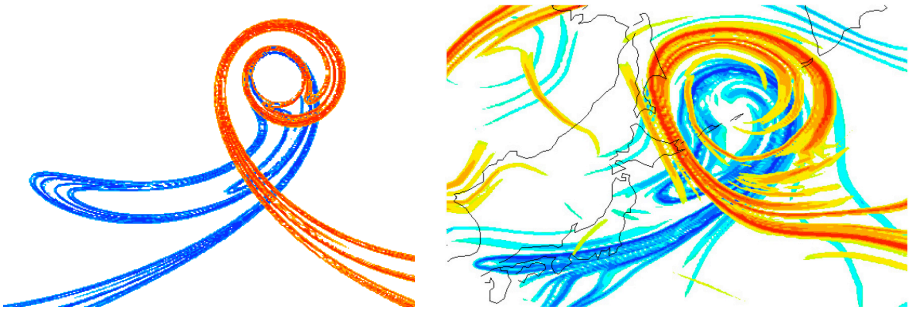

(a) LCS in the kinematic model (b) LCS in Typhoon Nabi.

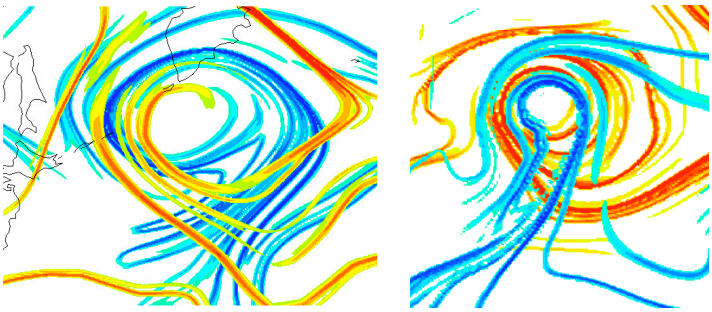

(c) LCS in Typhoon Banyan (d) LCS in Typhoon Tip

Figure 6.7: The LCS computed for the simple kinematic model is shown in (a) and compared with the LCS computed for the wind fields in three Pacific typhoons (b)-(d). The homoclinic tangle structure is evident in all three storms and indicates that lobe dynamics is a dominant transport structure in tropical storms.

of the hurricane, while the region colored green is a lobe that will be entrained into the storm. Without computing the LCS, the location of the boundary to the storm is not clear, and hence the concepts of detrainment and entrainment are ill-defined. In the literature, plots of vorticity and humidity are typically provided to indicate the size and location of a storm. These quantities are correlated with the motion of the vortex, but do not provide sharp well-defined boundaries, and consequently the transport mechanisms cannot be inferred.

Computations of the LCS for several typhoons have revealed that mixing via lobes in a homoclinic tangle is a generically dominant feature in tropical storms. Figure 6.7 shows the homoclinic tangles revealed via FTLE computations for Pacific Typhoons Tip (1979), Banyan (2005), and Nabi (2005) with the homoclinic tangle computed in the flow of the simple kinematic model provided for comparison.

The similarity between the LCS computed for Typhoon Nabi wind-field data and

the LCS computed for the simple kinematic model is quite striking. Comparing Figures 6.3(a) and 6.6(a), we see that in both cases the LCS define a boundary to the vortex, as well as lobes both inside and outside this boundary. Comparing the final figures in each sequence (Figures 6.3(d) and 6.6(d)) reveals that in both cases, the LCS dictate how the lobes will be transported by the flow, and how the processes of entrainment and detrainment from the vortex will occur. The similarity between the transport processes is most easily appreciated when the LCS are viewed as an animated movie, rather than as a sequence of individual frames. In the movies, we see that the structure of the flows is remarkably similar despite the complexity of the atmospheric flow compared with the low-dimensionalty of the simple model. Computations of the LCS allow us to not only identify and characterize the dominant transport mechanism in hurricane flows, but also to observe that the essential structure of that transport mechanism can be faithfully reproduced by a simple low-dimensional model.

We remark also that careful study of the LCS computed for hurricane flows at fine detail reveals all the intricacies of the homoclinic tangle as studied theoretically in geometric mechanics. For instance, the action of the Smale horseshoe map and the first iteration in the formation of a Cantor set can be plainly discerned in the evolution of the LCS. As in our discussion in Chapter 2, these concepts are typically studied with regard to the Poincaré maps of periodically perturbed systems and are presented in abstraction, whereas here we see that the FTLE method for extracting LCS uncovers these very same notions in the seemingly unrelated turbulent and aperiodic flows of actual hurricane data, and presents them in a way that their evolution can be observed naturally through animation. Figure 6.8 illustrates how the central "third" region (shaded brown) is advected out of the storm, while the outer two "thirds" (shaded green) remain inside the storm, just as is prescribed by a single iteration of the Smale horseshoe map in the formation of the Cantor set.

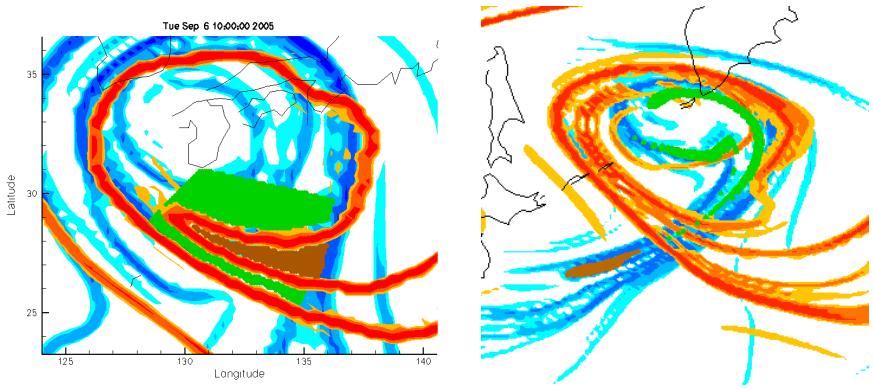

(a) (b)

Figure 6.8: The action of lobe dynamics in the homoclinic tangle induces a map that, as has been shown by Smale, leads to the formation of a Cantor set when iterated. Here we see the first iteration of the horseshoe map in the flow of the typhoon: the middle 'third', colored brown, is removed from the storm, while the two green outer 'thirds' remain.

6.3 Eye-wall structures in Hurricane Isabel

The study of flow in Typhoon Nabi was concerned with synoptic-scale flow. We now consider three-dimensional flow in the vicinity of a hurricane eye-wall. Recent observational data obtained during hurricanes Katrina (2005) and Rita (2005) indicate that storm intensity is intricately related to fine-scale processes such as *eyewall replacement* — a process in which the eyewall of a storm disintegrates and is replaced by an eyewall of larger radius and lower wind speed, resulting in decreased intensity [Houze 2007]. As was the case with Hurricane Rita, the new eyewall can subsequently contract, causing rapid storm intensification. This process of rapid intensity fluctuation has also been observed in high-resolution model data [Chen 2007, Houze 2007]. These observations emphasize that an understanding of the detailed dynamics of the hurricane eyewall is crucial to accurate predictions of storm intensity. Furthermore, the stability of a hurricane, and whether it will tend to decay or intensify, is dependent to some degree on the moisture and energy content of the air parcels it entrains from the large-scale flow. Hence, an understanding of the transport structures and mechanisms within the hurricane is a prerequisite for accurate intensity prediction. A lack of understanding with regard to the structural dynamics and transport processes

in hurricanes could well be part of the explanation for the current inability among the forecasting community to decrease intensity prediction errors despite exponentially increasing computing power[1].

In a three-dimensional flow model for Hurricane Isabel (2003) computed using the WRF model [Kuo 2003], LCS proves to be an effective method for analyzing transport structures near the eyewall. Figure 6.9 shows the extracted eyewall as visualized using LCS. Meteorologists typically define the eyewall as the locations of maximum wind speed on rays emanating from the eye of the storm. This definition, although simple to visualize, is an intrinsically Eulerian approach that, as has been shown in many applications, fails to capture the Lagrangian quantities necessary to understand transport in time-dependent flows [Shadden 2007]. Recently, attempts have been made to determine the instantaneous vortex filament about which the hurricane is rotating; however, this approach yields only the center of the vortex and no information about transport in the flow [Weinkauf 2007]. LCS, on the other hand, necessarily encodes information about the Lagrangian transport of tracers within the flow and is a rigorous barrier to transport. Thus, the surface revealed by the LCS is a precise definition of the eyewall that is consistent with the Lagrangian dynamics of the flow.

The insights into transport near the hurricane eyewall provided by the LCS are readily discerned by observing the trajectories of passive drifters placed in the various regions delineated by the LCS. For example, Figure 6.10 indicates drifters with initial positions located inside the eyewall (red) and outside the eyewall (blue). When these drifters are advected by the flow, as depicted in Figure 6.11, the red drifters remain inside the eye of the storm while the blue drifters are ejected from the storm into the upper atmosphere.

The green drifters are initially located in a lobe region protruding from the south-western edge of the eye. This lobe region represents air mass that will be detrained from the eye region and eventually ejected into the upper atmosphere, as evidenced by the trajectories of the green drifters. Already, we begin to see that the LCS

[1]See the forecast error analysis at `http://www.nhc.noaa.gov/verification/verify5.shtml`

summarizes and describes the transport processes near the eyewall.

It is hoped that the insights gained from further explorations in both the large-scale and the near-eyewall flow will directly inform the development of improved hurricane modeling and forecasting, as well as the types and locations of *in situ* data measurements (using dropsondes, for example) that will allow for optimal data collection, and the most accurate prediction of storm evolution.

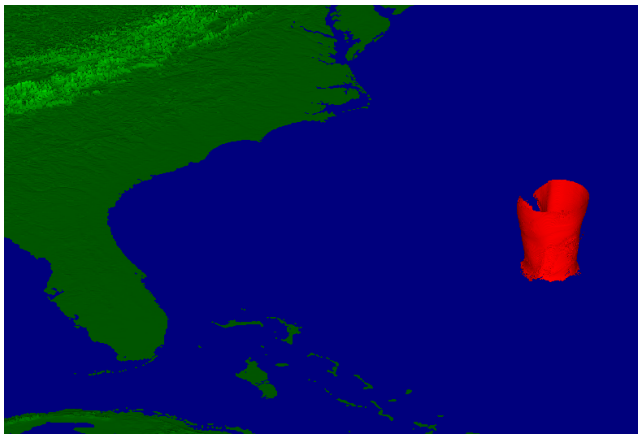

(a) The eyewall of Hurricane Isabel as visualized using the repelling LCS. The eyewall reaches an approximate height of 8km above sea-level.

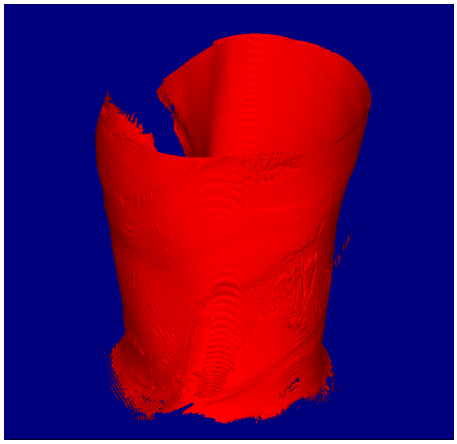

(b) Side view.

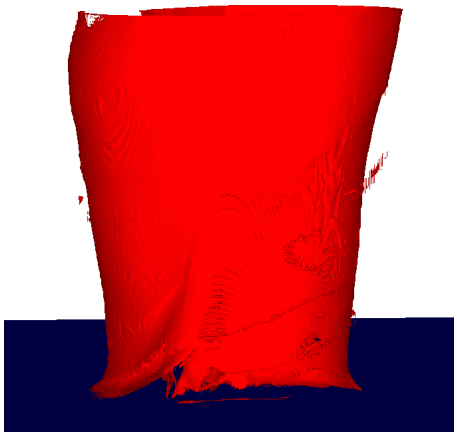

(c) View from the ocean surface.

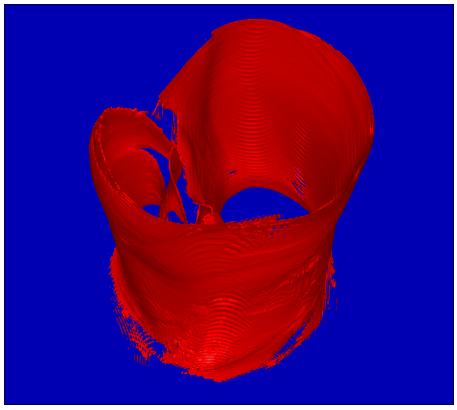

(d) Oblique view from above.

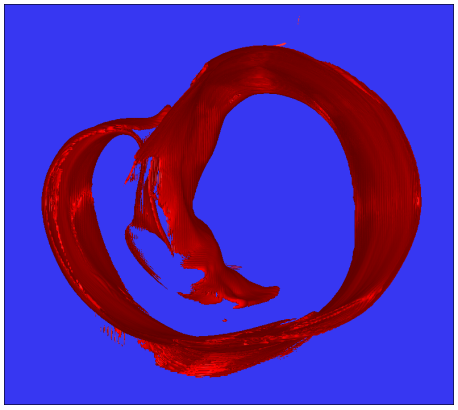

(e) Top view indicating a lobe structure protruding from the southwest corner of the main eye region.

Figure 6.9: The repelling LCS reveals the precise location and structure of the eyewall for Hurricane Isabel (2003). Figure 6.9(a) shows the eyewall in the Atlantic during the approach of Hurricane Isabel to the mainland, while figures 6.9(b)-6.9(e) show the three-dimensional structure of the eyewall from various viewpoints.

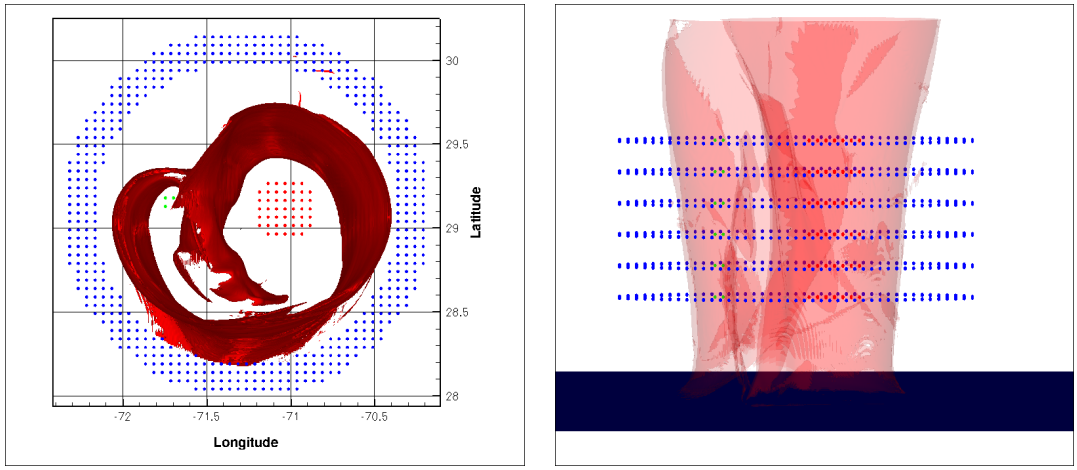

(a) Top view.

(b) Side view.

Figure 6.10: The eyewall, as revealed by the LCS, is a coherent structure that governs transport near the eye of the hurricane. This property is revealed by placing passive drifters in the different regions defined by the LCS and observing their trajectories under the action of the flow. The initial placement of the drifters is shown here: red drifters are placed well inside the eyewall, green drifters are placed in a lobe structure that will be detrained from the eye, and an annulus of blue drifters is placed outside the eyewall.

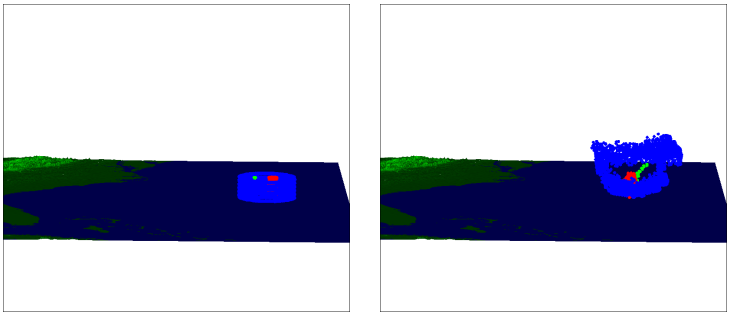

(a) t = 0.0 hrs

(b) t = 6.0 hrs

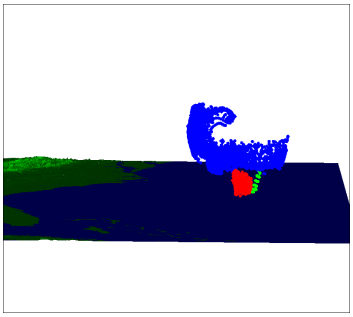

(c) t = 9.0 hrs

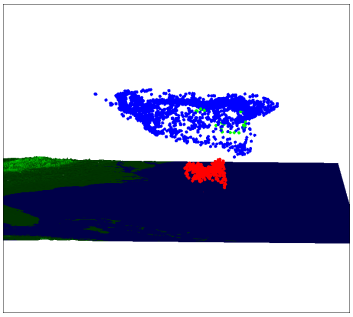

(d) t = 20.4 hrs

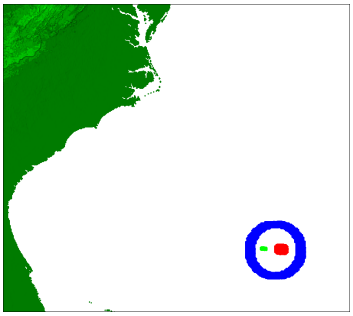

(e) t=0.0 hrs

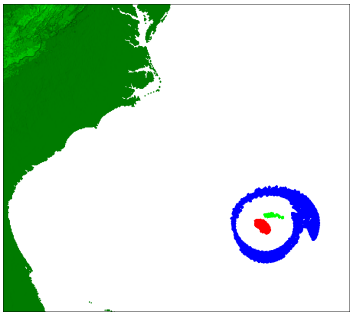

(f) t = 6.0 hrs

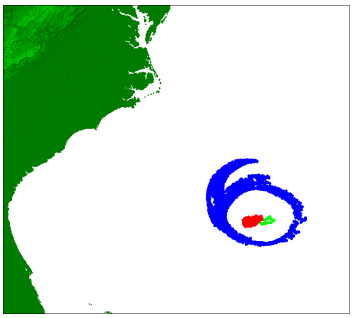

(g) t = 9.0 hrs

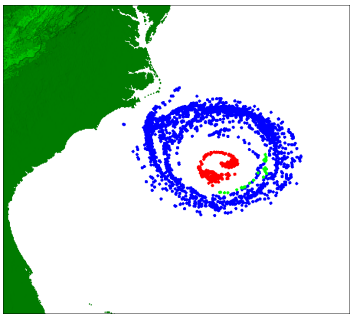

(h) t = 20.4 hrs

Figure 6.11: The drifters initially placed as depicted in Figure 6.10 (notice that they are strategically placed relative to the LCS) are advected forward in the flow. Snapshots of the drifter trajectories are shown here from above and from the side. Red particles within the eyewall remain near the ocean surface, while the blue particles are ejected into the upper atmosphere. The green particles are eventually detrained from the eye, and follow the blue drifters into the upper atmosphere.

Chapter 7

LCS and the Global Ocean

The Intergovernmental Panel on Climate Change (IPCC) has declaratively assessed that "warming of the climate system is unequivocal" and that "many natural systems are being affected by regional climate changes" [Solomon 2007]. Addressing climate change through accurate global climate prediction and sustainable engineering is arguably the most important scientific challenge of the twenty-first century.

Mesoscale eddies account for the majority of kinetic energy in the global ocean, and are largely responsible for the dispersion of heat and mass [Li 2008]. Chelton has similarly observed that more than fifty percent of ocean variability in satellite data is due to mesoscale eddies [Chelton 2007]. Consequently, accurate modeling of eddy activity, and the effect it has on heat budgets in the ocean, is imperative for faithful predictions of global climate. Yet, in the recent *Fourth Assessment Report of the IPCC* [Solomon 2007], only one of the twenty-four global climate models explicitly simulated mesoscale eddy activity [Bryan 2008]. Constraints on computing power, and the need for ensemble averages over long time scales, necessitate model simulations at large enough gridscales that only the large-scale laminar flow is captured, while the effects of unresolved eddies are included entirely by modeling, or *parameterization*. In a recent *Nature* article, Scheiermeier has observed that the wealth of ocean data now available from satellites and globally deployed drifters has confirmed the important role of mesoscale eddies in transport and stirring, and also revealed that widely-used model parameterizations of mesoscale eddies (variations of the Gent-McWilliams scheme introduced in 1990 are most commonly used [Gent 1990]) fail

to capture eddy mixing accurately [Schiermeier 2007]. Most notably, parameterizations of eddy stirring are typically employed uniformly under the assumption that stirring is homogeneous throughout the ocean; an assumption that the data now reveals is a significant weakness of ocean models. Although parameterizations have led to many modeling improvements, discrepancies between ocean observations and the parametrized models are not unexpected since the parameterization schemes were developed primarily using theoretical considerations of the primitive equations without access to large sets of ocean data or eddy-resolving models. For this reason, parameterizations fail to capture the influence of unresolved topography, bottom drag, and regionally specific sensitivities to variations in parameters [Fox-Kemper 2008].

Similarly, the energy exchange between the ocean and atmosphere reveals a rich interplay between rising ocean temperatures and the frequency and intensity of tropical storms, and motivates the need to more fully understand parameterization of transport and flux rates in the atmosphere as well. Emanuel, for instance, has proposed (not without controversy) that the rise in ocean temperatures has led to increased intensity of tropical storms, which in turn drives mixing in the ocean [Emanuel 2001, Emanuel 2007].

Increased computing power has recently permitted the advent of *eddy-resolving* global simulations; however, ensemble runs of climate-length simulations at eddy-resolving resolutions will not be feasible in the foreseeable future [Hecht 2008a]. Nevertheless, the availability of high resolution models, at least on short time scales, and the stream of new observational data is a boon not previously enjoyed by ocean modelers. To this end, the UK Meteorological Office hosted a "Workshop on Mesoscale Eddies" in April, 2009, with the stated purpose of "educating the research community regarding the importance of mesoscale eddies" and to "identify best practices for parameterizing ocean mesoscale eddies in coarse resolution climate models, and to discuss various research avenues for improved parameterizations" [1].

Certainly the use of LCS has a role to play in providing insight in to the regional

[1] See the Workshop webpage online at `http://www.metoffice.gov.uk/conference/mesoscale_workshop/`

variation of eddy activity and mixing, and revealing the mechanisms by which mixing occurs. Initial results in this regard are promising. The LCS are barriers to transport that define the boundaries to eddies and reveal the pathways for transport. Moreover, the LCS analysis provides a visualization of the transport mechanisms induced by mesoscale eddies, thus providing a clearer understanding of the mixing process. The transport mechanisms revealed in this way are turbulent, but their underlying structure is remarkably low-dimensional.

We begin our study of global ocean currents by investigating an idealized model for flow in the Antarctic Circumpolar Current. We then proceed to an investigation of reanalysis data for the global ocean.

7.1 A model for the Antarctic Circumpolar Current

The Antarctic Circumpolar Current is the only major ocean current that flows continuously without impinging on a continental shelf, and is an important component in the ocean "conveyor belt" that transfers heat energy and momentum between the major ocean basins. The current carries both warm water at its surface, as well as cool waters in its deep bottom currents. In [Hecht 2008a, Hecht 2008b], Hecht presented a Lagrangian-Averaged Navier Stokes (LANS-α) model for ocean flow, and applied the model to flow in a three-dimensional channel that idealizes the Antarctic Circumpolar Current. The channel used in the model has solid rectangular sides in the zonal directions, and the boundary conditions at the open ends are determined by reentrant flow which flows predominantly from West to East. The model includes wind and thermal forcing at the surface. The topography along the bottom of the channel includes a deep sea ridge, the effect of which is to induce northward flow immediately before the ridge, and southward flow immediately after the ridge. During the course of this meandering flow, eddies are produced that induce stirring and mixing. The intent of [Hecht 2008b] was to confirm that the LANS-α model captures

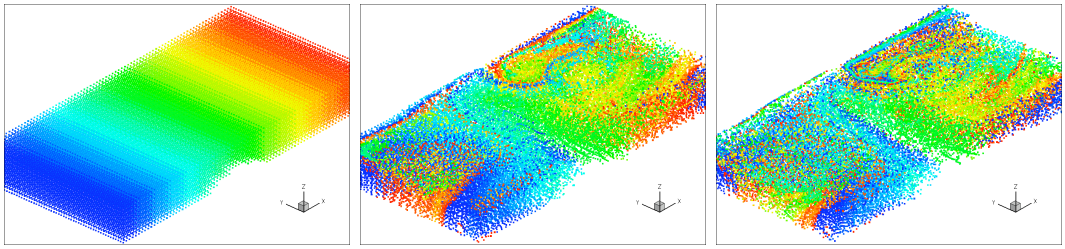

(a) (b) (c)

Figure 7.1: Snapshots of drifter trajectories in the idealized channel model of the Antarctic Circumpolar Current. The drifters are colored by their initial longitude, and flow is predominantly from West to East. A North-South ridge in the topography can be seen near the center of the channel. After a short time (less than the time for the majority of particles to travel the length of the channel), the drifters appear well-mixed.

the energy cascades to smaller scales correctly so that eddies are produced (a major problem with many coarse-grid ocean models is that they capture insufficient eddy kinetic energy.)

Our purpose, will be to study the transport structures that are responsible for mediating mixing in this channel flow. Simulation of passive drifters reveals that the turbulent flow due to the deep sea ridge quickly induces mixing of particle trajectories. Figure 7.1 shows three frames in the simulation of trajectories, in which drifters are colored by their initial zonal location. The final figure indicates that the particles are well-mixed, and the hypothesis that the mixing is fully turbulent and well-modeled by diffusion or a random walk appears valid. The computation of the LCS, however, reveals a different picture.

Figures 7.2(a) and 7.2(b) depict the FTLE scalar field for the channel flow model, colored so that the LCS appear as white curves. Considering the complexity of the flow, the low dimensionality, coherence, and stability of the resulting flow structures are quite surprising. The LCS reveal the boundaries of several major eddy structures that in concert provide the stirring mechanisms that induce the chaotic drifter trajectories. Some of the eddies pair into doublets that are reminiscent of familiar flows in dynamical systems texts such as the Duffing oscillator. The overall eddy structure is remarkably stable to perturbations in the flow. In fact, the perturbations

allow for exchange of drifters between the eddies through lobe dynamics and enhance mixing in the same manner we have observed previously in the perturbed pendulum. Here we observe that the LCS provide the "skeleton" of turbulence, as Haller has demonstrated previously for laboratory flows [Mathur 2007].

The insight gained by the LCS analysis of flow in the idealized channel, and the identification of eddy structures, bode well for the use of FTLE-LCS for understanding the role of mesoscale eddies in global ocean data, which we turn to next.

7.2 Reanalysis data for the global ocean

For our study we have used reanalysis data for global ocean currents provided by the Mercator Ocean Modeling group [Drevillon 2008]. The Mercator data product is produced by running a global ocean model at high resolution while assimilating satellite observations of sea surface height data – the primary driver of mesoscale eddy activity. The model also incorporates data received from merchant ships, as well as data retrieved from thousands of drifters deployed throughout the global ocean that relay current data through satellite uplinks.[2]

Computation of the FTLE for the global ocean reveals a rich labyrinth of coherent mesoscale eddy structures. Figure 7.3 shows the LCS computed for the global ocean for an integration time of three weeks. Perhaps most striking is the inhomogeneity in the distribution of the LCS. The Antarctic Circumpolar Current, the Atlantic Gulf Stream, the Cape Cauldron at the Southern tip of Africa, and the equatorial jets in the Eastern Pacific are all highlighted as regions of robust activity. Images of all these regions are shown in higher resolution in Figures 7.4(a) through 7.4(c). Taken purely from a visual perspective, the FTLE computation conveys intricate details about coherent structures in the ocean. These images are to be contrasted with plots of velocity, vorticity (see Figure 7.5), and sea surface height that are the more traditional plots used by oceanographers. Certainly, these are all important quantities to study, but do not capture the Lagrangian information necessary to understand transport

[2]See the Argo project at http://www.argo.ucsd.edu/index.html

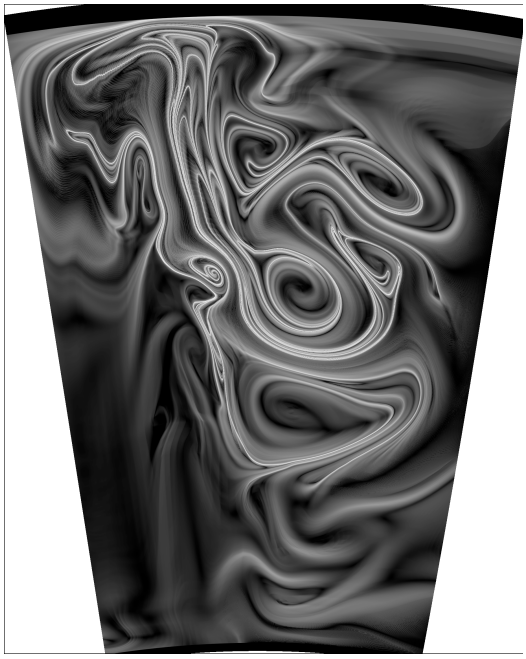

(a) Repelling FTLE.

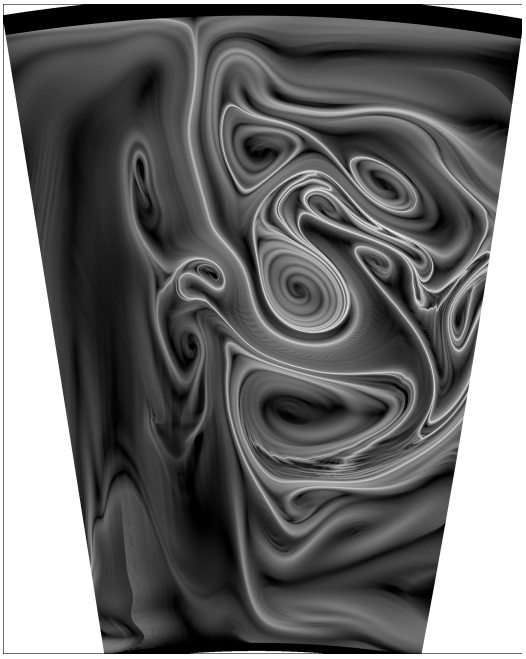

(b) Attracting FTLE.

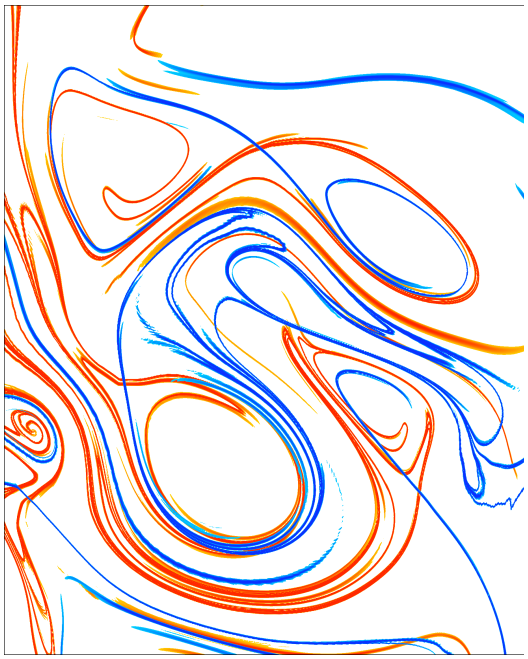

(c) Superimposing the repelling LCS (red) and the attracting LCS (blue) indicates the presence of familiar objects from low-dimensional dynamical systems, such as the Duffing oscillator.

Figure 7.2: LCS in flow of the idealized channel model of the Antarctic Circumpolar Current for the section of channel immediately behind the deep sea ridge.

mechanisms in mesoscale eddies. The LCS in the higher resolution images reveal the boundaries of the mesoscale eddies, and the time-dependence of the LCS reveals the manner in which eddies are created, interact with each other, and are finally destroyed, or subsumed by neighboring eddies.

Figure 7.4(c) shows a close-up of the Cape Cauldron off the Southern coast of Africa. The Agulhas retroflection is a well-known current formation that brings warm water from the equatorial ocean along the Eastern coast of Africa to the Southernmost tip of Africa, where the current undergoes a dramatic retroflection and joins the Eastward flow of the Antarctic Circumpolar Current. As a consequence, the Agulhas retroflection plays an important role in mixing warm surface water into the Antarctic Circumpolar Current. In the visualization provided by the FTLE computation, we see that the retroflection is not simply retrograde motion of bulk laminar flow, but rather the current is teeming with eddies that are vigorously inducing and enhancing mixing of tracers. Animations of the LCS reveal that the eddies interact strongly with each other while being advected in the direction of the mean flow.

An important feature revealed by the LCS, in relation to the role of mesoscale eddies is that the eddies are indeed the driving "atoms" of transport and mixing. If mixing in the ocean were diffusion-dominated, then we would not expect to see sharp LCS structures – the FTLE would be a diffuse field without strong ridges. To the contrary, strong LCS ridges are evident, and eddies retain their integrity and exchange material through complex networks of lobes. Zooming in on a single eddy in the FTLE field, as in Figure 7.6, reveals that the boundary of the eddy, even for this turbulent ocean flow, has the familiar shape of the perturbed homoclinic tangle observed previously in the pendulum and in hurricanes.

Taking time to view the images of the FTLE provides insight into the nature of turbulent structures in the ocean, and in particular the role that mesoscale eddies play in mediating mixing. The time-dependence of the LCS reveals the mechanisms by which folding, stretching, and transport occur. From a mathematical viewpoint, it is reward enough to see that the structures envisioned by Poincare in the three-body problem, and then reformulated abstractly by Smale, can be found

Figure 7.3: Repelling FTLE for the Global Ocean. The LCS reveal boundaries to mesoscale eddies that are responsible for lateral mixing. Regions of intense activity include the Pacific Equatorial jets, the Atlantic Gulf Stream, the Cape Cauldron, and the Antarctic Circumpolar Current.

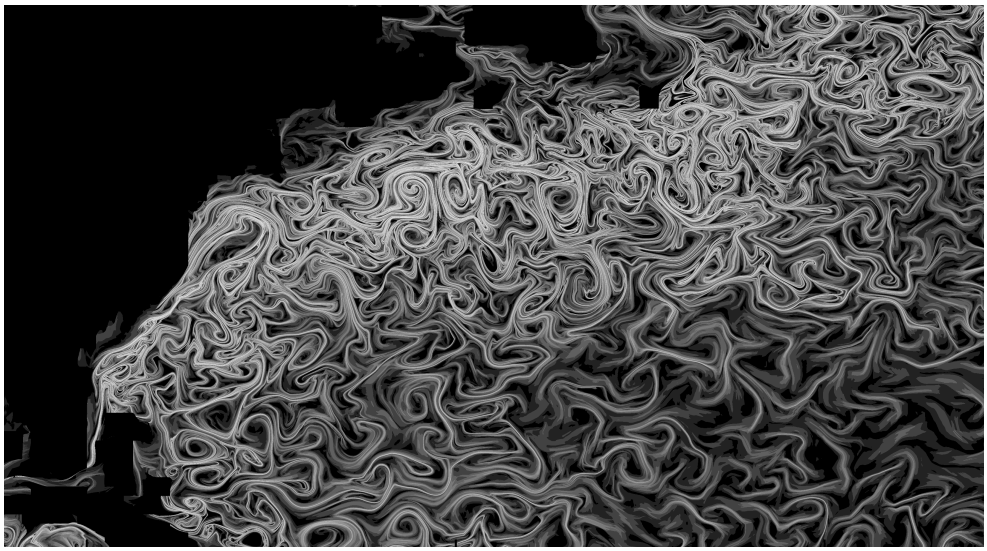

(a) The Atlantic Gulf Stream.

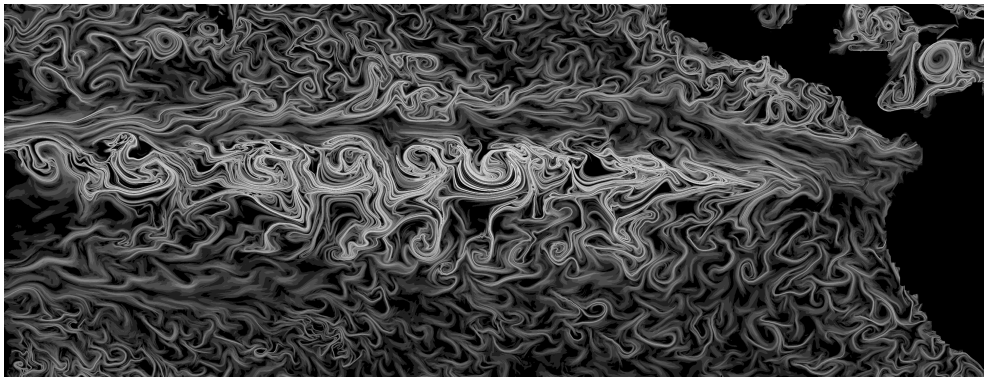

(b) The Pacific Equatorial Jets.

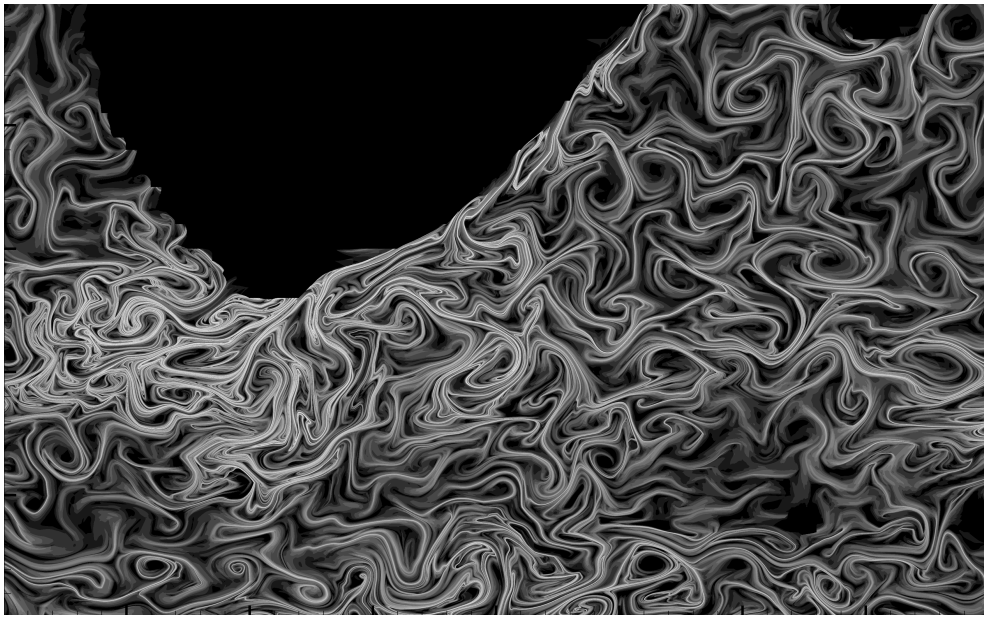

(c) The Cape Cauldron.

Figure 7.4: Mesoscale eddies visualized by the LCS reveal that the major ocean conveyor belts are teeming with eddies that constantly stir and mix the flow.

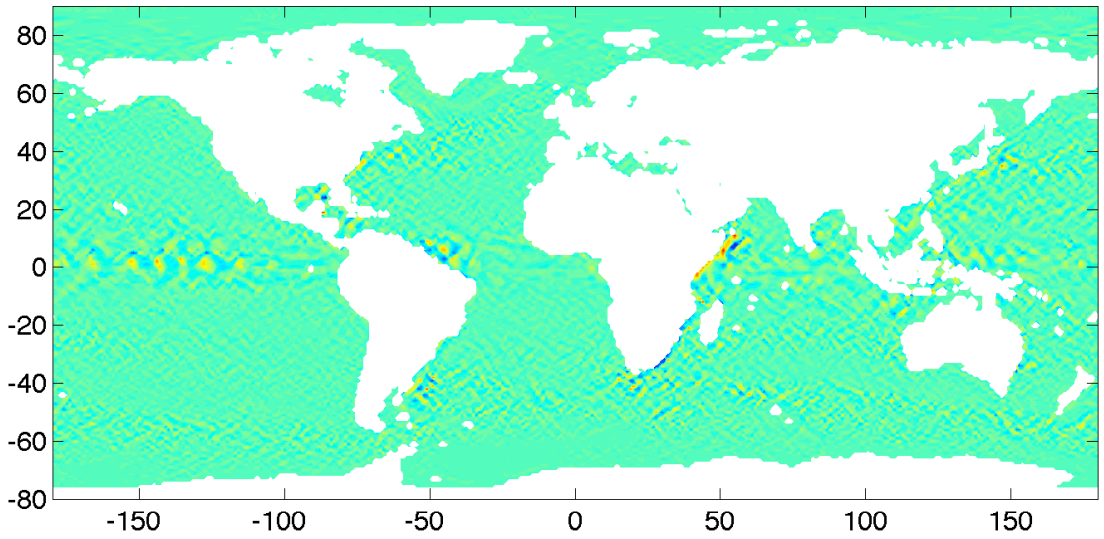

Figure 7.5: A plot of vorticity in the Global Ocean indicates the presence of eddies, but does not provide the same intricate detail as the LCS analysis. Moreover, the time-dependence of the vorticity does not indicate the mechanism responsible for transport and mixing between the eddies.

vigorously at work in the global ocean. To the oceanographer, these analyses will hopefully provide insight into the structure of turbulence, its spatial inhomogeneity, and the mechanisms by which mixing occurs, so that future parametrizations of these processes can be better informed. The realization of the importance of lobe dynamics suggests that the dynamical systems community may be able to shed helpful light on the the eddy parametrization problem. The studies of Rom-Kedar [Rom-Kedar 1990, Rom-Kedar 1991], for example, provide parametrized rates of mixing via lobe dynamics in a homoclinic tangle that may find useful application to the eddy parameterization problem in global ocean models.

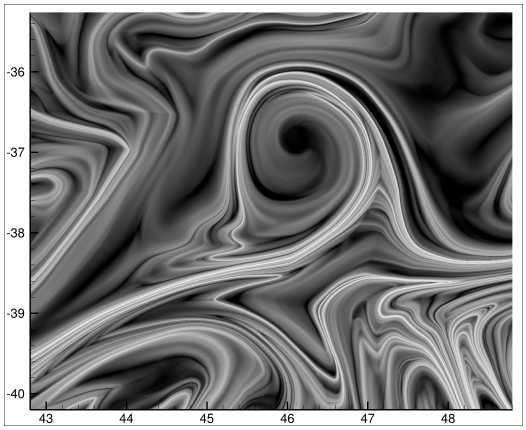

(a) Repelling FTLE.

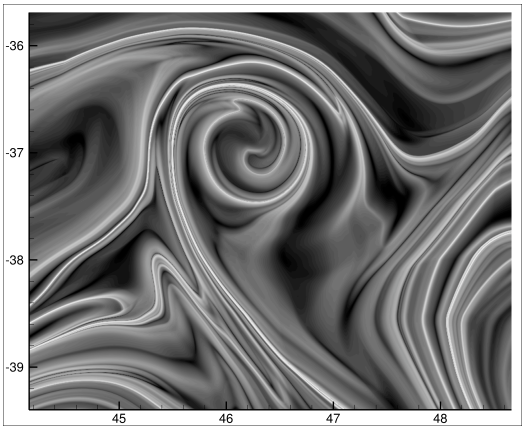

(b) Attracting FTLE.

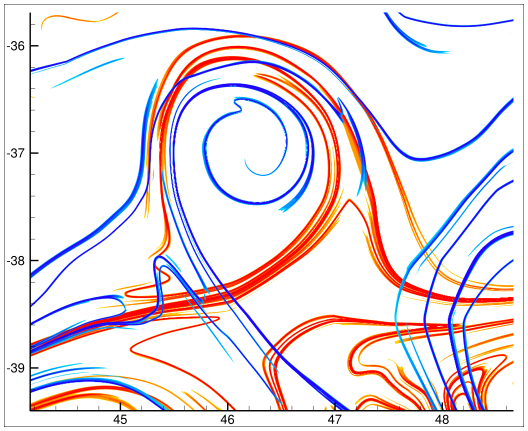

(c) The repelling LCS (red) and the attracting LCS (blue) are superimposed to reveal the boundary of a mesoscale eddy.

Figure 7.6: LCS in the Global Ocean reveals the boundary of a mesoscale eddy. The boundary has the familiar shape of the homoclinic tangle, as well as the boundary of hurricanes computed in Chapter 6. The time-dependence of the LCS reveals the mechanism for transport into and out of the eddy, and demonstrates that the eddy is the 'atom' of mixing.

Chapter 8

Flow of a Biomolecule

We leave our analysis of fluid flows for the moment, and consider the flow in a second order dynamical system. The system we study is a coupled oscillator system that models behavior of a linear biomolecule [Du Toit 2009a]. At the end of the analysis, we shall see that the LCS approach reveals the mechanism that governs transport in the flow, and that the underlying transport structure is the homoclinic tangle. Before arriving at this point, however, we will need first to provide a suitable reduction of the full system, which has hundreds of degrees of freedom, to a reduced single degree of freedom system that adequately captures the relevant transport dynamics.

Averaging over fast variables is a widely used method to obtain coarse equations of motion in mechanical systems with many degrees of freedom [Sanders 2007]. For example, averaging methods have been successfully used to find accurate coarse models in celestial mechanics and in oscillating electrical circuits [Verhulst 2000]. The system of nonlinearly perturbed coupled oscillators under study in this chapter, however, exhibits resonances on all scales and consequently does not admit analysis using standard averaging techniques. Furthermore, the full system, as will be demonstrated using a simple bio-mechanical example, has interesting dynamics that includes spontaneous and coherent changes in global conformation, and a reduction of the system using straightforward truncation methods fails to capture the crucial influence of the fine-scale dynamics that induces this conformation change.

The class of nonlinear systems of coupled oscillators that we study are close to a coupled chain of linear harmonic oscillators. Such near-integrable systems have been

studied in [Forest 1992] where transition to equipartition of energy, and dynamical properties related to integrable instability theory of partial differential equations were investigated [Ercolani 1990]. Here we discuss the representation of dynamics of the full oscillator system as a time-dependent single degree of freedom oscillator that represents well certain aspects of the full dynamics such as coherent switching between equilibria.

We begin by presenting an approximation to the full coupled oscillator system that allows for the derivation of a single coarse equation that retains essential contributions from the higher order components. Moreover, the resulting single degree of freedom system faithfully captures the statistics of the interesting conformation change behavior observed in the full system. The approximation involves, in essence, replacing higher order components in the perturbed problem with corresponding analytic trajectories for the nearby linear system.

For the biomolecular example system, we also investigate robust actuation of conformation change and demonstrate that low-powered traveling wave perturbations provide an efficient means for achieving near optimal conformation change. Finally, we will apply the LCS method to visualize transport structures in the dynamics describing the coarse variables and consequently gain insight into the transport mechanisms that allow for global conformation change to occur.

8.1 Coarse variables and models

Consider the following system of ordinary differential equations:

$$\ddot{\theta}(t) + D \cdot \theta(t) = \epsilon F(\theta(t), t) \tag{8.1}$$

with initial conditions

$$\theta(0) = a \qquad\qquad \dot{\theta}(0) = b\,,$$

where a, b, and $\theta(t)$ are vectors in $\mathbb{R}^N$, $F : \mathbb{R}^N \times \mathbb{R} \to \mathbb{R}^N$ is a nonlinear time-dependent mapping, $\epsilon > 0$ is a small parameter that controls the size of the nonlinear

perturbation, and $D : \mathbb{R}^N \to \mathbb{R}^N$ is a linear mapping that has the tri-diagonal matrix representation

$$D = \begin{bmatrix} 2 & -1 & 0 & & & 0 & -1 \\ -1 & 2 & -1 & 0 & & & 0 \\ 0 & -1 & 2 & -1 & 0 & & \\ & \ddots & \ddots & \ddots & \ddots & \ddots & \\ & & 0 & -1 & 2 & -1 & 0 \\ 0 & & & 0 & -1 & 2 & -1 \\ -1 & 0 & & & 0 & -1 & 2 \end{bmatrix} .$$

The smoothness conditions we require are that $F(\theta, t)$ is continuous in t and Lipschitz-continuous in θ. Equation (8.1) and the initial conditions can be written in component form using subscripts to denote the indices as

$$\ddot{\theta}_k = \theta_{k+1} - 2\theta_k + \theta_{k-1} + \epsilon F_k(\theta, t) \qquad k = 1, \ldots, N ,$$

$$\theta_k(0) = a_k \qquad \dot{\theta}_k(0) = b_k$$

where $\theta_0 = \theta_N$ defines the periodic boundary condition.

Such a system arises naturally from a spatial discretization of a nonlinearly perturbed wave equation with periodic boundary conditions:

$$u_{tt}(x, t) = u_{xx}(x, t) + \epsilon G(x, u(x, t), t) ,$$

where $u : \mathbb{R} \times \mathbb{R} \to \mathbb{R}$ is the amplitude of the wave in time and space (subscripts denote partial differentiation), and the real-valued function G represents the perturbation. In this context, the D matrix in equation (8.1) is simply a centered finite differencing operator that approximates the second partial derivative of u with respect to the spatial variable x, and F is obtained by evaluating G at uniformly discrete spatial positions x_k so that $F_k(\theta, t) := G(x_k, \theta, t)$, $\theta_k(t) := u(x_k, t)$, and $x_0 = x_N$.

Equivalently, equation (8.1) can be viewed as the dynamical system describing a

linear chain of N oscillators in which each oscillator is subject to a weak nonlinear potential and coupled to nearest neighbors through a harmonic potential; a specific example of such an oscillator chain related to the mechanics of biomolecules will be provided later. E. Fermi, J. Pasta, S. Ulam, and M. Tsingou used a similar chain of coupled oscillators as an example system in their pioneering numerical study of nonlinear dynamics that has since become famously known as the Fermi-Pasta-Ulam-Tsingou[1] (FPUT) problem [Fermi 1955]. The initial purpose of their study was to develop a theory of thermalization in systems with nonlinear dynamics; however, their investigation yielded unexpected results – energy initially placed in one mode did not become equally partitioned among all the modes after some time. Rather, they observed recurrences (as predicted by Poincaré) where the energy initially redistributed among some of the modes but then returned to the initial condition in which all the energy is again found in a single mode. Analyses of the FPUT problem fill a large body of literature including, for instance, the discovery of soliton and chaotic breather solutions, and have yielded insight into the interplay between chaos and integrability in nonlinear systems (see reference [Campbell 2005] for a survey of results related to the FPUT problem on the fiftieth anniversary of the introduction of the problem). The approach to the problem addressed in this chapter differs from traditional FPUT problem analyses in that, motivated by the biomolecular applications to DNA, we are interested in issues such as reduction to coarse variables and activation of global large-scale conformation change through the application of small local controls that are not typically associated with the FPUT problem.

We study the system of ordinary differential equations described by equation (8.1) when N is large, and hence the system has many degrees of freedom. Rather than determine precisely the dynamics of each degree of freedom, we are interested in describing the dynamics of only a single coarse variable. The first question to be addressed here is the following: how do we extract from the large N degree of freedom

[1]Historically, this problem has been referred to as the Fermi-Pasta-Ulam (FPU) problem; however, recently the contribution of Mary Tsingou to the implementation of the numerical routines has been more widely appreciated thus motivating the addition of her name. The recent article in [Dauxois 2008] provides a discussion of the relevant history.

system an evolution equation for a single coarse variable that describes a property of interest? For the purposes of the current study, our goal is to determine a single evolution equation for the dynamics of the *average* amplitude while faithfully retaining salient dynamical features of the full system. As will be shown later, the dynamics of the coarse variable will need to include the influence of the fine scales in order to reproduce the coarse evolution correctly. We begin by first gaining insight from the unperturbed case.

8.1.1 The unperturbed case

For $\epsilon = 0$, the system in equation (8.1) becomes:

$$\ddot{\theta}(t) + D \cdot \theta(t) = 0\,, \tag{8.2}$$

with initial conditions

$$\theta(0) = a \qquad\qquad \dot{\theta}(0) = b\,.$$

This is a simple linear system whose solution is easily obtained analytically. The solution is provided here in detail as it includes many building blocks required for the less tractable case when the nonlinear perturbation is included.

We begin by introducing a change of coordinates that diagonalizes the coupling matrix D. Let P be an $N \times N$ matrix whose columns contain the complete set of orthonormal eigenvectors of the real symmetric matrix D:

$$P_{kw} := \sqrt{\tfrac{2}{N}} \left[\begin{array}{cccccc} \frac{1}{\sqrt{2}} & \cos\frac{2\pi kw}{N} & \frac{(-1)^k}{\sqrt{2}} & \sin\frac{2\pi kw}{N} & & k=[1\ldots N] \\ & & & & & \\ w{=}0 & w{=}\left[1\ldots\frac{N}{2}{-}1\right] & w{=}\frac{N}{2} & w{=}\left[\frac{N}{2}{+}1\ldots N{-}1\right] & & \end{array} \right].$$

(Here we have taken N to be even for simplicity, although the case for odd N merely has the middle column corresponding to $w = \frac{N}{2}$ removed and the column numbering

altered accordingly.)

Next, we define new coordinates by the linear transformation,

$$\hat{\theta} := P'\theta \tag{8.3}$$

where P' denotes the transpose of P. Notice that

$$\hat{\theta}_0 := \frac{1}{\sqrt{N}} \sum_{k=1}^{N} \theta_k \tag{8.4}$$

is (except for a constant factor of $\sqrt{N}$) the average amplitude. In these coordinates, the symmetric linear operator D is diagonal, yielding N uncoupled second order ODEs. In component form, they are written as

$$\ddot{\hat{\theta}}_0 = 0 \tag{8.5a}$$

$$\ddot{\hat{\theta}}_w + \alpha_w^2 \hat{\theta}_w = 0 \qquad w = 1, \ldots, N-1\,, \tag{8.5b}$$

where $\alpha_w^2 := 2\left(1 - \cos\frac{2\pi w}{N}\right)$, and the initial conditions become

$$\hat{\theta}(0) = P'a =: \hat{a} \qquad\qquad \dot{\hat{\theta}}(0) = P'b =: \hat{b}\,.$$

Here we can immediately conclude that the evolution of the average amplitude in the unperturbed case is given by the single scalar equation

$$\hat{\theta}_0(t) = \hat{a}_0 + \hat{b}_0\, t\,.$$

Straightforward solution of the higher order components yields the analytic evolution equations

$$\hat{\theta}_w(t) = \hat{a}_w \cos\alpha_w t + \frac{\hat{b}_w}{\alpha_w} \sin\alpha_w t \qquad w = 1, \ldots, N-1\,. \tag{8.6}$$

We readily observe that the system has N integrals of motion, $\{I_w\}_{w=0}^{N-1}$, defined by

$$\dot{\hat{\theta}}_0(t) = (\hat{b}_0) =: \sqrt{2I_0}$$
$$\hat{\theta}_w(t)^2 + \left(\frac{\dot{\hat{\theta}}_w(t)}{\alpha_w}\right)^2 = (\hat{a}_w)^2 + \left(\frac{\hat{b}_w}{\alpha_w}\right)^2 =: 2I_w \quad w = 1, \ldots, N-1\,.$$

The first integral is simply a statement of the conservation of total (or average) momentum. The higher order modes evolve on circles of constant radii $\sqrt{2I_w}$ with an angular frequency of α_w. With these insights, we may write the system in completely integrable Hamiltonian form using action angle coordinates (I, ϕ), where I and ϕ are both vectors of length N whose components I_w and ϕ_w are denoted with subscripts:

$$H^0(I_0, \ldots, I_{N-1}) = \sum_{w=1}^{N-1} \alpha_w I_w \tag{8.7}$$

so that the Hamiltonian vector field becomes

$$\dot{I}_w = -\frac{\partial H^0}{\partial \phi_w}(I_0, \ldots, I_{N-1}) = 0$$
$$\dot{\phi}_w = \frac{\partial H^0}{\partial I_w}(I_0, \ldots, I_{N-1}) = \alpha_w \qquad w = 0, \ldots, N-1\,.$$

Before proceeding to an analysis of the perturbed case, we first observe here some of the important properties of the unperturbed system.

Remark. *The Hamiltonian H^0 is degenerate.*

The Hamiltonian H^0 is linear in the components of I; hence

$$\det\left(\frac{\partial^2 H^0}{\partial I_i \partial I_j}(I_0, \ldots, I_{N-1})\right) = 0 \qquad i, j = 0, \ldots, N-1\,, \tag{8.8}$$

and the frequency map $I \to \alpha(I)$ is not a diffeomorphism. This degeneracy of the Hamiltonian implies that the system does not satisfy the assumptions of classical KAM theorems and hence straightforward KAM theory cannot be applied [Wiggins 2003].

Remark. *The frequency vector α is resonant.*

Since the first element of the frequency vector α is 0, any $\kappa \in \mathbb{Z}^N \setminus \{0\}$ of the form

$\kappa = [z\ 0\ \ldots\ 0]'$ for any $z \in \mathbb{Z} \setminus \{0\}$ yields $\kappa \cdot \alpha = 0$. The irrational structure of the eigenvalues in the higher modes leads to the conclusion that the resonant frequency vector α is of multiplicity 1.

Furthermore, since z is any element in $\mathbb{Z} \setminus \{0\}$, we can conclude the following:

Remark. *The frequency vector α has resonances at all orders.*

A standard approach to achieve reduction of order in a dynamical system is to perform averaging over the fast angular coordinates. However, for the system of interest, the resonances, or more specifically the zero eigenvalue corresponding to $\alpha_0 = 0$ in the equation for the average amplitude, precludes such a treatment. Standard statements of averaging theorems require all the components of the frequency vector α to be strictly greater than 0 (see the statement of the Averaging Theorem in [Arnold 1978], for example, or the discussion in Chapter 8 of [Sanders 2007] regarding passage through resonance and the absence of theory to treat the fully resonant case). Hence, the oscillator system represents a special case to which routine averaging methods cannot be applied.

Moreover, in our attempt to obtain a single closed equation for the evolution of the average variable, straightforward averaging or truncation approaches are ineffective for an even more subtle—yet crucial—reason. Averaging over the higher order components (laying the resonance issues aside) yields a single degree of freedom, and hence an integrable system. As such, the reduced equation fails to capture important details in the dynamics arising from the inherent non-integrability, and in particular the intricate influence of the higher order components on the average mode. A thorough review of averaging methods is not within the scope or purpose of this thesis. However, an important point to be made is that a central feature of the proposed method for reduction is that it incorporates in an approximate yet effective way the influence of the higher order modes, and consequently more accurately captures non-trivial dynamics associated with the full non-integrable system.

8.1.2 Perturbed case

We use the same definitions and process used in the unperturbed case for the perturbed case. We begin by making the same linear change of coordinates using the matrix of eigenvectors P so that the transformed equations of motion become:

$$\ddot{\hat{\theta}}_0 = \epsilon\, P_{k0} F_k(P\hat{\theta}) \tag{8.9a}$$

$$\ddot{\hat{\theta}}_w + \alpha_w^2 \hat{\theta}_w = \epsilon\, P_{kw} F_k(P\hat{\theta})\,, \qquad w = 1, \ldots, N-1, \tag{8.9b}$$

where we sum over k from 1 to N on the right hand side.

As expected, the coordinate transformation diagonalizes the nearest neighbor coupling term, but the nonlinear forcing term remains globally coupled. At this stage, no approximations have been made and equations (8.9a) and (8.9b) recover the full solution exactly. For nonzero ϵ, the system is no longer integrable and the solutions that were previously observed to evolve on circles of fixed radii are perturbed.

At this point, we must consider how to break the coupling between the zeroth order equation for the average amplitude and the higher order modes in order to obtain a closed equation for the average amplitude. As previously mentioned, the system is not amenable to averaging methods because of the zero eigenvalue in the frequency vector. Rather, we introduce an approximation by replacing equations (8.9b) with the analytical solutions of the unperturbed linear system as defined in equation (8.6). This approach effectively removes the need to integrate the higher order modes by replacing their evolution with the explicit analytic solution of the nearby integrable system. In so doing, we obtain the improved approximation, $\bar{\theta}_0$, of the exact solution $\hat{\theta}_0$, whose dynamics is prescribed by

$$\ddot{\bar{\theta}}_0 = \frac{\epsilon}{\sqrt{N}} \sum_{k=1}^{N} F_k(P\bar{\theta})\,, \tag{8.10}$$

where in the right hand side P is a constant matrix, and $\bar{\theta}$ is a vector whose first component is the scalar dependent variable $\bar{\theta}_0$ and whose remaining components are

elementary functions of time and the initial conditions of the full system provided analytically by equation (8.6).

Remark. *The solution trajectories of equation* (8.10) *are within* $\mathcal{O}(\epsilon)$ *of the solution trajectories of the original full system described in equation* (8.9a) *for times* $\mathcal{O}(1)$.

This result is shown by applying a standard error analysis technique: substituting a formal expansion of the solution, using the Lipschitz continuity of F, and then applying the Gronwall lemma as is done in the proof of Theorem 9.1 in [Verhulst 2000], for example.

The approach proposed here for obtaining a closed equation for the average amplitude includes the influence of higher order modes by incorporating explicit time-dependence in the perturbing term, and hence leads to a one and a half degree of freedom system. The coordinate transformation and subsequent approximation yield a single *non-autonomous* ordinary differential equation that includes approximate dynamics for the higher order scales, and whose solution approximates the dynamics of the average angle of the system. In effect, the information contained in the higher order modes persists in the lower order description via the initial conditions.

The method just described is now applied to a simple coupled-oscillator model for biomolecules where retention of the influence of the higher modes in the dynamics is essential for accurately recovering nontrivial dynamics of conformation change.

8.2 Conformation change in biomolecules

Biomolecules undergo rapid and global conformation change as a crucial part of their function. Many statistical mechanical models have been proposed in which these conformation changes are the result of increased thermal fluctuations [Yakushevich 2004, Peyrard 2004, Weber 2006, Dauxois 1993, Causo 2000, Kafri 2002], or an external agent that provides an overwhelming force [Bhattacharjee 2000, Cocco 1999]. Presently, we are interested in investigating whether this conformation change phenomenon can be induced simply by utilizing the natural dynamics inherent to the system. A simple

model will be presented in which the intrinsic design of the dynamics ensures the robustness of conformational states to random perturbations, yet global conformation change can be robustly induced by the action of a low-energy local control. At the heart of this dynamical behavior is the exchange of energy between smaller and larger scales. The approximation technique presented in the first section allows passage to a low-dimensional model that effectively captures this behavior.

8.2.1 The model

We consider a class of biopolymers that can be modeled as a long circular chain of identical pendula attached to a rigid backbone. Each pendulum has one rotational degree of freedom in the plane orthogonal to the backbone. The motion of the pendula is governed by two interactions: each pendulum interacts with its nearest neighbors through a harmonic potential that models torsional coupling through the backbone; and secondly, each pendulum moves in a Morse potential that models the weaker hydrogen bonding interaction between pendulum pairs on a complementary chain. We immobilize one of the strands and consider only the motion of the pendula on the opposing strand as depicted in Figure 8.1.

Using the pendulum mass, m, for the mass scale; the pendulum length, h, for the length scale; and the nearest neighbor coupling strength, S, for the energy scale; the non-dimensional Lagrangian that describes the motion of N coupled pendula is given by

$$L(\theta,\dot{\theta}) = \sum_{k=1}^{N} \left[\frac{1}{2}\dot{\theta}_k^2 - \frac{1}{2}(\theta_k - \theta_{k-1})^2 - \epsilon \left(e^{-a[1-\cos\theta_k - x_0]} - 1 \right)^2 \right],$$

where a, x_0, and ϵ are the Morse potential decay coefficient, the Morse potential equilibrium distance, and the Morse potential amplitude respectively. The angular displacement of the k^{th} pendulum is denoted θ_k. The argument of the Morse potential is the distance between complementary base pairs projected onto the vertical. The time, t, has been scaled by the induced non-dimensional time, $\tau = \sqrt{S/(mh^2)}\, t$.

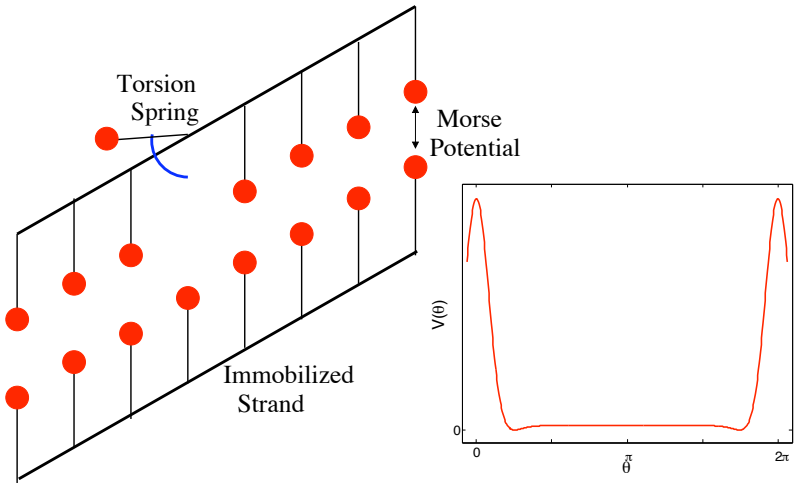

Figure 8.1: The biomolecule is modelled as a chain of pendula that rotate about the axis of a fixed backbone. The pendula interact with nearest neighbors along the backbone through harmonic torsional coupling, and with pendula on the opposing strand through a Morse potential.

Lagrange's equations of motion yield

$$\ddot{\theta}_k - \theta_{k+1} + 2\theta_k - \theta_{k-1} = 2\epsilon a \left(e^{-a[1-\cos\theta_k - x_0]} - 1\right) e^{-a[1-\cos\theta_k - x_0]} \sin\theta_k$$

for $k = 1, \ldots, N$. These equations can also be written in the form introduced in equation (8.1): $\ddot{\theta} + D \cdot \theta = \epsilon F(\theta)$ where D is the constant tridiagonal $N \times N$ matrix that describes the nearest neighbor coupling, and F is the nonlinear vector-valued forcing term due to the Morse potential.

Numerical integration of the full system of equations was performed for a chain of $N = 200$ pendula using a fourth order symplectic integrator with excellent energy preservation properties [McLachlan 1992]. The parameter values were chosen to best represent typical values for biomolecules. The nondimensional scales are determined using parameter values $m = 300$ AMU, $h = 1$ nm, and $S = 42$ eV, that collectively induce a model time unit of 0.272 ps. In nondimensional units, the Morse potential parameters are $a = 7$, $x_0 = 0.3$, and $\epsilon = 1/1400$. For these parameter values, the nonlinear Morse potential term represents a small perturbation to the linear nearest

neighbor coupling interaction.

8.2.2 Properties of the model

The shape of the Morse potential induces two stable equilibria corresponding to global energy minima achieved when all the pendula have identical angular displacements (thus nullifying the nearest neighbor coupling) and are positioned at the Morse potential equilibrium distance, x_0, from their complementary pendula. For small energies, typical motions involve uncoordinated oscillations of the pendula near these stable equilibria, although Mezić has previously observed that a local perturbation can cause the pendula to undergo a coherent global change of conformation from one energy basin to the other [Mezic 2006]. By definition, we say that a global conformation change has occurred when the average angle of the pendula passes through π radians. This motion is referred to in the rest of this chapter as "flipping". A convenient way to represent this flipping behavior is to project the trajectory of the system onto the average variables $\Theta := \frac{1}{N}\sum_{k=1}^{N}\theta_k$ and $\dot{\Theta}$ as shown in Figure 8.2(b). In this projection we see that the pendula at first oscillate about an energy minimum in one conformational state, and then undergo conformational change to the other energy basin where they continue to oscillate.

8.2.3 The reduced order model

As noted above, the average angle variables, Θ and $\dot{\Theta}$, provide a good coarse description of the flipping process and begs the derivation of a single closed equation for the average variable. There is, however, no separation of time scales in this system so that simple truncation to a low order model does not retain sufficient dynamics to incorporate spontaneous flipping events. Indeed, any method that yields an autonomous single degree of freedom system for the coarse variable cannot possibly capture the flipping event. Furthermore, as previously noted, routine averaging methods are not applicable since intrinsic resonances induce coupling on all scales.

The approach presented in the first section is now applied to this pendulum chain

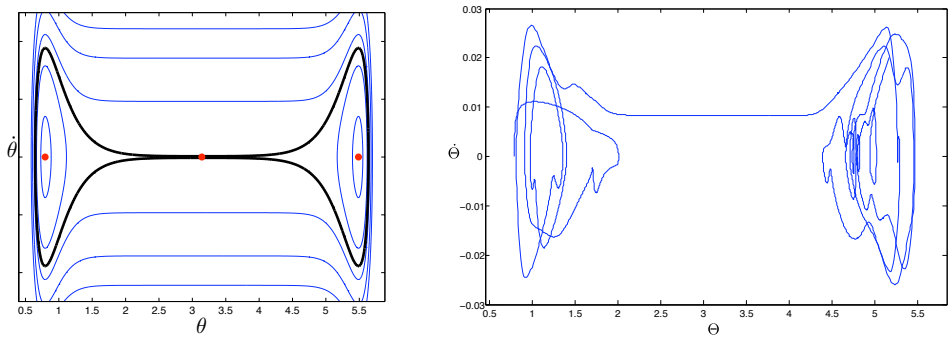

(a) (b)

Figure 8.2: Figure (a) shows sample phase space trajectories of a single pendulum in the Morse potential when no coupling is present. The homoclinic trajectory is emphasized. The locations of the equilibrium points are marked with red dots. Trajectories inside the homoclinic trajectory associated with the equilibrium point at $(\pi, 0)$ are always oscillating, while those outside the homoclinic trajectory are always flipping. Figure (b) shows a single trajectory of the fully-coupled model projected onto the average variable phase space and indicates a flipping event from one conformational state to the other. The trajectory resembles the phase portrait for a single pendulum moving in the Morse potential; however, the harmonic nearest neighbor coupling provides resonant kicks that allow the trajectory to escape from one energy basin and then become trapped by the other.

to obtain a low order model that retains the essential influence of the higher order scales on the global flipping behavior. With no Morse potential ($\epsilon = 0$), the remaining linear system has an explicit solution in which the average velocity $\dot{\hat{\theta}}_0$ is constant, and the remaining coordinate pairs $(\hat{\theta}_w, \dot{\hat{\theta}}_w)$ (after scaling $\dot{\hat{\theta}}_w$ by its corresponding frequency, α_w) evolve on circles of fixed radii. For small nonzero ϵ, this integrable solution is perturbed as shown in Figure 8.3. Certainly, deviations from the linear solution are evident in the lower modes, whereas the trajectories of the higher order components remain close to the integrable circular solutions of the unperturbed case. Numerical experiments reveal that as epsilon is increased, the higher order components in a typical flipping trajectory remain close to the unperturbed solution until epsilon has increased by a factor of 10. As epsilon increases further, the higher order components still exhibit oscillatory behavior, but the stronger nonlinear coupling causes large deviations from the trajectories along fixed radii and the circular

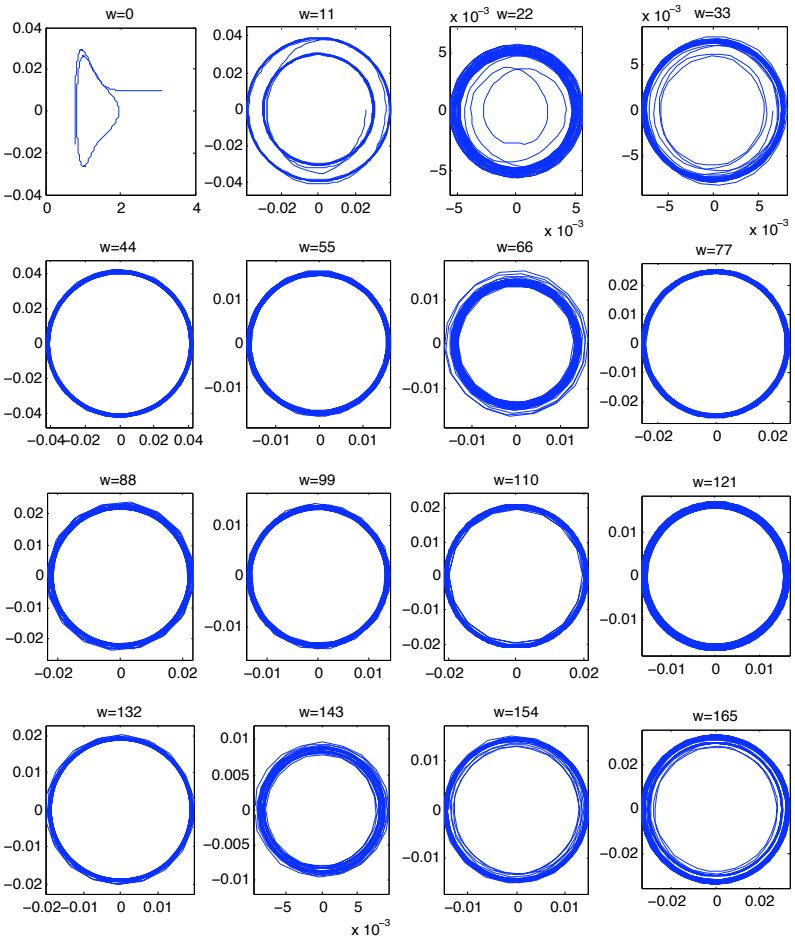

Figure 8.3: The evolution of a few of the $\hat{\theta}_w$ and $\dot{\hat{\theta}}_w$ variables is shown here. The average mode ($w = 0$) indicates that flipping occurs as in Figure 8.2(b) while the remaining modes simply oscillate with small deviations from the unperturbed ($\epsilon = 0$) integrable solution.

solutions disintegrate.

The $1\frac{1}{2}$ degree of freedom reduced system obtained using the approximation in equation (8.10) retains sufficient dynamics of the higher order modes in the time-dependent terms to capture statistics of the the flipping event remarkably well. The distributions of numerically computed flipping times for 5000 random initial conditions for the $1\frac{1}{2}$ degree of freedom reduced system and the full 200 degree of freedom system are compared in Figure 8.4. The histograms in Figures 8.4(a), 8.4(b), and 8.4(c) are computed using values of epsilon equal to 1/1400, 5/1400, and 10/1400

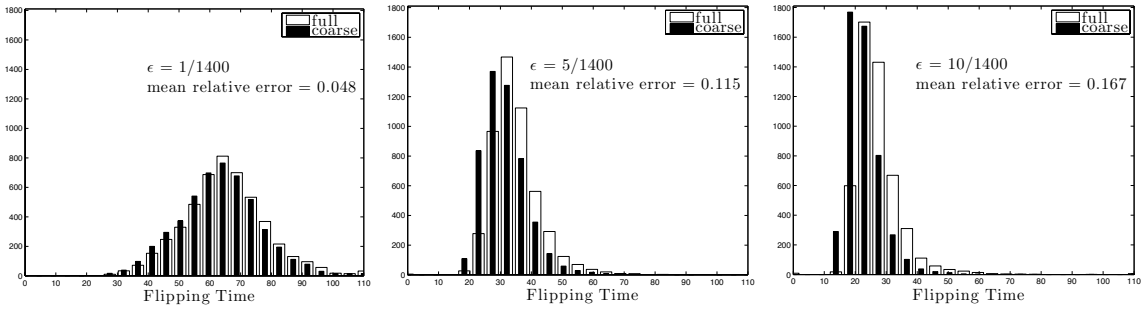

(a) (b) (c)

Figure 8.4: The histograms provided here compare the distribution of flipping times predicted by the $1\frac{1}{2}$ degree of freedom reduced model (shown in solid) with the distribution of flipping times predicted by the full 200 degree of freedom system (shown in outline) for different values of epsilon. The histograms are computed using 5000 random initial conditions. The plot in (a) was computed using a value of epsilon equal to 1/1400 consistent with the biomolecule model, while (b) and (c) were computed using values of epsilon that are larger by a factor of 5 and 10 respectively. In (a) we see that the reduced model captures the distribution of flipping times remarkably well with a relative error of 4.8 percent. As expected, the relative error increases for larger values of epsilon.

respectively. When epsilon is equal to 1/1400 (the value provided by the biomolecule model), the reduced model captures the shape of the flipping time distribution remarkably well and the mean relative error in the predicted flipping time is less than five percent. As expected, the relative error in the flipping time prediction increases as epsilon is increased. The quasi-periodic forcing introduced in the right hand side of equation (8.10) by the solution for the linear system provides the perturbation required to induce global flipping from a local perturbation and can be thought of as a time-dependent control.

The rigorous error estimate obtained in Section 8.1.2 stated that trajectories of the reduced model are within $\mathcal{O}(\epsilon)$ of the true solution for times $\mathcal{O}(1)$. The application of this error estimate to the biomolecule model merits the following two observations. First, the portion of a trajectory during which the pendulum experiences the Morse potential (which is responsible for inducing flipping motion) is very brief; the interaction occurs on a time-scale that is $\mathcal{O}(1)$ rather than the much longer $\mathcal{O}(1/\epsilon)$ time-scale, so that the estimate has validity, as evidenced numerically, for the

prediction of flipping times. Second, the error estimate was obtained for an arbitrary forcing function $F(\theta(t), t)$. In the biomolecule model, the exponential decay of the Morse potential with distance implies that when the pendula escape the immediate vicinity of the opposing pendula, the Morse potential and the consequent perturbation are effectively zero and the linear solution becomes nearly exact. Hence, the error estimate is conservative in that it utilizes only the fact that epsilon is small, and not the fact peculiar to the biomolecule model that in a large region of phase space the forcing term is also small. For these reasons, the numerically observed time-scale over which the reduced model for the biomolecule chain remains accurate is greatly increased over the rigorous estimate.

8.2.4 Efficient actuation of conformation change

The foregoing analysis indicates that the process of conformation change can be well-modelled by a low-dimensional model with a single degree of freedom. Next, we investigate the possibility of inducing this interesting flipping behavior using a low-powered local control.

Consider a pendulum chain in the stable equilibrium position. The minimum possible energy of a perturbation that induces flipping can be computed analytically and is

$$E_{\min} = N\epsilon \left(e^{-a[2-x_0]} - 1\right)^2 \approx 0.143$$

and corresponds to each pendulum being kicked with the same initial velocity. With this lower energy limit for reference, we have investigated the robustness of the zipped state by numerically measuring the flipping time as a function of energy for random and structured perturbations. The results shown in Figure 8.5 indicate that the tendency for flipping is strongly influenced by the structure of the initial perturbation and confirm the results found in [Mezic 2006].

Higher mode numbers refer to sinusoidal perturbations of higher harmonic frequencies. We also include the energy required to induce flipping with random perturbations (labeled "noise"), as well as perturbations consisting of the displacement

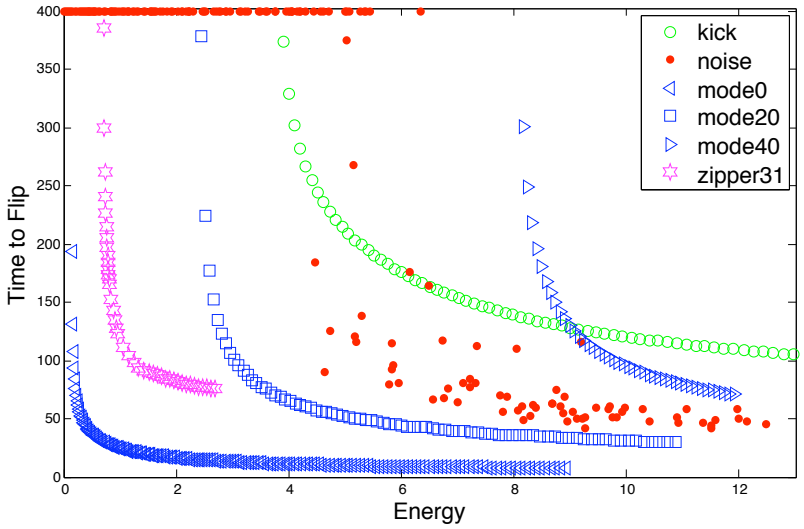

Figure 8.5: The time required for the chain to flip is plotted here as a function of the energy for various types of initial conditions. Green circles indicate initial conditions in which a single pendulum is displaced from the equilibrium position. Red dots indicate random initial conditions with gaussian distribution about the equilibrium. If flipping was not observed for this perturbation, a marker was placed at the 400 time mark at the top of the figure. The blue series in triangles and squares correspond to initial perturbations consisting of sinusoidal displacements with frequency indicated by the mode number. Magenta stars represent efficient "zippers" imparting 31 small kicks of varying strength as explained in the text. The amount of energy required to robustly induce flipping depends strongly on the frequency content of the initial condition. Less energy is required when the energy is placed in the low order modes. Random initial conditions must have energies above 6.0 to induce flipping whereas zippers require much less energy (0.75) to robustly induce flipping.

of a single pendulum (labeled "kick"). First, we notice that the equilibrium state is robust to very energetic random perturbations; energies in excess of 6.0 are required to robustly induce flipping. Second, flipping can be robustly induced by low-energy structured perturbations that comprise low frequency modes.

The magenta stars in Figure 8.5 refer to the following structured perturbation. Inspired by the unzipping action of polymerase and helicase proteins in DNA, we simulate the action of a hammer that moves along the strand with constant velocity and imparts a small kick to each pendulum as it passes. Despite its very low power requirement and localized interaction, this structured perturbation efficiently and

robustly induces global flipping motion by exciting the zeroth order collective mode. The action of the zipper comprises 31 small kicks (energy = 0.0245) providing a total energy of 0.75 to the pendulum chain. In contrast, the strand remains closed for random kicks that are two orders of magnitude larger than the individual kicks provided by the hammer. Hence, the pendulum chain has the interesting property that the conformation is robust against noise, yet allows for robust actuation of global conformation change through a small structured local control.

The fastest phonons in the pendulum dynamics move along the strand at a rate that is very near 1.0 pendulum per time unit. By increasing the speed with which the zipper moves down the chain well beyond this phonon speed, the total energy required to induce flipping can be made arbitrarily close to the theoretical minimum limit of 0.14. This observation follows from the fact that as the zipper moves faster, the time between kicks to subsequent pendula decreases and hence the perturbation approximates ever more closely the optimal perturbation of kicking each pendulum at the same instant. Thus, extremely (unrealistically) fast zippers can in effect provide the optimal global perturbation. On the other hand, by exploiting resonances in the dynamics, even slow-moving (more realistic) zippers are able to induce flipping with very low power consumption and only local interaction. The zippers referred to in Figure 8.5 move at a rate of only 0.4 pendula per time unit, well below the natural phonon velocity.

The zipper not only induces flipping more efficiently than the other perturbations considered, but also does so robustly when noise is added to the system. Figure 8.6 shows the energy required to induce rapid flipping (flipping occurs in less than 400 time units) when the system is simulated at constant temperature using a Brünger-Brooks-Karplus Langevin integrator with damping coefficient of 5 ns^{-1} [Brunger 1984]. For temperatures above 380K, flipping occurs before 10,000 time units without the action of any external perturbation. Notably, the zipper perturbation is able to robustly induce very fast flipping over a wide range of temperatures. Moreover, if the chain is at a low temperature and rigidly locked in a stable conformational state, conformational change can nevertheless be quickly induced.

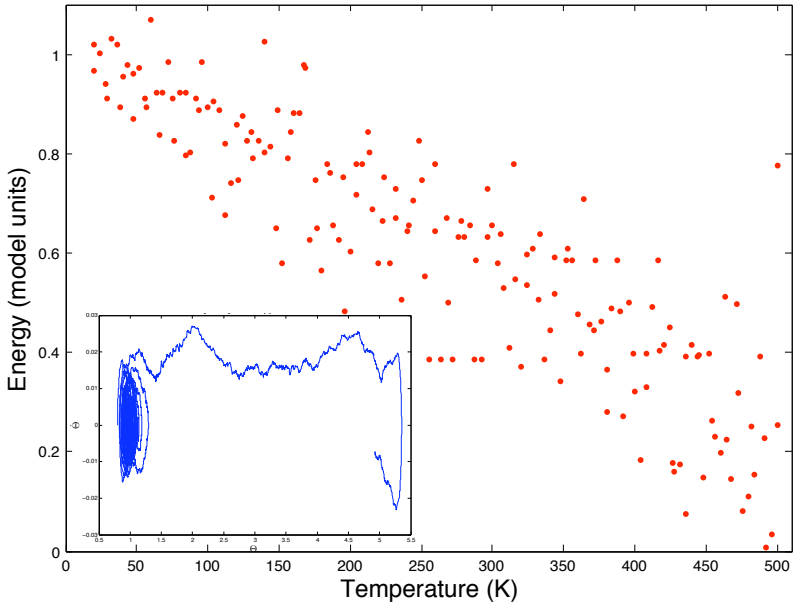

Figure 8.6: When the system is simulated at constant temperature, the zipper robustly and efficiently induces flipping. The energy required to induce flipping in less than 400 time units is shown for 120 simulations over a range of temperatures. The inset shows a sample trajectory induced by the zipper when the temperature is 310K and the zipper is activated after 2000 time units.

These observations in the simple chain of oscillators model yield insight into how biomolecule conformations can be robust to energetic stochastic perturbations (so that DNA, for example, does not spontaneously divide over a wide temperature range) and yet, with the right "trigger", it can divide reliably and quickly with a low energy wave-like perturbation. We believe that this is a fundamental dynamical mechanism that biological systems use to utilize natural dynamics in order to robustly perform rapid and reliable conformation changes that are not accidentally caused by random perturbations, and do not require the application of overwhelming force.

8.3 Visualizing transport in the reduced model

A single pendulum oscillating freely in the Morse potential is a one degree of freedom system whose phase portrait is shown in Figure 8.2(a). The shapes of the trajectories

in the full coupled-pendulum system, when projected onto the average variables as shown in Figure 8.2(b), resemble the trajectories of the single pendulum system except for the important difference that the single pendulum is an integrable system in which no *spontaneous* coherent flipping event can occur; the pendulum trajectory is either inside the homoclinic trajectory and never flips, or is outside the homoclinic trajectory and flips repeatedly. Therefore, the homoclinic trajectory in the single pendulum case defines a boundary of the conformation basin, and we say that a *spontaneous* flipping event in the full pendulum chain occurs when a trajectory in the average projection starts inside the region defined by the homoclinic trajectory, escapes it, and crosses into the other half plane by passing through the angle π radians.

These definitions afford us a precise manner in which to visualize transport from one conformation basin to the other. In the spirit of the FTLE-LCS method, the visualization method uses a measure of separation of nearby trajectories to find the boundaries of the regions in the flow that will undergo conformation change. Very simply, the visualization process involves four steps:

1. Construct a uniform grid of initial conditions in the phase space of the average angle in the reduced model.

2. Record whether each initial condition lies inside or outside a conformation basin as delineated by the homoclinic trajectory for the single pendulum.

3. (a) Advect each initial condition *forward* from time t_0 to time t_0+T and record whether the integrated position lies inside or outside a conformation basin.

   (b) Mark with blue each initial condition in the grid that has a neighboring initial condition that started in the same region but ended in a different region, and hence has separated from its neighbor (thus indicating points of forward separation).

4. (a) Advect each initial condition *backward* from time t_0 to time $t_0 - T$ and record whether the integrated position lies inside or outside a conformation basin.

(b) Mark with red each initial condition in the grid that has a neighbor position that started in the same region but ended in a different region after backward integration (thus indicating points of backward separation).

These four steps can be repeated for different initial times t_0 producing an animation of the time-dependent manifolds of separation. This method is of course motivated by the FTLE-LCS approach for measuring separation between nearby trajectories. In this application, however, since we are specifically interested in transport from one pre-defined set to another, we define separation using the boundary of these sets rather than the FTLE.

Before an initial condition in the reduced phase space of the average angle can be advected, it must first be *lifted* to the full $2N$-dimensional phase space. The initial condition in the reduced space determines $\hat{\theta}_0$ and $\dot{\hat{\theta}}_0$ exactly; however, the higher order components are free to be chosen arbitrarily and hence the lifting procedure is not unique. Presently, we compare the transport structures present when lower order modes are activated with the transport structures obtained when higher order modes are activated in order to make connections with the activation energies recorded in Figure 8.3. After lifting to the full space, the initial condition is then integrated using either the full system of equations or the reduced model.

Sample results obtained from this visualization procedure using the reduced order model are shown in Figure 8.7 and reveal manifolds in the flow that govern transport. For clarity of this initial presentation, the initial condition used in the visualization process was lifted to the full space by adding energy to only the first mode yielding a periodic time-dependence in the reduced model. Just as for the perturbed pendulum of Chapter 4, the intersection of the blue and red boundary surfaces define *lobes* that mediate transport in the flow. Indeed, the manifolds reveal that transport occurs via the now familiar mechanism of lobe dynamics that attends a perturbed homoclinic trajectory.

In Figure 8.8, snapshots of the trajectories inside two of the lobe regions taken for different values of t_0 have been suitably colored to indicate explicitly the action of lobe dynamics in this example. We observe that trajectories colored red are captured

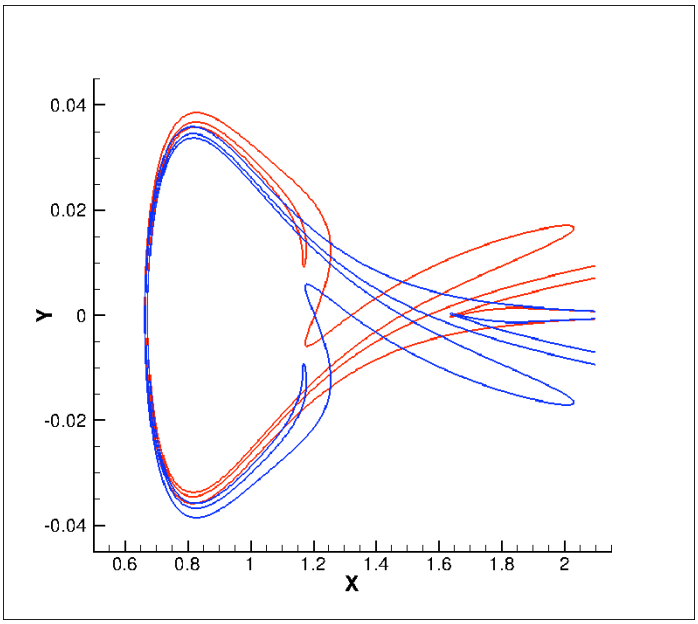

Figure 8.7: Surfaces that govern transport in the flow of the reduced model for the parameter values provided in 8.2.1 are visualized here using the method described in the text. Blue surfaces separate regions that will undergo conformation change from those that will not when trajectories are integrated *forward* in time. Conversely, red surfaces separate regions that will undergo conformation change from those that will not when trajectories are integrated *backward* in time. Together the surfaces reveal the familiar structure of a perturbed homoclinic tangle. This visualization is computed for the case when the perturbation is created by adding energy to the first mode only.

into the conformation basin, while those colored blue escape from the conformation basin and undergo flipping. Regions in which lobes overlap indicate trajectories that undergo complex itineraries, i.e., drifters in an overlapping region may first be captured into the conformation basin and then subsequently escape. Increasing the integration time T reveals more and more intersections and corresponding families of possible itineraries precisely as shown by Smale in the Horseshoe map description of the homoclinic tangle [Smale 1967].

Straightforward linear analysis of the full system reveals that the equilibrium point

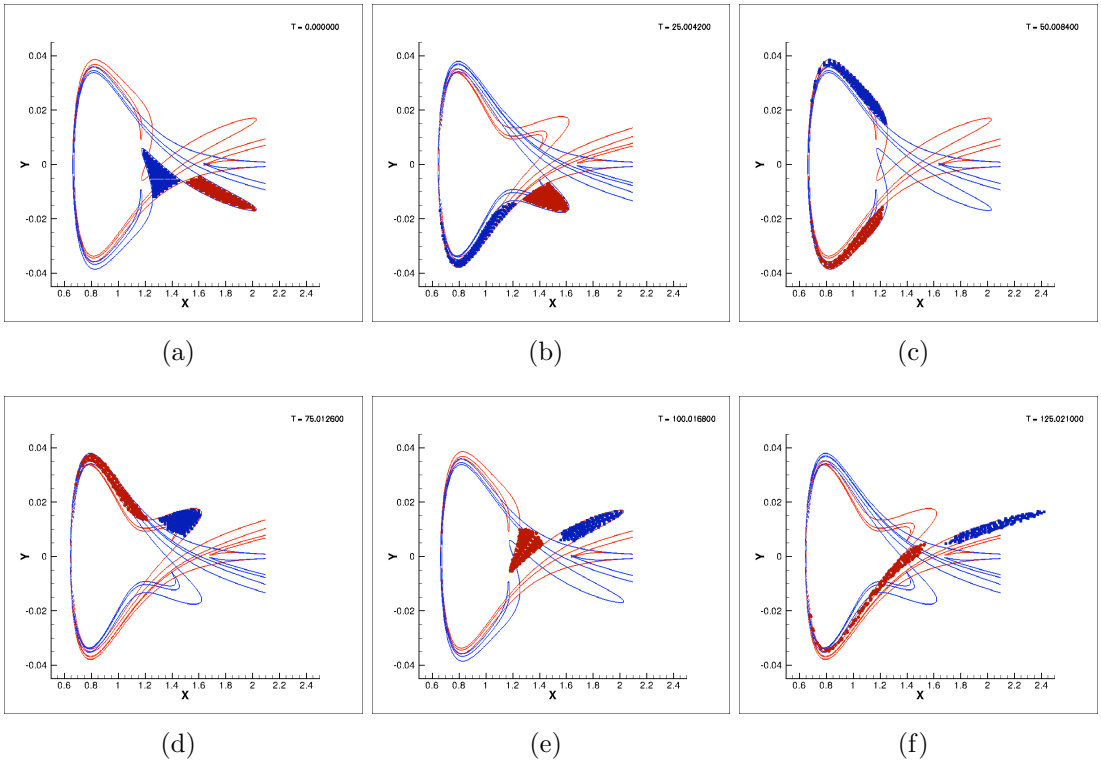

(a) (b) (c)

(d) (e) (f)

Figure 8.8: The action of lobe dynamics associated with the perturbed homoclinic trajectory in Figure 8.7 is easily observed by visualizing the time-dependent manifolds of greatest separation. The intersections of the manifolds define lobes that are either entrained or detrained from the conformation basin. In these snapshots, the trajectories visualized in red have recently flipped and are captured into the conformation basin. Conversely, the blue trajectories begin within the conformation basin and then escape and undergo flipping.

at $(\pi, 0)$ has $2N$ eigenvalues:

$$\lambda_{\pm}^{p} := \pm\sqrt{2\cos\left(\frac{2\pi p}{N}\right) - 2 + \epsilon\mu} \qquad p = 0, \ldots, N-1\,, \tag{8.11}$$

where the real number μ is defined by

$$\mu := 2a\left(1 - e^{-a(2-x_0)}\right)e^{-a(2-x_0)}\,. \tag{8.12}$$

The reasonable assumption that the Morse potential equilibrium distance x_0 is less than twice the pendulum length guarantees that μ is positive.

When epsilon is identically zero, one pair of eigenvalues lies at the origin, while all the remaining eigenvalues fall along the imaginary axis in complex conjugate pairs. For small non-zero epsilon, the zero eigenvalues are perturbed off the origin along the real axis yielding a symmetric pair of real eigenvalues. Precisely when

$$0 \leq \epsilon < \frac{2 - 2\cos\left(\frac{2\pi}{N}\right)}{\mu} \tag{8.13}$$

the set of eigenvalues contains only one real pair and the equilibrium point is a rank 1 saddle, i.e., the linear stability of the equilibrium point is of the type saddle $\times$ center$_1$ $\times$ $\ldots$ $\times$ center$_{N-1}$. Transport in systems with rank 1 saddles has been well-studied with regard to low-dimensional applications in celestial mechanics and molecular dynamics. The results of Koon et al [Koon 2000] show that transport in systems with rank 1 saddles is governed by tubes defined by the invariant manifolds of the periodic orbit: trajectories inside the tube defined by the stable manifold, for example, will cross the saddle and be transported inside the tube from one region to another. For the parameters given for the coupled oscillator system in section 8.2.1, the inequality in condition (8.13) is satisfied whenever N is less than 24,000 and hence for $N = 200$ the equilibrium point associated with all the pendula in the flipped position at π radians is indeed a rank 1 saddle. The visualization procedure thus yields the interesting insight that transport via tubes in the full many degrees of freedom system corresponds to lobe dynamics in the projection onto the coarse average coordinates in the reduced model. This observation is currently being pursued further by the author and collaborators as a method for understanding transport in a wide range of molecular systems, such as the atomic cluster described in [Yanao 2007], for example.

We now proceed to use this method for visualizing transport structures to study the effect of the frequency content of perturbations on flipping. Figure 8.9 compares the transport structures obtained when the perturbing energy is initially placed in a range of modes and the resulting initial conditions are then advected using both the reduced and full models. In each of these plots, the amount of energy placed into the perturbing mode is 0.75 energy units – an amount equal in size to the energy required

by the zipper presented in section 8.2.4 to cause a trajectory at the equilibrium point to flip. Blue curves represent the boundary of the flipping region and are determined by integrating the initial conditions forward in time. Recall that this blue curve is not a trajectory, but rather a surface that separates trajectories that will flip from those that will not. In particular, the region enclosed by the blue curve contains initial conditions that will not flip. The gray curve is the homoclinic trajectory for the single pendulum in the Morse potential that defines the basin from which a flipping trajectory must escape. Also, for reference, the black "sawtooth" trajectory of the zipper is shown indicating the manner in which the zipper causes an initial condition at the equilibrium point (represented by a red dot) to flip. Since the equilibrium point in each of the plots falls inside the blue separatrix, none of the perturbations (except for the zipper) are able to induce flipping of trajectories starting at the equilibrium point at this particular energy level.

A study of the plots in Figure 8.9 yields several observations that in many ways serve as a summary of the chief results of this chapter. These observations are listed here:

- Qualitatively, *the reduced model captures the transport structures in the projected phase space remarkably well.* For the case when the initial energy is placed in mode 10, the reduced model does not provide the correct amplitude of the lobes, yet the frequency of the lobes and the overall proportions of the area delineated by the separatrix are very similar. For higher order modes all the relevant features are captured correctly and the differences between the reduced model and full model become visually indistinguishable. A single degree of freedom model obtained through averaging or truncation methods fails to capture flipping entirely. The time-dependence in the reduced model encodes the effect of the initial conditions of the full system so as to include the effect of higher order modes in inducing flipping.

- Perturbations consisting of higher order modes are less efficient at inducing flipping since the lobe structures are much smaller and the region inside the blue

separatrix that represents trajectories that do not undergo flipping is enlarged. For the case when the perturbing energy is placed in mode 40, for example, we see that no flipping is induced whatsoever. This observation serves as a visual representation of the fact that the conformation basin is impervious to noisy perturbations with high frequency content as has been previously observed in section 8.2.4. *The biomolecule chain is robust to noisy perturbations.*

- The zipper is an efficient and robust method for inducing conformation change that utilizes only localized perturbations. Certainly, perturbations with low frequency content are efficient at unzipping the chain; however, these perturbations have global structure. Hence, *conformation change in the biomolecule chain can be robustly induced via a low-energy, localized structured perturbation.*

In summary, then, we have introduced a strategy for deriving an approximate reduced equation for the evolution of a coarse variable in a high degree of freedom system in a way that carefully includes the influence of fine-scale dynamics, and have applied it to a simplified model for biomolecules. It has been shown that the basic mechanism of global conformation change can be understood using a single degree of freedom dynamical system that is acted on by an explicitly computable "subgrid" time-dependent forcing that represents the effect of the higher order modes on the main mode. We have also demonstrated that conformations are robust to large random perturbations, yet conformation change can be robustly induced by the application of a small, local structured perturbation. Visualization of transport in the coarse variables of the reduced model indicates that one channel through which conformation change occurs for a large class of perturbations is the process of lobe dynamics associated with the perturbed homoclinic trajectory of a rank 1 saddle.

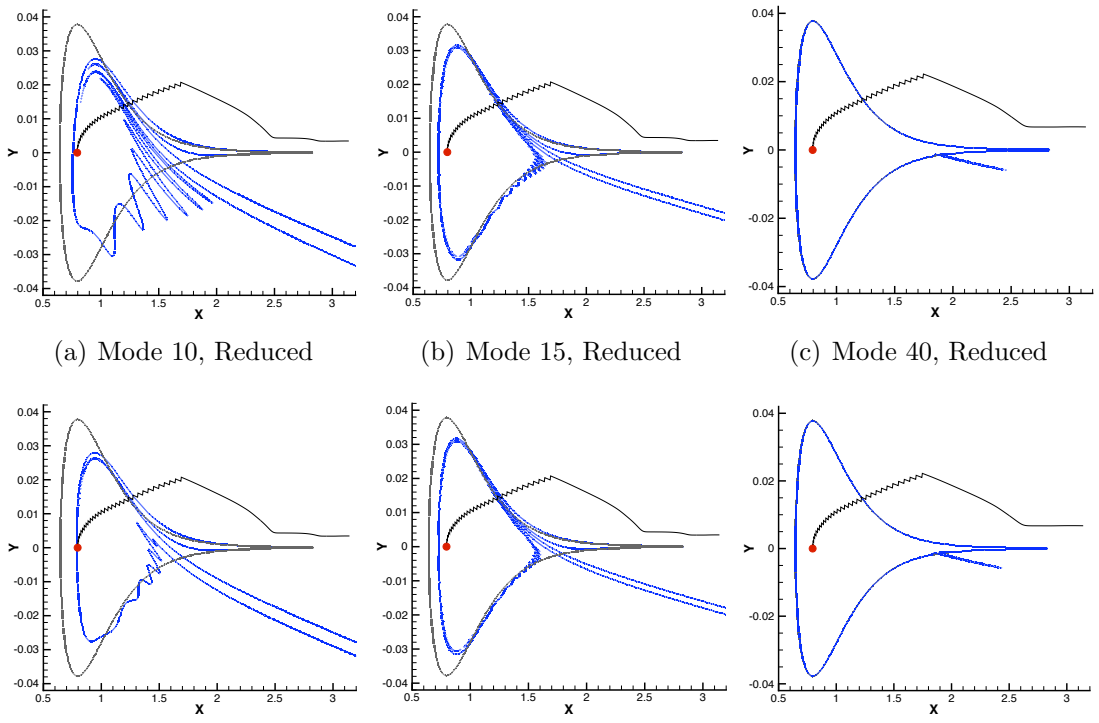

(a) Mode 10, Reduced (b) Mode 15, Reduced (c) Mode 40, Reduced

(d) Mode 10, Full (e) Mode 15, Full (f) Mode 40, Full

Figure 8.9: As described in more detail in the text, transport structures in the phase space of the average variables for the biomolecule are compared here for both the full and the reduced models. A review of the plots leads to the following observations: 1.) For perturbations in mode 10, the reduced model predicts incorrect amplitudes for the lobe structures, yet the overall geometry and topology of the flipping region is well captured. 2.) For perturbations in higher order modes, the transport structures in the reduced model are visually indistinguishable from those of the full model. 3.) Perturbations consisting of lower order modes are more efficient at inducing flipping motion. 4.) The zipped conformation of the chain is robust against high frequency perturbations. 5.) The zipper induces flipping efficiently while using only a localized perturbation.

Chapter 9

Properties of LCS

The preceding chapters have illustrated the effectiveness of using the FTLE-LCS method for revealing transport mechanisms in geophysical flows, and in flows defined by a dynamical system. In other fields, researchers are harnessing the utility of the method for revealing coherent structures in a wide array of aperiodic flows. However, the number of papers dealing with the theoretical underpinnings of FTLE and LCS has not grown proportionately. Since Haller's original inception of the idea [Haller 2000, Haller 2001], excellent contributions to the theory of LCS have been provided by [Shadden 2005] and [Lekien 2007], which provide rigorous definitions for LCS that had not previously been codified, as well as a bound for the amount of flux that crosses the LCS. Haller has also explored the robustness of LCS to noise in the velocity field [Haller 2002], and used the premise of LCS to analyze criteria for separation in unsteady flows in [Surana 2008, Weldon 2008]. Motivated by applications, several groups have also provided an equivalent LCS theory for inertial particles in a flow [Sapsis 2009, Tallapragada 2008, Peng 2009]. This being said, the literature contains very little analysis on the fundamental *properties* of LCS – that is, given a rigorous definition of the LCS, what properties follow from this definition?

In tandem with this want of rigorous theoretical results, there have been, in the LCS literature over the last decade, tacit assertions made regarding the properties of LCS. In many cases, these assertions have been made as a pedagogical tool to illustrate an idea by analogy; however, many end users of the theory have consequently attributed these properties as statements of fact. To be sure, the proponents of LCS

theory have not made errors in their analysis. However, in the presentation of ideas, these assertions have often been propagated. Indeed, there is hardly a published paper utilizing the LCS method that does not make these assertions to some degree.

Most commonly, the assertions to which we are referring are the following:

A1. The repelling/attracting LCS generalize stable/unstable manifold theory from autonomous flows to aperiodic flows.

A2. LCS are invariant, or stated differently, the LCS are material surfaces.

In this chapter, we will investigate the LCS in relation to these two properties. The approach will use both analysis and examples to illustrate the ideas, and to provide direct counterexamples.

One reason for the slow development of a theory surrounding LCS beyond the applications is the lack of readily available approaches for analysis. As we have seen, the LCS is defined in terms of the derivatives of the flow map, whereas, for the analysis we would like to determine properties of the LCS in terms of the underlying velocity field. For the aperiodic flows we are considering, the flow map can only be determined by numerical integration. Moreover, the LCS is defined in terms of a derivative condition on the flow map, and verification of the properties of the LCS requires access to the derivatives of this condition.[1] With this in mind, this thesis does not claim to provide the needed breakthrough in the analysis. It is hoped, however, that an informed discussion of these issues will help to provide a more rigorous framework in which to continue development of FTLE-LCS theory.

We proceed by addressing each of the previously stated assertions in turn. The final section of this chapter will then investigate the possibility of an evolution equation for the LCS in terms of the underlying velocity field.

[1]The difficulty of the situation can be appreciated anecdotally by referring to a conversation of the author with Dr. Peter Constantin, of the University of Chicago, who, after hearing of the attempt to provide further analysis for LCS, and realizing the need to come to terms with the flow map with arbitrary time dependence, exasperatedly exclaimed: “Heaven help you!”.

9.1 LCS and stable and unstable manifolds

Recall that, given a hyperbolic fixed point, p, in an autonomous velocity field, the stable and unstable manifolds of p are defined as the union of points whose trajectories asymptote toward p as $t \to \infty$ and $t \to -\infty$, respectively. Even in this thesis, we have seen applications in which the correspondence between LCS and stable/unstable manifolds appears very convincing. In our very first example (the simple pendulum of Chapter 3), the LCS appears to coincide precisely with the well-known stable and unstable manifolds for pendulum flow. Even the fact that the LCS "grow" away from the fixed point as the integration time, T, is increased, is suggestive of the definition of stable and unstable manifolds. Further examples in this thesis have used the LCS method to reveal homoclinic tangle structures in a variety of aperiodic flows that unmistakably resemble the stable and unstable manifolds of Poincaré maps associated with periodically forced flows. Further evidence for the link between LCS and manifolds is the observation that stable and unstable manifolds traditionally define *separatrices* in a time-independent flow, just as has been shown for LCS which, *by definition*, are surfaces of greatest separation. In addition, the property that stable and unstable manifolds are invariant manifolds seems to be true for LCS computed numerically in physical flows (although this property will be examined more closely in the next section.)

Given the aforementioned observations, it is understandable that analogies have been made between LCS and stable/unstable manifolds, leading prematurely to the conclusion that LCS represent the generalizations of these manifolds from autonomous flows to aperiodic flows. For this claim to be true, there needs to be a mathematical link between asymptotic trajectories (in the definition of manifolds) and separation (in the definition of LCS). We shall now see through example that this link does not hold necessarily, and that an important criterium to monitor in this regard is the rate of separation along the unstable manifold.

Before proceeding, we introduce the following definitions that will be useful when discussing the examples:

Definition: Let $\mathbf{u}(\mathbf{x})$ be an autonomous velocity field defined on $\mathbb{R}^2$ that has a hyperbolic fixed point, $\mathbf{p} \in \mathbb{R}^2$. Denote the one-dimensional invariant unstable manifold of $\mathbf{p}$ as $W^u(\mathbf{p})$. For a point $\mathbf{x}_0^u \in W^u(\mathbf{p})$, let $\mathbf{x}^u(t, \mathbf{x}_0^u)$ denote the solution trajectory parameterized by time for which $\mathbf{x}^u(0, \mathbf{x}_0^u) = \mathbf{x}_0^u$. Let $s(t; \mathbf{x}_0^u)$ be the arclength along the trajectory $\mathbf{x}^u(t; x_0)$ also parameterized by time, so that $s(0; \mathbf{x}_0^u) = 0$, and $s(t; \mathbf{x}_0^u)$ is a strictly increasing function in t. Then, for $T > 0$, the unstable manifold $W^u(\mathbf{p})$ is said to be

- *sublinear* up to time T if

$$\frac{d^2}{dt^2} \ln s(t, \mathbf{x}_0^u) < 0 \tag{9.1}$$

- *superlinear* up to time T if

$$\frac{d^2}{dt^2} \ln s(t, \mathbf{x}_0^u) > 0 \tag{9.2}$$

- *linear* up to time T if

$$\frac{d^2}{dt^2} \ln s(t, \mathbf{x}_0^u) = 0 \tag{9.3}$$

for all $t \in [0, T]$, and for all $\mathbf{x}_0^u$ in some neighborhood of p.

By choosing T small enough, every unstable manifold can be assigned one of these definitions.

Example 1. Flow near a linear saddle: The quintessential flow that exhibits stable and unstable manifolds in an autonomous flow is the linear saddle. Consider the linear flow in the coordinates $\mathbf{x} = (x, y)$ prescribed by

$$\dot{\mathbf{x}} = A\mathbf{x}\,, \qquad\qquad A := \begin{bmatrix} 1 & 0 \\ 0 & -1 \end{bmatrix}. \tag{9.4}$$

The streamlines for this flow are plotted in Figure 9.1. In this case, we can solve for

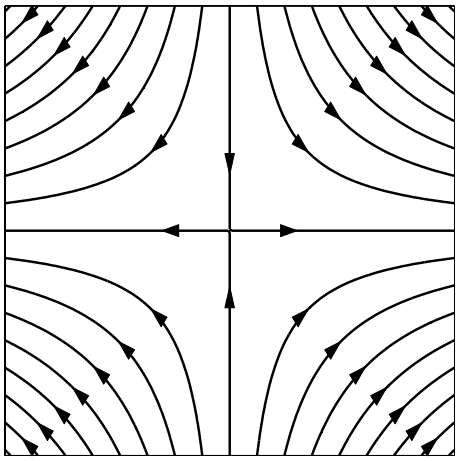

Figure 9.1: Streamlines in the flow of a linear saddle.

the flow map, and the FTLE analytically. An initial condition, $\mathbf{x}_0 = (x_0, y_0)$, mapped forward in the flow becomes

$$\mathbf{x}(t_0 + T) = \begin{bmatrix} x_0 e^T \\ y_0 e^{-T} \end{bmatrix} . \tag{9.5}$$

The linearization of the flow map is

$$\left.\frac{d\phi_{t_0}^{t_0+T}}{d\mathbf{x}}\right|_{\mathbf{x}=\mathbf{x_0}} = \begin{bmatrix} e^T & 0 \\ 0 & e^{-T} \end{bmatrix} , \tag{9.6}$$

and the deformation tensor is

$$\Delta = \begin{bmatrix} e^{2T} & 0 \\ 0 & e^{-2T} \end{bmatrix} . \tag{9.7}$$

Finally, following the definition in (3.3), the FTLE is

$$\sigma(\mathbf{x}, t) = 1 . \tag{9.8}$$

The FTLE is constant in both space and time, and hence admits neither ridges nor LCS. This result is, of course, not surprising since the flow map itself is independent of

both space and time. We conclude that all points in the flow separate at an equal rate, regardless of their initial location with respect to the stable and unstable manifolds; in particular, initial conditions straddling the stable manifold separate at the same rate as all other trajectories in the flow. In effect, all particles are slaved to the unstable manifold and separation of particles along the unstable manifold is uniform. This trivial example indicates that *LCS computed using FTLE cannot generalize stable and unstable manifolds to aperiodic systems since we have an example in which LCS do not reduce to the stable and unstable manifolds in the autonomous case.*

In terms of the definitions provided above, the unstable manifold in this example is *linear* and represents a critical case. Insight is gained by examining two further examples that represent *sublinear* and *superlinear* cases.

Example 2. Flow due to two point vortices: Consider the potential flow generated by two point vortices with equal and opposite vorticity located at $(-a, 0)$ and $(a, 0)$ in the plane with constant $a > 0$. The stream function describing the flow in a reference frame translating with the vortices is

$$\psi(x, y) = \frac{1}{2\pi}\left[\frac{x}{2a} + \ln\left(\frac{r_2}{r_1}\right)\right], \tag{9.9}$$

where r_1 and r_2 are the distances from the point (x, y) to the first and second vortices, respectively. The stream function for this autonomous flow is shown in Figure 9.2(a), and the velocity field generated by this stream function is

$$\begin{aligned}\dot{x} &= \frac{1}{2\pi}\left(\frac{y}{r_2^2} - \frac{y}{r_1^2}\right)\\ \dot{y} &= \frac{1}{2\pi}\left(\frac{x+a}{r_1^2} - \frac{x-a}{r_2^2} - \frac{1}{2a}\right).\end{aligned}$$

The flow exhibits two hyperbolic fixed points along the y-axis, and the stable and unstable manifolds associated with these fixed points are well-defined. The heteroclinic manifolds joining the fixed points are separatrices that delineate the region of fluid that translates with the vortex, while fluid outside the heteroclinc connection

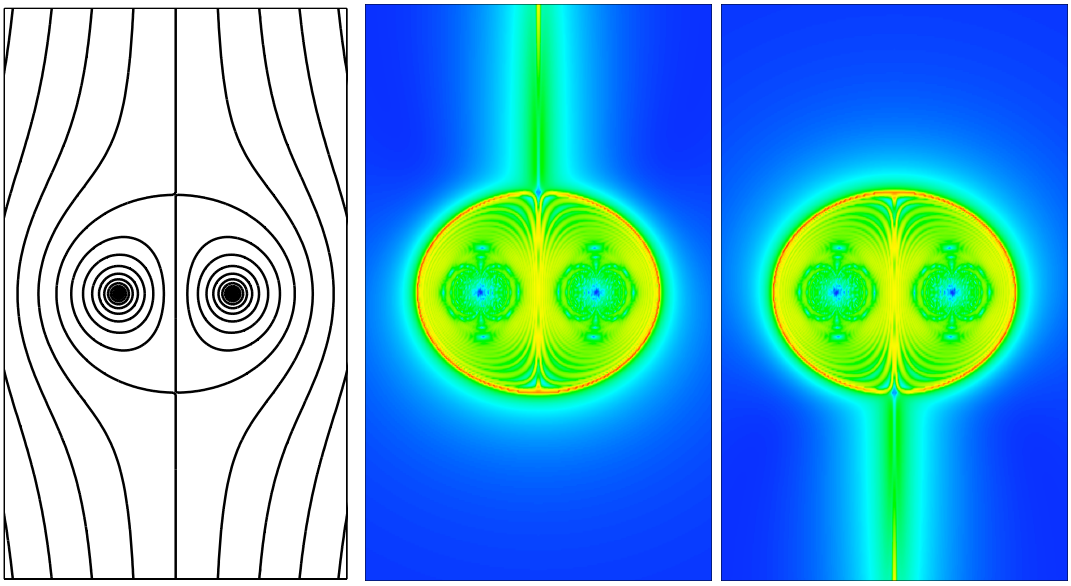

(a) Streamlines. Bulk flow is from top to bottom.

(b) Repelling FTLE.

(c) Attracting FTLE.

Figure 9.2: LCS in the flow of the double point vortex flow. The repelling and attracting LCS coincide with the stable/unstable manifolds.

appears to move downward and out of the field of view.

The corresponding FTLE fields for this flow computed numerically are shown in 9.2(b) and 9.2(c). The bulk flow outside the vortex is a largely uniform flow in which there is no separation and the deformation tensor is zero. Hence, the largest separation occurs between the flow inside the vortex and the bulk flow, and consequently the LCS does indeed agree with the stable and unstable manifolds. For this example, the stable and unstable manifolds coincide with the LCS, and is a case in which the velocity field along the unstable manifold is *sublinear*.

Example 3. Flow in Hill's vortex: In an 1884 monograph (see reference at [Hill 1894]), Hill considered a three-dimensional flow with an axis of symmetry. Taking the z-axis as the axis of symmetry, and using cylindrical coordinates (r, θ, z), he showed that level surfaces defined by

$$r^2\left(r^2 + z^2 - 1\right) = \text{constant} \tag{9.10}$$

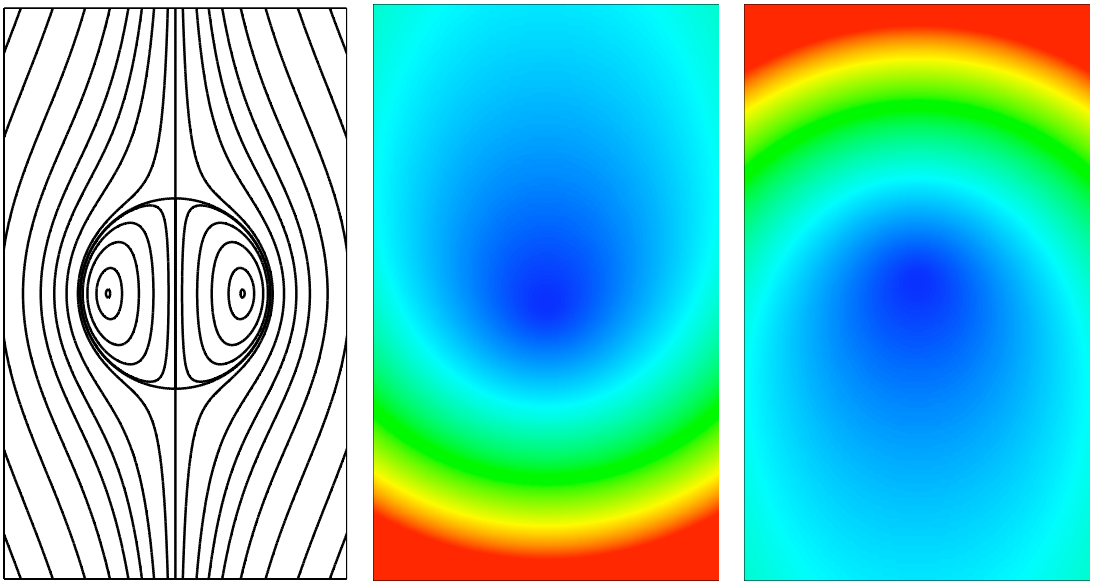

(a) Streamlines. Bulk flow is from top to bottom.

(b) Repelling FTLE.

(c) Attracting FTLE.

Figure 9.3: LCS in the flow of Hill's spherical vortex. The FTLE fields admit neither ridges nor LCS.

are invariant surfaces under the axisymmetric flow defined by[2]

$$\dot{r} = 2rz \tag{9.15}$$

$$\dot{\theta} = 0 \tag{9.16}$$

$$\dot{z} = -2(2r^2 - 1) - 2z^2 \,. \tag{9.17}$$

Figure 9.1 shows the streamlines (invariant surfaces) on a planar section of the flow through the axis of symmetry. The streamline patterns are very similar to those

[2]Hill's result was actually more general than this. He showed that the level surfaces of

$$r^2 \left(\frac{r^2}{a^2} + \frac{(z-Z)^2}{c^2} - 1 \right) = \text{constant} \tag{9.11}$$

are invariant under the flow

$$\dot{r} = 2\frac{k}{c^2} r(z - Z) \tag{9.12}$$

$$\dot{\theta} = 0 \tag{9.13}$$

$$\dot{z} = -2\frac{k}{a^2}(2r^2 - a^2) - 2\frac{k}{c^2}(z - Z)^2 \tag{9.14}$$

for arbitrary constants a, c, and k, and any function of time Z.

for the previous flow arising from two point vortices – the geometric structure of the stable and unstable manifolds are identical. However, the important difference is that the bulk flow *accelerates superlinearly* as it travels in the direction of the negative z-axis, and the z-coordinate of the flow becomes infinite in finite time – the culprit being the $-z^2$ term in the z-component of the velocity.

Although the structure of the stable and unstable manifolds of the Hill vortex flow and the point vortex flow are identical, the FTLE fields are very different. The FTLE fields for the Hill vortex are shown in Figure 9.3. The FTLE has a smooth gradient that does not admit ridges – *there are no LCS in this flow.* Particles initially located further down the negative z-axis experience larger separation in a fixed amount of time. Hence, separation in the flow is not at all related to the location of stable and unstable manifolds. Separation along the unstable manifold in this example is *superlinear.*

Reviewing the results in these three examples, we can conclude that flows must be sublinear for the repelling LCS to correspond with the stable manifold, and likewise the attracting LCS with the unstable manifold. Otherwise, the faster than exponential rate of stretching ensures that the greatest rate of separation will not occur at the stable manifold.

We can attribute the fact that excellent agreement of the LCS with stable and unstable manifolds has been routinely found in physical flows (such as oceans, atmospheres, laboratory flows, etc.) to the observation that flows in these applications are physical and characteristically sublinear; the rate of separation along unstable manifolds does not grow without limit, but rather reduces with distance from the hyperbolic fixed point.

9.2 Invariance of the LCS

We now turn our attention to the assertion that LCS are invariant. Invariance is one of the defining characteristics of stable and unstable manifolds for autonomous sys-

tems, and hence the similarities between LCS and stable/unstable manifolds discussed previously, as well as the apparent invariance of the LCS observed in the applications, warrant a further study of this issue.

The question of invariance in relation to LCS contains two more subtle features that must be mentioned with regard to this matter. In the seminal paper of Haller [Haller 2000], LCS are defined as surfaces that are *always* repelling. It clearly follows that a surface that is always repelling will have no flux across it, and is necessarily invariant. However, the method he proposed for discovering these surfaces, namely the FTLE method, does not guarantee this property *a priori*. Haller regarded the FTLE method as a manner in which to approximate the "true" LCS that *are* invariant by definition, and posited that any flux across the LCS is an artifact of the FTLE approximation method. In contrast, Shadden's approach in [Shadden 2005] is to *define the LCS in terms of the FTLE*, and then to examine how invariant the LCS defined in this way actually are. The difference is somewhat semantic, but helps to explain some of the confusion as to whether LCS should be ascribed the property of invariance.

A second factor must also be considered. The group of Wiggins *et al.* have developed a separate method for extracting coherent structures in aperiodic flows called the "Distinguished Hyperbolic Trajectory" (DHT) method [Ide 2002]. The reader is referred to the references for a deeper study of this approach, however, the underpinning methodology is to first identify an "instantaneous stagnation point" (ISP) in the flow, the continuous motion of which defines a "distinguished hyperbolic trajectory" about which the linearized flow is maximally hyperbolic. The linearization about the ISP provides the linear subspaces that provide initial guides along which to search for the global stable and unstable manifolds. These manifolds are then declared to be the important structures in the time-dependent flow, and their time-dependence is obtained by advecting them forward in time using the given velocity field. The question of whether to use the FTLE approach or the DHT approach is largely a matter of preference; however, we have found that in analyzing geophysical flows, the DHT method has not been as effective because of the need to identify ISP's

which for many flows of interest are not Gaililean-invariant, or as is often the case, do not exist. The crucial point, though, is that in the DHT method the resulting time-dependent LCS are advected by the flow, and hence by definition, are invariant material surfaces. The development of this DHT method for extracting LCS, in which the LCS *are* invariant by definition, provides some additional confusion as to the invariance of the LCS for the FTLE-LCS method.

As mentioned previously, Shadden has provided a bound on the flux rate across an LCS, and has also verified numerically for an oceanic flow that flux across the LCS is almost negligible and falls within the numerical uncertainty of the calculation. The numerical results have led Haller to suggest (in conversation) that perhaps the flux estimate is not sharp, and that perhaps further analysis will reveal that FTLE-LCS are indeed invariant.

In this section, we will now present an example for which the FTLE-LCS is clearly not invariant – there is unambiguous flux across the LCS. Before presenting the example, we hasten to say that the Shadden flux estimate is not violated for this example. The example is a "pathological" case in which the underlying velocity field is smooth, but nevertheless has large temporal and spatial gradients. It is hoped that the example will be instructive in many ways. Beyond simply settling the question of the invariance of the FTLE-LCS, the example provides an indication of why a theory for LCS in time-dependent flows *must* admit flux across the LCS; *an invariant LCS may quickly become an irrelevant LCS.*

Example: Consider the flow in the xy-plane prescribed by

$$\dot{x} = 0.4 \tanh 10(x - 0.5t) \tag{9.18}$$

$$\dot{y} = 0\,. \tag{9.19}$$

This flow is only cheaply two-dimensional; the y-coordinate of each trajectory remains constant, and we need only consider the evolution of $x(t)$. As shown in Figure 9.4(a), the $\dot{x}$-component of the velocity field has a sigmoidal shape in space

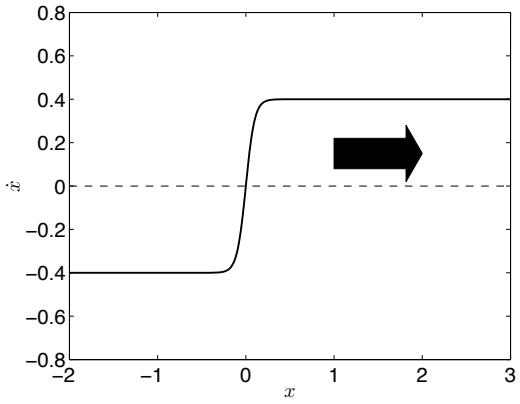

(a) Snapshot of the x-component of velocity as a function of the x-coordinate. In time, the sigmoidal velocity wave-front translates to the right.

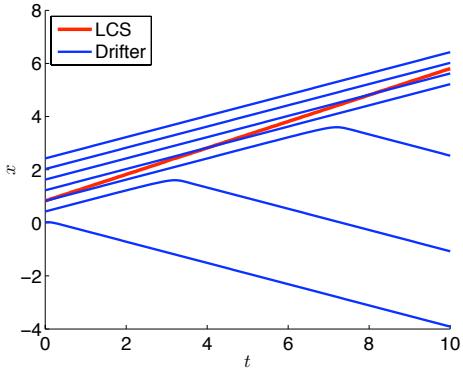

(b) The x-coordinate of drifter locations as a function of time are plotted in blue. The x-coordinate of the repelling LCS is shown in red, indicating the presence of flux across the LCS.

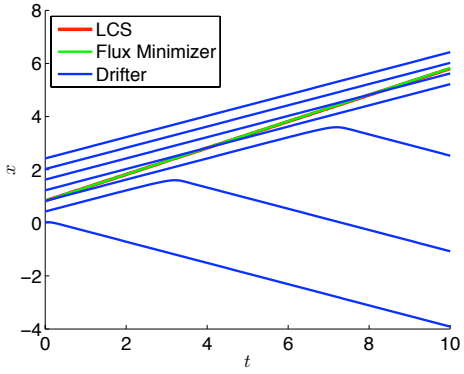

(c) The x-coordinate of the flux-minimizing path is plotted in green and coincides with the trajectory of the LCS. The flux minimizing path is derived in Section 9.2.1.

Figure 9.4: LCS in the flow of a sigmoidal wave front flow.

that propagates in time with constant speed in the direction of the positive x-axis. The important feature to notice is that the velocity profile translates with a velocity of 0.5 that is greater than the velocity of the fastest drifters in the flow (0.4). The factor of 10 in the argument of the tanh() function controls the steepness of the sigmoidal wave-front.

Computation of the FTLE for this flow reveals that the LCS is an infinite line parallel with the y-axis, that translates to the right, and in this way tracks the velocity front. In order to investigate flux across the LCS, we plot the x-location of the LCS

in relation to passive drifters in the flow. In Figure 9.4(b), where the horizontal axis is time, the x-coordinate of the LCS is shown to translate at a constant speed of 0.5 and tracks the wave-front. Drifter trajectories, however, are overtaken by the LCS, thus inducing continuous flux across the LCS. Clearly, the LCS in this example is not a material line, and not invariant.

It is instructive to compare the final location of the FTLE-LCS with a material line that originates at the same location. The LCS has translated to the right to keep pace with the velocity wave front which is the surface of greatest separation and the most important structure in the flow. The material line, on the other hand, is left behind in the wake of the flow. Thus, while an LCS that is materially advected remains invariant, it may no longer represent the important coherent structure in the flow. The implications of this observation are that we should not expect a theory that identifies coherent structures in aperiodic flows to provide LCS that are invariant, and the property of invariance may need to be sacrificed in order to ensure proper tracking of the relevant coherent structures. Further investigation of this example in the next section reveals the further subtle feature that the FTLE-LCS not only remains the relevant coherent structure in the flow, but does so in a manner that minimizes the flux. In other words, in this example, the FTLE-LCS provides the optimal tradeoff between tracking important structures and maintaining as much invariance as possible.

9.2.1 Motion of a Flux Minimizing Surface

Consider an arbitrary time-dependent velocity field, $\mathbf{f}(\mathbf{x}, t)$, defined on the plane, and suppose that $L^{t_0}(c)$ is a one-dimensional curve in the plane at time t_0 parametrized by $c \in [0, 1]$, and that $L^{t_1}(c)$ is another one-dimensional curve in the plane at time t_1 also parametrized by $c \in [0, 1]$, with $t_1 > t_0$. The situation is depicted in Figure 9.5.

We now propose the problem of choosing a one-parameter family of paths, $\mathbf{x}(c, t)$, in which the parameter c enumerates the paths, and each path is parametrized by time, t, so that $\mathbf{x}(c, t_0) = L^{t_0}(c)$, $\mathbf{x}(c, t_1) = L^{t_1}(c)$, and the flux induced by the velocity

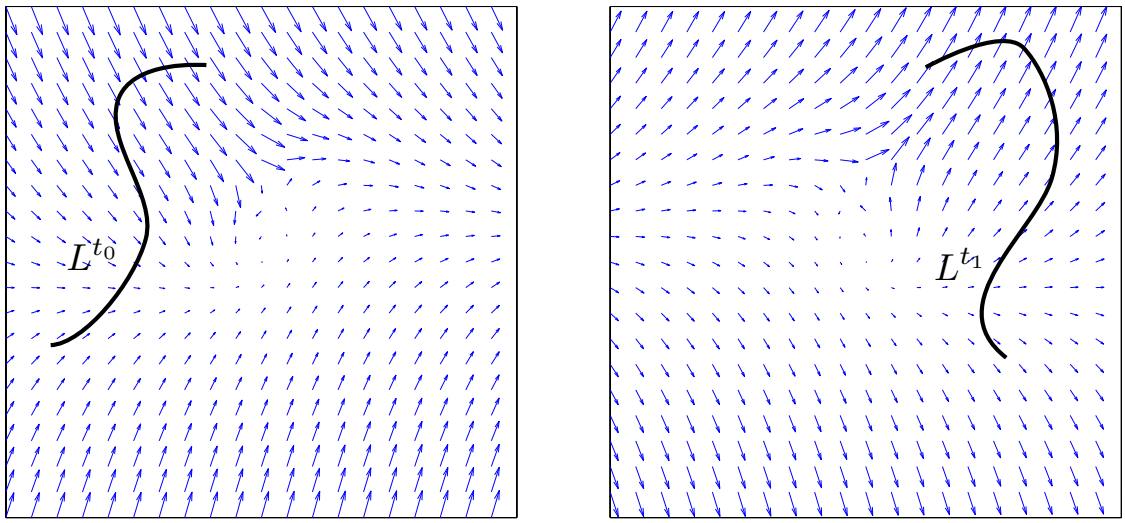

(a) time = t_0 (b) time = t_1

Figure 9.5: L^{t_0} is a curve shown at time t_0. L^{t_1} is a different curve at a later time, t_1. In the text, we derive the "most Lagrangian" transformation from L^{t_0} to L^{t_1} through the time-dependent velocity field.

field across each path is minimized. Said another way, we wish to choose the motion of the points located at $L^{t_0}(c)$ for $c \in [0,1]$ at time t_0 through the plane so that they arrive at corresponding points on the curve $L^{t_1}(c)$ for $c \in [0,1]$ at time t_1, and do so in a way that minimizes flux across each point. We can imagine the curve translating while morphing and changing its shape so that it arrives at $L^{t_1}(c)$ at time t_1 in a way that follows as closely as possible the underlying velocity field so as to reduce the flux. In this way, we hope to find "the most Lagrangian transformation" from L^{t_0} to L^{t_1}.

If $L^{t_1}(c) = \phi_{t_0}^{t_1}\left(L^{t_0}(c)\right)$ for all $c \in [0,1]$, where $\phi_{t_0}^{t_1}$ is the flow map for the velocity field $\mathbf{f}$, then the solution to the problem is obtained trivially by simply advecting the curve at time t_0 by the flow until time t_1. The advected curve will satisfy the boundary conditions, and will behave as a material line with precisely zero flux. However, for arbitrary placement of the final curve L^{t_1}, the motion of points along the curve must be found by applying a *variational principle*.

The motion of the point labelled by c is "most Lagrangian" when the flux integral

across the point is stationary:

$$\delta \int_{t_0}^{t_1} ||\dot{\mathbf{x}}(c,s) - \mathbf{f}(\mathbf{x}(c,s),s)||^2 \, ds = 0 \,. \tag{9.20}$$

The integrand can be considered a Lagrangian of the form:

$$L(\mathbf{x}, \dot{\mathbf{x}}, t) = ||\dot{\mathbf{x}}(c,t) - \mathbf{f}(\mathbf{x}(c,t),t)||^2 \,. \tag{9.21}$$

The Euler-Lagrange equations,

$$\frac{d}{dt}\left(\frac{\partial L}{\partial \dot{\mathbf{x}}}\right) - \frac{\partial L}{\partial \mathbf{x}} = 0 \,, \tag{9.22}$$

that arise from the variational principle yield

$$\ddot{\mathbf{x}} = \frac{\partial \mathbf{f}}{\partial t} + (\nabla \mathbf{f})' \cdot \mathbf{f} + (\nabla \mathbf{f} - (\nabla \mathbf{f})') \, \dot{\mathbf{x}} \tag{9.23}$$

for the second order dynamics of the flux minimizing point. The constants of integration are chosen to satisfy the boundary conditions.

The curve $\mathbf{x}(c,t)$ obtained by solving the boundary value problem is the path that moves through the time dependent velocity field from point $L^{t_0}(c)$ at time t_0, to the point $L^{t_1}(c)$ at time t_1, in such a way that it minimizes flux, and is most Lagrangian.

We have computed the flux-minimizing trajectory for the sigmoidal velocity-front example discussed earlier. The path of the flux-minimizing trajectory is plotted in Figure 9.4(c) and indicates that, for this example at least, the FTLE-LCS moves precisely along the trajectory that minimizes flux. Although the LCS is not invariant, it allows flux in order to retain its status as the important coherent structure, and does so in a manner that is optimal with respect to minimizing flux.

An added point to make here is that these findings indicate a manner in which to efficiently solve for the approximate motion of the LCS. If the location of the LCS is computed at time t_0, and at a much later time t_1, then the motion of the LCS during the interval of time (t_0, t_1) can be interpolated using the evolution of the

the flux minimizing curve. This ostensibly saves computation, since a large grid of trajectories no longer needs to be integrated at each time step, and improves upon the procedure of simply advecting the LCS by the velocity field which we have seen in the example can become largely inaccurate.

9.3 Equations of Motion for the LCS

In all the examples of the FTLE-LCS method provided in previous chapters, the time-dependence of the LCS is obtained by computing the location of the LCS at many time steps, and then animating the resulting frames to learn the motion of the LCS. This requires the computation of the FTLE over the entire region at many time steps, and the time-dependence of the LCS is an emergent feature extracted from the computed data. In this section, we address the time-dependence of the LCS in a different manner. In particular, we ask the question: "Given a velocity field, $\mathbf{f}(\mathbf{x}, t)$, and any needed derivatives, can we write evolution equations for the motion of the LCS?" If so, we will then, in principle at least, be able to solve for the motion of the LCS by direct integration of their deterministic equations of motion, without having to compute the FTLE everywhere and then extracting the apparent motion of the LCS.

In the discussion that follows we will proceed to derive equations of motion for the LCS and thus answer this question affirmatively. Unfortunately, however, the resulting equations of motion do not simplify to just a few explicit terms, but contain many terms defined up to quadrature that place a shadow over their utility for numerical computations. Nevertheless, we proceed with the analysis because (a) the idea of obtaining direct equations of motion for the LCS is intrinsically attractive, is worthy in its own merit, and if it can be done, must be done,[3] (b) simplification of the equations of motion (by approximation, for example) may in fact lead to more

[3]The author first started this calculation while visiting the Carlsberg Insititute, the former home of Niels Bohr, in Copenhagen, Denmark, and while discouraged that the calculations did not lead to a simple result, learned from Bohr's grandson, Tomas Bohr, of the long pages and pages of calculations that Bohr provided for his first gold-medal winning paper, and thus took courage.

efficient routines for computing the evolution of the LCS, and (c) having the explicit equations of motion in hand, although not practical for computations *per se*, may provide a breach through which we can attempt to provide further theoretical progress in proving definitive properties of the LCS. With regard to this last point, it is hoped that, just as Picard's iteration is seldom used for numerically integrating ordinary differential equations, but is nevertheless a singularly invaluable tool for proving existence and uniqueness of solutions, the evolution equations for the LCS may also provide insight and methods of proof for the properties of LCS. Certainly, the availability of equations of motion will spark new questions. For example, "Do the evolution equations follow from a variational principle in the velocity field?" At very least, the availability of evolution equations will allow expressions for quantities such as flux across the LCS (the relative motion between the LCS and the underlying flow) in terms of the primitive velocity fields, whereas we presently resort to numerical verifications at discrete time intervals.

In order to present the calculation that leads to the equations of motion, we appeal to the simple case of one-dimensional flow along the real line. This is manifestly the simplest flow we can consider, but it is nevertheless insightful since the same calculation for two-dimensional flow follows exactly analogous steps, albeit cluttered with more terms; and perhaps more importantly, for flow near a hyperbolic point, the flow is, as we have already seen, slaved to the unstable manifold so that for the purposes of understanding separation, we can think of the flow as essentially one-dimensional. In any case, we shall see that even though the flow is trivial, solving for the motion of the LCS may not be.

One-Dimensional Flow: We consider a time-dependent flow on the real line given by

$$\dot{x}(t) = f(x(t), t)\,. \tag{9.24}$$

The corresponding flow map ϕ that integrates points forward in the flow is

$$\phi_{t_0}^{t_0+T}(x_0) := x_0 + \int_0^T f(\phi_{t_0}^{t_0+s}(x_0), t_0+s)\, ds\,. \tag{9.25}$$

For one-dimensional flow, we identify the LCS as the point locations of greatest separation over the integration time T. That is, we must find the points that maximize the separation between two infinitesimally separated points. The scalar field $\sigma(x,t)$ provides the measure of separation:

$$\sigma(x,t) := \lim_{h\to 0} \frac{\phi_t^{t+T}(x+h) - \phi_t^{t+T}(x-h)}{2h} = \frac{d\phi_t^{t+T}(x)}{dx}\,. \tag{9.26}$$

We define the LCS as the locations $x_{LCS}(t)$ of locally maximal separation as measured by σ. Notice that in this setting, the LCS are now single points on the line that we may refer to individually as an "LCS point". Phrased differently, the point $x_{LCS}(t)$ simultaneously satisfies the conditions for a local maximum:

$$\frac{\partial\sigma(x_{LCS}(t),t)}{\partial x} = 0\,, \quad \text{and} \quad \frac{\partial^2\sigma(x_{LCS}(t),t)}{\partial x^2} < 0\,. \tag{9.27}$$

This condition is directly analogous to condition (3.1) for two-dimensional flow.

Our procedure is now to determine the motion of the LCS, $\dot{x}_{LCS}(t)$, by implicitly differentiating this constraint with respect to time. Our final goal is to write the evolution of the location of an LCS point in terms of the velocity field $f(x,t)$ and its derivatives. It will be incumbent upon us, during the evolution, to check that the condition on the second derivative of σ in (9.27) remains satisfied – otherwise, *ridges may become valleys.*

The time evolution of the LCS must be such that condition (9.27) remains satisfied along the path of the LCS point:

$$\frac{d}{dt}\left(\frac{\partial\sigma(x_{LCS}(t),t)}{\partial x}\right) = 0\,,$$

which, after expanding the material derivative, yields

$$\dot{x}_{LCS}(t) = -\frac{\frac{\partial^2 \sigma(x_{LCS},t)}{\partial x\, \partial t}}{\frac{\partial^2 \sigma(x_{LCS},t)}{\partial x^2}} = -\frac{\frac{\partial^3 \phi_t^{t+T}(x_{LCS})}{\partial x^2\, \partial t}}{\frac{\partial^3 \phi_t^{t+T}(x_{LCS})}{\partial x^3}}\,. \tag{9.28}$$

It now remains to write the required partial derivatives of the flow map with respect to space and time in terms of the velocity field, $f(x,t)$. Before doing so, we introduce some helpful shorthand notation. Let,

$$\phi_{m,n} := \left.\frac{\partial^{m+n} \phi_t^{t+T}}{\partial x^m \partial t^n}\right|_{x=x_0}, \tag{9.29}$$

and likewise

$$f_{m,n} := \left.\frac{\partial^{m+n} f}{\partial x^m \partial t^n}\right|_{\substack{t\,=\,t_0+s \\ x\,=\,\phi_{t_0}^{t_0+T}(x_0)}}. \tag{9.30}$$

Then, using

$$\phi_{t_0}^{t_0+T}(x_0) = x_0 + \int_0^T f(\phi_{t_0}^{t_0+s}(x_0), t_0+s)\, ds\,, \tag{9.31}$$

we derive the *variational equations* for the partial derivatives of the flow map. The variational equations are first order differential equations that must be integrated from an initial integration time 0, to the final integration time T, in order to obtain the value of the desired partial derivative. The variational equations for the first time derivatives are

$$\phi'_{1,0} = f_{1,0} \cdot \phi_{1,0} \qquad \phi_{1,0}(0) = 1 \tag{9.32}$$

and

$$\phi'_{0,1} = f_{0,1} + f_{1,0} \cdot \phi_{0,1} \qquad \phi_{0,1}(0) = 0\,. \tag{9.33}$$

The prime notation in these equations denotes differentiation with respect to a time of integration variable, s. Higher derivatives are written in terms of these partial derivatives. After some computation, we find that

$$\phi'_{1,1} = f_{1,1} + f_{2,0} \cdot \phi_{0,1} \cdot \phi_{1,0} + f_{1,0} \cdot \phi_{1,1} \qquad \phi_{1,1}(0) = 0\,, \tag{9.34}$$

$$\phi'_{3,0} = f_{3,0} \cdot [\phi_{1,0}]^3 + f_{1,0} \cdot \phi_{3,0} \qquad \phi_{3,0}(0) = 0\,, \tag{9.35}$$

and finally,

$$\phi'_{2,1} = f_{2,1} + f_{3,0} \cdot \phi_{0,1} \cdot [\phi_{1,0}]^2 + 2f_{2,0} \cdot \phi_{1,0} \cdot \phi_{1,1} + f_{1,0} \cdot \phi_{2,1} \qquad \phi_{2,1}(0) = 0\,. \tag{9.36}$$

In these derivations, we have used the fact that, by definition of LCS, $\phi_{2,0} = 0$ when evaluated on the LCS. These formulae provide a system of coupled ordinary differential equations written explicitly in terms of the velocity field, f, and its derivatives. Integrating these equations will provide the needed quantities in the formula for the evolution of the LCS point.

The complete set of coupled ordinary differential equations is reproduced here:

$$\phi'_{1,0} = f_{1,0} \cdot \phi_{1,0} \tag{9.37}$$

$$\phi'_{0,1} = f_{0,1} + f_{1,0} \cdot \phi_{0,1} \tag{9.38}$$

$$\phi'_{1,1} = f_{1,1} + f_{2,0} \cdot \phi_{0,1} \cdot \phi_{1,0} + f_{1,0} \cdot \phi_{1,1} \tag{9.39}$$

$$\phi'_{3,0} = f_{3,0} \cdot [\phi_{1,0}]^3 + f_{1,0} \cdot \phi_{3,0} \tag{9.40}$$

$$\phi'_{2,1} = f_{2,1} + f_{3,0} \cdot \phi_{0,1} \cdot [\phi_{1,0}]^2 + 2f_{2,0} \cdot \phi_{1,0} \cdot \phi_{1,1} + f_{1,0} \cdot \phi_{2,1}\,. \tag{9.41}$$

Notice that the equations are weakly coupled. In the first step, we may integrate the differential equations for $\phi_{1,0}$ and $\phi_{0,1}$ independently. With these in hand, we may compute $\phi_{1,1}$ and $\phi_{3,0}$. In the third and final step, we obtain $\phi_{2,1}$.

As derived previously in (9.28), the LCS point can then be advected using

$$\dot{x}_{LCS}(t) = -\frac{\phi_{2,1}}{\phi_{3,0}}\,. \tag{9.42}$$

We must also remember to monitor the value of $\phi_{3,0}$ to ensure that the second condition in the ridge definition remains satisfied.

Two-Dimensional Flow: The derivation of the evolution equations for the LCS in two-dimensional flow follows precisely analogous steps, except that the calculation is mired by many more terms generated in the expression – so many that it would be tiresome to use the resulting expressions in a numerical impementation. We provide the initial steps in the calculation here.

We consider a time-dependent flow in the plane given by

$$\dot{\mathbf{x}}(t) = \mathbf{f}(\mathbf{x}(t), t)\,, \tag{9.43}$$

for which the flow map is

$$\phi_{t_0}^{t_0+T}(\mathbf{x}_0) := \mathbf{x}_0 + \int_0^T \mathbf{f}(\phi_{t_0}^{t_0+s}(\mathbf{x}_0), t_0+s)\,ds\,. \tag{9.44}$$

and the FTLE is

$$\sigma(\mathbf{x}, t_0) := \frac{1}{2T} \ln \left[\lambda_{\max} \left[\left(\frac{d\phi_{t_0}^{t_0+T}(\mathbf{x})}{d\mathbf{x}} \right)^T \left(\frac{d\phi_{t_0}^{t_0+T}(\mathbf{x})}{d\mathbf{x}} \right) \right] \right]\,. \tag{9.45}$$

In this two dimensional flow, we can write the expression for the maximum eigenvalue explicitly:

$$\sigma(\mathbf{x}, t) = \frac{1}{2T} \ln \left[\frac{1}{2} \left(\phi_{1,x}^2 + \phi_{2,y}^2 + \sqrt{\phi_{1,x}^4 - 2\phi_{1,x}^2\phi_{2,y}^2 + \phi_{2,y}^4 + 4\phi_{1,y}^2\phi_{2,x}^2} \right) \right]\,, \tag{9.46}$$

where, for instance, $\phi_{1,x}$ represents the partial derivative of the first component of ϕ with respect to x. For further notational convenience, it will be helpful to denote partial differentiation of σ using subscripts also, so that

$$\sigma_{xxy} := \frac{\partial^3 \sigma}{\partial x^2 \partial y}\,, \tag{9.47}$$

for example.

LCS are defined as the ridges in the scalar field $\sigma(\mathbf{x}, t)$. To mathematically define "ridges", we will need to compute both the gradient of $\sigma(\mathbf{x}, t)$:

$$\nabla\sigma(\mathbf{x}, t) := \begin{bmatrix} \sigma_x \\ \sigma_y \end{bmatrix} , \tag{9.48}$$

and the Hessian:

$$\Sigma(\mathbf{x}, t) := \begin{bmatrix} \sigma_{xx} & \sigma_{xy} \\ \sigma_{xy} & \sigma_{yy} \end{bmatrix} . \tag{9.49}$$

The Hessian, $\Sigma(\mathbf{x}, t)$, has a minimum eigenvalue:

$$\lambda_{\mathbf{n}}(\mathbf{x}, t) = \lambda_{\min}\left[\Sigma(\mathbf{x}, t)\right] = \frac{1}{2}\left(\sigma_{xx} + \sigma_{yy} - \sqrt{\sigma_{xx}^2 - 2\sigma_{xx}\sigma_{yy} + \sigma_{yy}^2 + 4\sigma_{xy}^2}\right) , \tag{9.50}$$

with a corresponding eigenvector

$$\mathbf{n}(\mathbf{x}, t) = \begin{bmatrix} \sigma_{xx} - \sigma_{yy} - \sqrt{\sigma_{xx}^2 - 2\sigma_{xx}\sigma_{yy} + \sigma_{yy}^2 + 4\sigma_{xy}^2} \\ 2\sigma_{xy} \end{bmatrix} . \tag{9.51}$$

With these definitions of $\mathbf{n}$ and $\lambda_{\mathbf{n}}$ in hand, we can now define a point on the LCS as any point $\mathbf{x}_{LCS}$, for which the following two conditions are satisfied:

$$\nabla\sigma(\mathbf{x}_{LCS}, t) \cdot \mathbf{n}(\mathbf{x}_{LCS}, t) = 0 , \quad \text{and} \quad \lambda_{\mathbf{n}}(\mathbf{x}_{LCS}, t) < 0 . \tag{9.52}$$

These two conditions ensure that the point $\mathbf{x}_{LCS}$ lies on a ridge in the scalar field σ. At such a point, the eigenvector, $\mathbf{n}$, has the property that it is a vector normal to the LCS.

The evolution of the LCS is determined by finding precisely the motion that preserves the LCS condition:

$$\frac{d}{dt}\left[\nabla\sigma(\mathbf{x}_{LCS}, t) \cdot \mathbf{n}(\mathbf{x}_{LCS}, t)\right] = 0 . \tag{9.53}$$

Condition (9.53) is a single scalar equation for the two unknown components of $\dot{\mathbf{x}}_{LCS} = [\dot{x}_{LCS}, \dot{y}_{LCS}]$. In order to solve for $\dot{x}_{LCS}$ and $\dot{y}_{LCS}$, we must introduce a second condition. We choose to impose the condition that points on the LCS move only in a direction orthogonal to the LCS.[4] This is ensured by

$$\nabla\sigma \cdot \dot{\mathbf{x}}_{LCS} = 0\,. \tag{9.55}$$

Together, conditions (9.53) and (9.55) allow us to solve for the motion of the LCS. As before, we must always ensure that the minimum eigenvalue, $\lambda_{\mathbf{n}}$, remains negative during the evolution.

Expanding the derivative of condition (9.53) yields

$$\frac{\partial}{\partial t}\left(\nabla\sigma \cdot \mathbf{n}\right) + \dot{\mathbf{x}}_{LCS} \cdot \left(\Sigma\,\mathbf{n}\right) + \dot{\mathbf{x}}_{LCS} \cdot \left([\mathrm{D}\mathbf{n}]'\,\nabla\sigma\right) = 0\,.$$

Before solving for the components of $\dot{\mathbf{x}}_{LCS}$, we introduce one further simplification. Recall that $\mathbf{n}$ is an eigenvector of Σ corresponding to the eigenvalue $\lambda_{\mathbf{n}}$. Thus,

$$\frac{\partial}{\partial t}\left(\nabla\sigma \cdot \mathbf{n}\right) + \lambda_{\mathbf{n}}\left(\dot{\mathbf{x}}_{LCS} \cdot \mathbf{n}\right) + \dot{\mathbf{x}}_{LCS} \cdot \left([\mathrm{D}\mathbf{n}]'\,\nabla\sigma\right) = 0\,.$$

Finally, solving for the velocity of the LCS that satisfies the constraints yields

$$\dot{x}_{LCS} = \sigma_y \frac{A}{B} \tag{9.56}$$

$$\dot{y}_{LCS} = -\sigma_x \frac{A}{B}\,, \tag{9.57}$$

[4] An alternative condition is that the velocity of a point on the LCS, in the direction tangential to the LCS, is equal to the tangential velocity of the underlying velocity field:

$$\nabla\sigma \cdot \dot{\mathbf{x}}_{LCS} = \nabla\sigma \cdot \mathbf{f}\,, \tag{9.54}$$

which yields a slightly different result.

where

$$A := \frac{\partial}{\partial t}\left(\nabla\sigma \cdot \mathbf{n}\right) , \tag{9.58}$$

$$B := \sigma_x(\lambda_{\mathbf{n}} n_2 + \sigma_x n_{1,y} + \sigma_y n_{2,y}) - \sigma_y(\lambda_{\mathbf{n}} n_1 + \sigma_x n_{1,x} + \sigma_y n_{2,x}) . \tag{9.59}$$

Recall that all the terms in this expression are defined in terms of σ and its derivatives. In turn, equation (9.46) provides an expression for σ in terms of the flow map ϕ. The end result is that we can write an expression of the form

$$\dot{\mathbf{x}}_{LCS} = F[\phi] , \tag{9.60}$$

where F is a known function of ϕ and its partial derivatives.

Finally, the values of these partial derivatives can be computed using the variational equations as described for the case of one-dimensional flow, yielding evolution equations of motion for points on the LCS that can, in principle, be computed *a priori* from the underlying velocity field $\mathbf{f}(\mathbf{x}, t)$. Some of the terms in these equations simplify because we can impose the condition that the terms are evaluated on the LCS. Even so, it is bitterly clear at this point that the number of terms has become unwieldy, and we must resort to computer algebra or approximations before proceeding further.

This situation is not without parallel. The study of sensitivity analysis of ODE and DAE systems results in similar sets of equations. One potentially promising step forward on the numerical front is the possible incorporation of automatic differentiation methods developed by Barrio that are based on Taylor Series approximations, and are designed expressly for problems of this type [Barrio 2006].

Chapter 10

Numerical Considerations

The FTLE calculations presented in this thesis were computed using recently developed research software, called `Newman`. One of the the most important contributions of the new software is that the calculations can be performed in parallel, thus dramatically decreasing computation times. As an example, calculations of the FTLE for the global ocean at a grid resolution of 4096×4096 that would require days to compute with first-generation single processor codes, can now be computed in minutes on a parallel cluster. A further advantage of the new software is that it can be compiled for computations in flows of any dimension, whereas previous codes were restricted to two-dimensional flows.

10.1 FTLE Computation

The core algorithm for computing the FTLE follows that of [Lekien 2003], and involves approximating the flow map by integrating trajectories from a uniform grid of initial conditions. The derivatives of the flow map needed in the definition of the FTLE are then obtained by finite differencing the approximate flow map. In principle, the numerical algorithm is very simple, and the pseudo-code barely fills a hand-written page; however, the software can become somewhat complex (a few thousand lines of code) in order to cover all possible contingencies. These include memory constraints, velocity data provided on non-uniform grids or nested grids, arbitrarily shaped domains including domains with islands, varying input and output formats,

choices of integration schemes, integration in Cartesian space or on the sphere, etc.

By far the most computationally expensive part of the algorithm is integration of individual drifter trajectories. As mentioned, this task can be trivially parallelized, thus reducing the computation time. Although not pursued as part of this thesis, opportunities still remain to design a more efficient algorithm beyond straightforward parallelization. Possibilities include adaptive refinement of the grid of initial conditions in regions that track the LCS, as well as reusing results of drifter integrations from previous time frames to inform integration of drifters in the current frame. Further ideas include using the evolution equations for the LCS to numerically track the motion of the LCS, or approximating the motion of the LCS using flux minimizing curves.

10.2 Features of the `Newman` Software

`Newman` was specifically designed for large-scale parallel computations of geophysical flows. In particular it contains the following features:

1. **N-Dimensional Code:** The underlying code in `Newman` is dimension independent. When the code is compiled, a user-supplied flag indicates the desired dimensionality. In this way, the code is more easily maintained, and no sacrifice in efficiency is required.

2. **Parallel Implementation:** The code is written using the Message Passing Interface for use on either a single processor or a parallel cluster. Currently, parallel computations are performed routinely on several hundreds of processors in the Geophysical and Planetary Sciences supercluster at Caltech.

3. **Fast and Modular C++ Structures:** `Newman` is written in C++ to ensure computational speed and modularity of code. Users can easily implement their own additions to the code by editing or replacing individual modules.

4. **Light-Weight Data Structures:** `Newman` can handle large data sets and high-resolution computations through efficient memory usage. All input and output

are performed in binary format for fastest retrieval over the internet.

5. **Geophysical Applications:** `Newman` has many features specifically intended for geophysical applications. These include the ability to compute and plot FTLE on the sphere in 2D and 3D, or on a Mercator longitude-latitude-altitude projection; track the center of a tropical storm so that FTLE may be computed in storm-centered coordinates; use velocity data computed on multiple moving nested grids as is common for hurricane simulations; and interpolate data provided on non-uniform Cartesian grids.

6. **Fast Treatment of Boundaries:** `Newman` can quickly integrate trajectories for flows with arbitrarily shaped boundaries and multiple islands and appropriately compute the FTLE.

7. **Library of Integration Algorithms:** `Newman` uses the GNU Scientific Library for integration of trajectories and linear algebra calculations. The user can choose from several different integration schemes available.

8. **Miscellaneous Features:** `Newman` allows the user to produce plots of the FTLE, drifter trajectories, and velocity fields both forward and backward in time at a temporal resolution that is independent of the temporal spacing between frames in the data set. Data sets can be specified as periodic along any spatial dimension and in time.

`Newman` is freely available for download over the internet at www.cds.caltech.edu:∼/pdutoit/software. A manual that describes installation, including all the parameters the user may select, is provided in Appendix A.

Chapter 11

Conclusion

In his study of planetary motion and celestial mechanics, Poincaré was the first to discover the geometric structure of the homoclinic tangle. Others, such as Cartwright, Littlewood, and Levinson, saw the effects of the tangle exhibited in the bizarre behavior of trajectories for periodically forced electric circuits. Later, Smale would abstract the action of the tangle and fully come to terms with the implications of chaotic trajectories.

This thesis adds infinitesimally to these works, by providing evidence for the persistence of the homoclinic tangle in *aperiodic* flows – a realm where Poincaré's theory is not directly applicable. Indeed, the action of horseshoes has been shown to arise not just in an abstract manner on the beaches of Rio [Smale 1998], but in a very real way in the waters a few miles offshore, and in the swirling atmosphere above. The approach that allows for visualization of the homoclinic tangle in aperiodic flows is the FTLE-LCS method.

In hurricanes, we have seen that the FTLE-LCS recovers the relevant Lagrangian boundary to a storm – a boundary that cannot be perceived from plots of velocity or vorticity alone. Moreover, the mechanism that governs transport of airmass across this boundary is lobe dynamics, the process of tranporting regions of the flow that necessarily attends the action of a homoclinic tangle.

In the turbulent flows of the global ocean, the FTLE-LCS approach provides a mental picture of how mesoscale eddies are responsible for inducing mixing and stirring. The LCS reveals the boundaries to eddies, and their mutual interaction, in a

time-dependent manner that underscores the importance of eddies and lobe structures for lateral mixing in the ocean.

The method has been applied further in a model for bio-molecules. Computation of the LCS for aperiodic flow in a reduced order model that faithfully captures the statistics of the full system reveals that the transport mechanism that governs global conformation change is again the homoclinic tangle.

Further applications of the method include coastal ocean flows, the atmosphere of Titan, storms on Netpune, laboratory flows, persistent eddies in the North Atlantic, and celestial mechanics. In each case, the LCS provides interesting insight into the the important separatrices that dictate transport, and encode Lagrangian information that cannot be discerned from Eulerian fields.

Beyond the applications, we have addressed some important theoretical underpinnings of the LCS method. We have discovered that the FTLE-LCS are neither invariant, nor are they generalizations of stable and unstable manifolds, yet they optimally shed as little invariance as needed in order to track the most important features in the flow. An algorithm has been presented which allows for the derivation of explicit evolution equations for the LCS, which the author hopes will spur further progress in the theory of the FTLE-LCS method.

Future applications of FTLE-LCS appear to be as wide and varied as there are flows, and there are many avenues in which to proceed. Immediate research goals that follow from this thesis, include:

- A continued study of the theoretical underpinnings of FTLE-LCS using the initial results provided here as a starting point. What are the key properties that can be shown for LCS defined as ridges in the FTLE?

- Development of regionally specific mesoscale eddy parameterizations for use in global ocean models based on the insights learned from LCS. Can LCS provide a parametrization that improves upon the diffusion and random-walk parametrizations currently employed?

- Incorporating FTLE-LCS calculations to guide real-time deployment of sensory

drifters in ocean and hurricane experiments. An experiment to this effect is planned for Prince William Sound, Alaska in July and August, 2009. An ideal situation will be to compute the FTLE-LCS in realtime using ocean model velocity data, identify homoclinic dynamics in the flow, and seed the corresponding lobes in the Sound with drifters in order to verify the presence of horseshoe dynamics.

Appendix A

Newman - Software for Computing FTLE in Geophysical Applications

`Newman` is software to compute the FTLE for time-dependent velocity fields. The velocity field is provided either as an analytical expression, or as a numerical data set. The computations can be performed on parallel processors or on a single processor.

A.1 Installation

`Newman` source code can be compiled using the make command. To install `Newman` you will need to complete the following three steps:

1. Install the MPI library,
2. Install the GSL library,
3. Make Newman,

The MPI and GSL libraries must be installed before `Newman` can be compiled.

A.1.1 MPI

`Newman` is designed for industrial strength computations in parallel. Computations can be run on a single processor; however, MPI must still be installed. Visit `http:`

//www.open-mpi.org to find instructions for downloading and installing the MPI library.

A.1.2 GSL

Newman uses the integration and eigensystem routines in the GNU Scientific Library. Visit http://www.gnu.org/software/gsl/ to find instructions for downloading and installing the GSL library. Newman requires version GSL 1.10 or greater. To determine which version of GSL you currently have and where it is installed, simply execute the gsl-config command.

A.1.3 Make Newman

The Newman source code resides in the ./src directory. A shell script is provided that will attempt to compile Newman in two, three, and four dimensions. Make sure that the permissions on the script ./makenewman.sh are set to executable, and then run the script:

>./makenewman.sh

This will attempt to generate three executable files: newman2D, newman3D, and newman4D in the ./src directory.
If there are errors in compilation, or if you would like to customize the installation, you may need to edit the makefiles. The makefiles can be found in the ./src directory. The most common error encountered when compiling is ensuring that the linker can find the needed libraries.

A.2 Running Newman

To run Newman from the commandline, type

>newman2D saturn.in

where saturn.in is a text input file containing parameter values for your computation. Be sure that the executable is in a directory in your path.

See the Examples directory for an example of an input file. A description of each of the parameters and their default values is provided in section A.4.

A.3 Viewing the Results

`Newman` outputs all results in a lightweight binary format. Separate code modules are then used to convert the raw binary format into the final desired format. This allows for:

- fast retrieval of results from a cluster over the internet,
- easier writing of modules for data conversion to the final desired format required by the user.

A.3.1 Tecplot Format

The `raw2tec` modules are provided to convert the raw binary output from `Newman` to Tecplot binary format. Tecplot is commercial plotting software. To compile the raw2tec modules, run the makeraw2tec.sh shell script.

>./makeraw2tec.sh

This script will attempt to compile raw2tec2D, raw2tec3D, and raw2tec4D in the ./raw2tec directory. The first step executed by the script will be to compile the tecio.a library in the ./lib/tecio/ directory. The tecio.a library is written by the Tecplot company. As the compilation proceeds, you will be requested to select your platform. I have found that selecting linux.22 as the platform works well on Unix and Mac platforms. Next, when directed, select the option: "1. Make tecio.a only". The

script should then proceed uninterrupted to the finish. The raw2tec executables will be in the ./raw2tec directory.

To learn more about these modules, type

>raw2tec2D -h

at the commandline.

The binary data can be formatted for plotting in Cartesian coordinates or on the sphere for geophysical applications. Use the `-s` flag to convert from spherical coordinates to cartesian for plotting on the sphere.

For 3D data on the sphere, use the `-a` option to provide the scale factor by which to scale the atmosphere with respect to its true size. For example, `-a 20.0` will scale the atmosphere by a factor of 20.0 relative to the sphere radius.

A.3.2 Matlab Format

In the ./scripts directory, you will find the raw2mat.m Matlab script. This script allows for conversion of the raw binary output to Matlab form. The Matlab conversion script raw2mat is not as well supported as the Tecplot conversion module raw2tec. Many of the features available in raw2tec still need to be included in the raw2mat.m script.

A.4 Parameters

Atmos_Radius

Values: double

Default: 6378.1

Description: Atmos_Radius is the radius of the sphere to be used for integration on the sphere.

Atmos_Set

Values: [0 | 1]

Default: 0

Description: Atmos_Set is a switch to turn on/off integration on the sphere using Longitude and Latitude coordinates.

Boundary_InFile

Values: char*

Default: boundary.dat

Description: Boundary_InFile is the name of the file containing the list of polygon segments to be used for the boundary.

Boundary_Method

Values: [0 | 1 | 2]

Default: 0

Description: Boundary_Method determines the type of boundary checking that will be used according to the following table:

0 No enforcement of boundaries.

1 Regions outside the boundary are defined as those for which the velocity data cell contains a value that is NaN.

2 The boundary is explicitly provided as a list of polygon segments. 3 An analytical expression hard-wired into the code is evaluated to determine the boundary.

Data_Format

Values: [0 | 1 | 2]

Default: 2

Description: Data_Format determines the format of the numerical velocity data according to the following table:

0 Raw binary data

1 Tecplot ASCII data

2 ASCII lean velocity data

Data_InFile

Values: char*

Default: velocitydata

Description: Base name of the files containing the numerical velocity data.

Data_Max[ND]

Values: double

Default: 1.0

Description: Data_Max[ND] is the maximum value of grid locations in the numerical velocity data.

Data_Min[ND]

Values: double

Default: 0.0

Description: Data_Min[ND] is the minimum value of grid locations in the numerical velocity data.

Data_NonUniformGridND]

Values: [0 | 1]

Default: 0

Description: Data_NonUniformGrid[ND] is a switch to turn on/off the use of a non-uniform grid for the locations of numerical velocity data along the given dimension.

Data_NumInputFiles

Values: int

Default: 2

Description: Number of input files containing the numerical velocity data.

Data_Periodic[ND]

Values: [0 | 1]

Default: 0

Description: Data_Periodic[ND] is a switch to turn on/off periodicity of the data along the given spatial dimension.

Data_Res[ND]

Values: int

Default: 2

Description: Data_Res[ND] is the number of grid locations in the numerical velocity data.

Data_TDelta

Values: double

Default: 1.0

Description: Data_TDelta[ND] is the time interval between time slices in the numerical velocity data.

Data_TMin

Values: double

Default: 0.0

Description:

Data_TPeriodic

Values: [0 | 1]

Default: 0

Description: Data_TPeriodic is a switch to turn on/off time periodicity in the numerical velocity data.

Data_TRes

Values: int

Default: 2

Description: Data_TRes is the number of time slices in the numerical velocity data.

Filter_Width

Values: double

Default: 0.0

Description: FTLE_Width is the width of the gaussian filter to be used in post process smoothing of the FTLE.

FTLE_Compute

Values: [0 | 1]

Default: 1

Description: A switch to turn on/off computation of the Finite Time Liapunov Exponent field.

FTLE_IntTLength

Values: double

Default: 1.0

Description: FTLE_IntTLength is the integration time to be used in the definition of the FTLE.

FTLE_Max[ND]

Values: double

Default: 1.0

Description: FTLE_Max[ND] is the maximum grid location for computation of the FTLE.

FTLE_Min[ND]

Values: double

Default: 0.0

Description: FTLE_Min[ND] is the minimum grid location for computation of the FTLE.

FTLE_OutFile

Values: char*

Default: repatt

Description: FTLE_Outfile is the base name of the output file for FTLE data.

FTLE_Res[ND]

Values: int

Default: 3

Description: FTLE_ResND] is the number of grid locations for computation of the FTLE.

FTLE_TrackWidth[ND]

Values: double

Default: 1.0

Description: FTLE_TrackWidth[ND] is the width of the grid for computation of the FTLE centered about the storm center when the Track_Storm option is used.

Int_AbsTol

Values: double

Default: 1e-5

Description: Int_AbsTol is the tolerance threshold for the absolute error for an adaptive step size integrator.

Int_MaxTimeStep

Values: double

Default: 1.0

Description: Int_MaxTimeStep is the maximum allowed timestep for the RK45 integrator with adaptive step-sizing and step-size thresholds. The algorithm attempts to choose the largest step size between Int_MinTimeStep and Int_MaxTimeStep such that the error tolerances are satisfied.

Int_Method

Values: [0 | 1 | 2 | 3]

Default: 0

Description: Int_Method determines the type of integrator used to integrate trajectories according to the following table:

0 Adaptive step size integrator with strict error tolerances

1 Fixed step size integrator

2 Euler integrator

3 RK45 integrator with adaptive step-sizing and step-size thresholds.

Int_MinTimeStep

Values: double

Default: 0.1

Description: Int_MinTimeStep is the minimum allowed timestep for the RK45 integrator with adaptive step-sizing and step-size thresholds. The algorithm attempts to choose the largest step size between Int_MinTimeStep and Int_MaxTimeStep such that the error tolerances are satisfied.

Int_RelTol

Values: double

Default: 1e-6

Description: Int_RelTol is the tolerance threshold for the relative error for an adaptive step size integrator.

Int_TimeStep

Values: double

Default: 1.0

Description: Int_TimeStep is the size of the timestep for a fixed step size integrator.

MapCoord

Values: [0 | 1]

Default: 0

Description: A switch to turn on/off mapping of points to an integration space before integration of trajectories. This is convenient if the FTLE is to be plotted in a space that is different form the space in which the trajectories are to be integrated.

Nest_NumNests

Values: int

Default: 0

Description: Nest_NumNests is the number of total nests available for nested velocity grids.

Nest_List

Values: { int }

Default: 0

Description: Nest_List is an ordered list specifying which of the nested velocity sets should be used for the computation. Elements in the list can be any integer from 0 to Nest_NumNests-1 inclusive.

Output_TDelta

Values: double

Default: 1.0

Description: Output_TDelta is the desired time interval between frames of output data.

Output_TRes

Values: int

Default: 2

Description: Output_TRes is the desired number of frames of output data.

Output_T1

Values double

Default: 0.0

Description: Output_T1 is the desired time of the first frame of output data.

Parallel_LoadRatio

Values double

Default: 1.0

Description: Parallel_LoadRatio is the factor by which the number of jobs to be assigned is larger than the number of processors available. Choosing a larger ratio can help to improve load balancing among the nodes at the expense of a nominal overhead.

Parameters_Print

Values: [0 | 1]

Default: 1

Description: A switch to turn on/off printing of all parameter values to the screen.

Path_Input

Values: char*

Default: Input

Description: Path_Input is the directory in which all input files can be found.

Path_Output

Values: char*

Default: Output

Description: Path_Output is the directory where all output data generated will be placed.

Path_Work

Values: char*

Default: Work

Description: Path_Work is a directory where temporary working files used by the Master node during the computation will be placed.

Path_Scratch

Values: char*

Default: /tmp

Description: Path_Work is a directory where temporary working files used by the slave nodes during the computation will be placed. This should be a directory local to the node to avoid unnecessary transfer of files.

Plot_Max[ND]

Values: double

Default: 1.0

Description: Plot_Max[ND] is the maximum grid location for plotting of the velocity.

Plot_Min[ND]

Values: double

Default: 0.0

Description: Plot_Max[ND] is the minimum grid location for plotting of the velocity.

Plot_OutFile

Values: char*

Default: velocityplot.dat

Description: Plot_OutFile is the name of the file where the plotted velocity output data will be placed.

Plot_Res[ND]

Values: int

Default: 2

Description: Plot_ResND] is the number of grid locations for plotting of the velocity.

Plot_Velocity

Values: [0 | 1]

Default: 0

Description: A switch to turn on/off output of the velocity field for velocity data.

Query_Velocity

Values: [0 | 1]

Default: 0

Description: A switch to turn on/off querying of the velocity data at a specified point.

Query_X[ND]

Values: double

Default: 0.0

Description: Query_X[ND] are the coordinates at which the velocity will be queried and printed to the screen.

Time_Direction

Values: [-1 | 1]

Default: 1

Description: For Plot_Velocity and Trace computations, Time_Direction determines the direction of time in the output data. For FTLE_Compute, Time_Direction determines the direction of itegration of trajectories.

Time_Origin

Values: 6 int

Default: 0 0 0 0 0 0

Description: Time_Origin contains an array of six integers representing the time and date that correspond to time zero in the data. The integers represent: Year Month Day Hour Minute Second. Specifying the time origin allows the raw2tec utilities to time and datestamp the output for plotting purposes.

Trace_ColorDimension

Values: int

Default: 0

Description: Trace_ColorDimension is the dimension that will be used to color drifters according to their initial position.

Trace_Compute

Values: [0 | 1]

Default: 0

Description: A switch to turn on/off computation of passive drifter trajectories.

Trace_GenerateMesh

Values: [0 | 1]

Default: 0

Description: Trace_GenerateMesh is a switch to turn on/off the generation of a grid of initial locations for drifter trajectories.

Trace_InFile

Values: char*

Default: drifterinput.dat

Description: Trace_InFile is the name of the input file containing initial locations of drifters.

Trace_MeshColor

Values: double

Default: 0.0

Description: Trace_MeshColor is the color to be assigned to the grid of generated drifters.

Trace_MeshMax[ND]

Values: double

Default: 1.0

Description: Trace_MeshMax[ND] is the maximum grid location for initial positions of drifters.

Trace_MeshMin[ND]

Values: double

Default: 0.0

Description: Trace_MeshMin[ND] is the minimum grid location for initial positions of drifters.

Trace_MeshReleaseTime

Values: double

Default: 0.0

Description: Trace_MeshReleaseTime is the time at which the grid of drifters will be released in the flow.

Trace_MeshRes[ND]

Values: int

Default: 2

Description: Trace_MeshRes[ND] is the number of grid locations for initial positions of drifters.

Trace_OutFile

Values: char*

Default: drifteroutput.dat

Description: Trace_OutFile is the name of the output file containing drifter trajectories.

Track_InFile

Values: char*

Default: track.dat

Description: Track_File is the name of the file containing the coordinates of the track to be used for computation of FTLE for moving grids.

Track_Storm

Values: [0 | 1]

Default: 0

Description: Track_Storm is a switch to turn on/off computation of FTLE in storm centered coordinates.

V[ND]

Values: char*

Default: x

Description: List of analytical equations for the velocity field.

Velocity_Format

Values: [0 | 1 | 2]

Default: 0

Description: Velocity_Format determines the type of velocity to be used during the computation according to the following table:

0 Equations for velocity hard wired into the code at compile time in the velocity.cpp file. 1 Equations specified by the user at run time using the equation parser. 2 Velocity is to be determined from a numerical data set.

Velocity_Null[ND]

Values: [0 | 1]

Default: 0

Description: Velocity_Null[ND] is a switch to turn on/off the zeroing of the velocity along the specified dimension.

Bibliography

[Armi 1989] L. Armi, D. Hebert, N. Oakey, J. F. Price, P. L. Richardson, H. T. Rossby, and B. Ruddick, Two Years in the Life of a Mediterranean Salt Lens, Journal of Physical Oceanography, 19(3), 354–370 (1989).

[Arnold 1978] Arnold, V. I. (1978). Mathematical Methods of Classical Dynamics. Springer-Verlag.

[Aurell 1997] E. Aurell, G. Boffetta, A. Crisanti, G. Paladin, and A. Vulpiani, Predictability in the large: an extension of the concept of Lyapunov exponent, Journal of Physics A: Mathematical and General, 30(1), 1-26 (1997).

[Barrio 2006] R. Barrio, Sensitivity Analysis of ODES/DAES Using the Taylor Series Method, SIAM J. Sci. Comput., 27(6), 1929–1947 (2006).

[Barrow-Green 1996] Barrow-Green, J. (1996). Poincaré and the Three Body Problem. American Mathematical Society.

[Beigie 1991] D. Beigie, A. Leonard, and S. Wiggins, Chaotic transport in the homoclinic and heteroclinic tangle regions of quasiperiodically forced two-dimensional dynamical systems, Nonlinearity, 4(3), 775–819 (1991).

[Bhattacharjee 2000] S. M. Bhattacharjee, Unzipping DNAs: towards the first step of replication, Journal of Physics A: Mathematical and General, 33(45), L423-L428 (2000).

[Booker 1999] A. J. Booker, J. E. Dennis, P. D. Frank, D. B. Serafini, V. Torczon, and M. W. Trosset, A rigorous framework for optimization of expensive functions by surrogates, Structural and Multidisciplinary Optimization, 17(1), 1–13 (1999).

[Brunger 1984] A. Brunger, C. L. Brooks, and M. Karplus, Stochastic boundary conditions for molecular dynamics simulations of ST2 water, Chemical Physics Letters, 105(5), 495–500 (1984).

[Bryan 2008] F. O. Bryan, Introduction: Ocean modeling – eddy or not, appearing in *Ocean modeling in an eddying regime* M. Hecht, H. Hasumi, (eds.) American Geophysical Union, 1-3 (2008).

[Campbell 2005] D. K. Campbell, P. Rosenau, and G. M. Zaslavsky, Introduction: The Fermi–Pasta–Ulam problem—The first fifty years, Chaos: An Interdisciplinary Journal of Nonlinear Science, 15(1), 015101 (2005).

[Cartwright 1945] M. L. Cartwright and J. E. Littlewood, On Non-Linear Differential Equations of the Second Order: I. the Equation Formula - k(1-y2)Formula + y = b{lambda}k cos({lambda}l + {alpha}), k Large, Journal of the London Mathematical Society, s1-20(3), 180–189 (1945/6/1).

[Causo 2000] M. S. Causo, B. Coluzzi, and P. Grassberger, Simple model for the DNA denaturation transition, Phys. Rev. E, 62(3), 3958–3973 (2000).

[Chandrasekhar 1969] Chandrasekhar, S. (1969). Ellipsoidal Figures of Equilibrium. Dover.

[Chelton 2007] D. B. Chelton, M. G. Schlax, R. M. Samelson, and R. A. de Szoeke, Global observations of large oceanic eddies, Geophys. Res. Lett., 34 (2007).

[Chen 2007] Chen, S. S., J. F. Price, W. Zhao, M. A. Donelan, and E. J. Walsh [2007], The CBLAST-Hurricane Program and the next-generation fully coupled atmosphere-wave-ocean models for hurricane research and prediction. *Bull. Amer. Meteor. Soc*, **88**, 311–317.

[Chertock 2009] A. Chertock, P. Du Toit, and J. Marsden, A particle method for the EPdiff equation, Article in preparation.

[Cocco 1999] S. Cocco and R. Monasson, Statistical Mechanics of Torque Induced Denaturation of DNA, Physics Review Letters, 83, 5178–5181 (1999).

[Dauxois 1993] T. Dauxois, M. Peyrard, and A. R. Bishop, Entropy-driven DNA denaturation, Phys. Rev. E, 47(1), R44–R47 (1993).

[Dauxois 2008] T. Dauxois, Fermi, Pasta, Ulam and a mysterious lady, PHYSICS TODAY, 61, 55 (2008).

[d'Ovidio 2004] F. d'Ovidio, V. Fernández, E. Hernández-Garca, and C. López, Mixing structures in the Mediterranean Sea from finite-size Lyapunov exponents, Geophys. Res. Lett., 31 (2004).

[Drevillon 2008] M. Drvillon, The GODAE/Mercator-Ocean global ocean forecasting system: results, applications and prospects, Journal of Operational Oceanography, 1(1), 51-57 (2008).

[Du Toit 2009a] P. Du Toit, I. Mezic, and J. Marsden, Coupled oscillator models with no scale separation, Physica D: Nonlinear Phenomena, 238(5), 490-501 (2009).

[Du Toit 2009b] P. Du Toit, K. Grubits, S. Costiner, and J.E. Marsden, Fast generation of potentials for self-assembly, Submitted.

[Du Toit 2009c] P. Du Toit, M. Kabilarov, S. Nair, and J. Marsden, A framework for search with under-actuated vehicles and uncertain sensors, In preparation.

[Emanuel 2001] K. Emanuel, Contribution of tropical cyclones to meridional heat transport by the oceans, J. Geophys. Res., 106 (2001).

[Emanuel 2007] K. Emanuel, Environmental Factors Affecting Tropical Cyclone Power Dissipation, Journal of Climate, 20(22), 5497–5509 (2007).

[Ercolani 1990] N. Ercolani, M. G. Forest, D. W. McLaughlin, Geometry of the modulational instability III. Homoclinic orbits for the periodic sine-Gordon equation, Physica D Nonlinear Phenomena 43 (1990) 349-84

[Fermi 1955] E. Fermi, J. Pasta, and S. Ulam, Studies of Nonlinear Problems. I, Los Alamos Report, (LA-1940) (1955).

[Forest 1992] M. G. Forest, C. G. Goedde, A. Sinha, Instability-driven energy transport in near-integrable, many degrees-of-freedom, Hamiltonian systems, Physical Review Letters 68 (1992) 2722-5.

[Fox-Kemper 2008] B. Fox-Kemper and D. Menemenlis, Can large eddy simluation techniques improve mesoscale rich ocean models?, appearing in *Ocean modeling in an eddying regime* M. Hecht, H. Hasumi, (eds.) American Geophysical Union, 319-337 (2008).

[Franco 2007] E. Franco, D. Pekarek, J. Peng, and J. Dabiri, Geometry of unsteady fluid transport during fluid-structure interactions, Journal of Fluid Mechanics, 589(-1), 125-145 (2007).

[Gawlik 2009] E. Gawlik, J. Marsden, P. Du Toit, and S. Campagnola, Lagrangian coherent structures in the planar elliptic restricted three-body problem, Celestial Mechanics and Dynamical Astronomy, 103(3), 227–249 (2009/03/01/).

[Gent 1990] P. R. Gent and J. C. Mcwilliams, Isopycnal Mixing in Ocean Circulation Models, Journal of Physical Oceanography, 20(1), 150–155 (1990).

[Guckenheimer 1983] J. Guckenheimer and P. Holmes. (1983). Nonlinear Oscillations, Dynamical Systems, and Bifurcations of Vector Fields. Springer.

[Haller 2000] G. Haller and G. Yuan, Lagrangian coherent structures and mixing in two-dimensional turbulence, Physica D: Nonlinear Phenomena, 147(3-4), 352–370 (2000).

[Haller 2001] G. Haller, Distinguished material surfaces and coherent structures in three-dimensional fluid flows, Physica D: Nonlinear Phenomena, 149(4), 248–277 (2001).

[Haller 2002] G. Haller, Lagrangian coherent structures from approximate velocity data, Physics of Fluids, 14(6), 1851–1861 (2002).

[Hecht 2008a] M. W. Hecht, D. D. Holm, M. R. Petersen, and B. A. Wingate, The LANS-α and Leray turbulence parameterizations in primitive equation ocean modeling, Journal of Physics A: Mathematical and Theoretical, 41(34), 344009 (23pp) (2008).

[Hecht 2008b] M. W. Hecht, D. D. Holm, M. R. Petersen, and B. A. Wingate, Implementation of the LANS-α turbulence model in a primitive equation ocean model, Journal of Computational Physics, 227, 5691-5716 (2008).

[Hill 1894] M. J. M. Hill, On a Spherical Vortex, Philosophical Transactions of the Royal Society of London. A, 185, 213–245 (1894).

[Holm 2005] D. Holm and J. Marsden, Momentum maps and measure-valued solutions (peakons, filaments, and sheets) for the EPDiff equation, The Breadth of Symplectic and Poisson Geometry, , 203–235 (2005).

[Holmes 1990] P. Holmes, Poincaré, Celestial Mechanics, Dynamical-Systems Theory, and Chaos, Physics Reports, 193(3), 137-163 (1990).

[Houze 2007] J. Houze, Robert A., S. S. Chen, B. F. Smull, W. Lee, and M. M. Bell, Hurricane Intensity and Eyewall Replacement, Science, 315(5816), 1235–1239 (2007).

[Ide 2002] K. Ide, D. Small, and S. Wiggins, Distinguished hyperbolic trajectories in time-dependent fluid flows: analytical and computational approach for velocity fields defined as data sets, Nonlinear Processes in Geophysics, 9(3/4), 237–263 (2002).

[Kafri 2002] Y. Kafri, D. Mukamel, and L. Peliti, Melting and unzipping of DNA, European Physical Journal B, 27, 135 (2002).

[Kida 1981] S. Kida, Motion of an elliptic vortex in a uniform shear flow, Journal of the Physical Society of Japan, 50, 3517-3520 (1981).

[Kirchhoff 1876] G. R. Kirchhoff. *Vorlesungen uber Matematische Physik*, Vol. I, Teubner, Leipzig, 1876.

[Koon 2000] W. S. Koon, M. W. Lo, J. E. Marsden, and S. D. Ross, Heteroclinic connections between periodic orbits and resonance transitions in celestial mechanics, Chaos: An Interdisciplinary Journal of Nonlinear Science, 10(2), 427-469 (2000).

[Kuo 2003] Kuo, B., et al. Hurricane Isabel data produced by the Weather Research and Forecast (WRF) model, courtesy of NCAR, and the U.S. National Science Foundation (NSF).

[Lamb 1945] Lamb, H. (1945). Hydrodynamics. Dover Publications.

[Lekien 2003] F. Lekien, Time-Dependent Dynamical Systems and Geophysical Flows, PhD Thesis, (2003).

[Lekien 2005] F. Lekien, C. Coulliette, A. J. Mariano, E. H. Ryan, L. K. Shay, G. Haller, and J. Marsden, Pollution release tied to invariant manifolds: A case study for the coast of Florida, Physica D: Nonlinear Phenomena, 210(1-2), 1–20 (2005).

[Lekien 2007] F. Lekien, S. C. Shadden, and J. E. Marsden, Lagrangian coherent structures in n-dimensional systems, Journal of Mathematical Physics, 48(6), 065404 (2007).

[Levinson 1949] N. Levinson, A Second Order Differential Equation with Singular Solutions, The Annals of Mathematics, 50(1), 127–153 (1949).

[Li 2008] Z. Li, Y. Chao, J. C. McWilliams, and K. Ide, A three-dimensional variational data assimilation scheme for the Regional Ocean Modeling System: Implementation and basic experiments, J. Geophys. Res., 113 (2008).

[Mathur 2007] M. Mathur, G. Haller, T. Peacock, J. E. Ruppert-Felsot, and H. L. Swinney, Uncovering the Lagrangian Skeleton of Turbulence, Physical Review Letters, 98(14), 144502–4 (2007).

[McKiver 2003] W. J. McKiver and D. G. Dritschel, The motion of a fluid ellipsoid in a general linear background flow, Journal of Fluid Mechanics, 474, 147-173 (2003).

[McLachlan 1992] R. I. McLachlan and P. Atela, The accuracy of symplectic integrators, Nonlinearity, 5, 541–562 (1992).

[Meacham 1994] S. P. Meacham, K. K. Pankratov, A. F. Shchepetkin, and V. V. Zhmur, The interaction of ellipsoidal vortices with background shear flows in a stratified fluid, Dynamics of Atmospheres and Oceans, 21(2-3), 167–212 (1994).

[Mezic 2006] I. Mezic, On the dynamics of molecular conformation, PNAS, 103(20), 7542-7547 (2006).

[Morton 1913] W. B. Morton, On the Displacements of the Particles and Their Paths in Some Cases of Two-Dimensional Motion of a Frictionless Liquid, Royal Society of London Proceedings Series A, 89, 106-124 (1913).

[Odier 2007] P. Odier, Characterization of turbulent mixing in an Oceanic Overflow Facility, Abstract submitted to DFD07 Meeting of the American Physical Society, (2007).

[Peng 2009] J. Peng and J. O. Dabiri, Transport of inertial particles by Lagrangian coherent structures: application to predator?prey interaction in jellyfish feeding, Journal of Fluid Mechanics, 623(-1), 75-84 (2009).

[Peyrard 2004] M. Peyrard, Nonlinear dynamics and statistical physics of DNA, Nonlinearity, 17(2), R1-R40 (2004).

[Poincaré 1899] Poincare, H. (1899). New Methods of Celestial Mechanics. Springer.

[Polvani 1990] L. M. Polvani, J. Wisdom, E. DeJong, and A. P. Ingersoll, Simple Dynamical Models of Neptune's Great Dark Spot, Science, 249(4975), 1393–1398 (1990).

[Richardson 2007] M. I. Richardson, A. D. Toigo, and C. E. Newman, PlanetWRF: A general purpose, local to global numerical model for planetary atmospheric and climate dynamics, J. Geophys. Res., 112 (2007).

[Rom-Kedar 1990] V. Rom-Kedar, A. Leonard, and S. Wiggins, An analytical study of transport, mixing and chaos in an unsteady vortical flow, Journal of Fluid Mechanics Digital Archive, 214(-1), 347-394 (1990).

[Rom-Kedar 1991] V. Rom-Kedar and S. Wiggins, Transport in two-dimensional maps: concepts, examples, and a comparison of the theory of Rom-Kedar and Wiggins with the Markov model of MacKay, Meiss, Ott, and percival, Phys. D, 51(1-3), 248–266 (1991).

[Sanders 2007] Sanders, J., Verhulst, F., and Murdock, J. (2007). Averaging Methods in Nonlinear Dynamical Systems. Springer.

[Sapsis 2009] H. Sapsis, Inertial Particle Dynamics in a Hurricane, Journal of the Atmospheric Sciences, In press. (2009).

[Schiermeier 2007] Q. Schiermeier, Oceanography: Churn, churn, churn, Nature, 447(7144), 522–524 (2007).

[Shadden 2005] S. C. Shadden, F. Lekien, and J. E. Marsden, Definition and properties of Lagrangian coherent structures from finite-time Lyapunov exponents in two-dimensional aperiodic flows, Physica D: Nonlinear Phenomena, 212(3-4), 271–304 (2005).

[Shadden 2007] S. C. Shadden, K. Katija, M. Rosenfeld, J. E. Marsden, and J. O. Dabiri, Transport and stirring induced by vortex formation, Journal of Fluid Mechanics, 593(-1), 315–331 (2007).

[Shadden 2008] S. Shadden and C. Taylor, Characterization of Coherent Structures in the Cardiovascular System, Annals of Biomedical Engineering, 36(7), 1152–1162 (2008).

[Smale 1967] S. Smale, Differentiable dynamical systems, Bull. Amer. Math. Soc., 73, 747–817 (1967).

[Smale 1998] S. Smale, Finding a horseshoe on the beaches of Rio, Mathematical Intelligencer, 20, 39-44 (1998).

[Solomon 2007] Climate Change 2007: The Physical Science Basis. Contribution of Working Group I to the Fourth Assessment Report of the Intergovernmental Panel on Climate Change [Solomon, S., D. Qin, M. Manning, Z. Chen, M. Marquis, K.B. Averyt, M.Tignor and H.L. Miller (eds.)]. Cambridge University Press, Cambridge, United Kingdom and New York, NY, USA.

[Surana 2008] A. Surana, G. B. Jacobs, O. Grunberg, and G. Haller, An exact theory of three-dimensional fixed separation in unsteady flows, Physics of Fluids, 20(10), 107101-+ (2008).

[Szebehely 1967] Szebehely, V. (1967). Theory of Orbits, The restricted problem of three bodies.. Academic Press.

[Szpiro 2007] Szpiro, G. (2007). Poincaré's Prize. Penguin.

[Tallapragada 2008] P. Tallapragada and S. D. Ross, Particle segregation by Stokes number for small neutrally buoyant spheres in a fluid, Physical Review E (Statistical, Nonlinear, and Soft Matter Physics), 78(3), 036308 (2008).

[Tanaka 2008] M. Tanaka and S. Ross, Separatrices and basins of stability from time series data: an application to biodynamics, Nonlinear Dynamics, (2008).

[Vellinga 2002] M. Vellinga and R. A. Wood, Global Climatic Impacts of a Collapse of the Atlantic Thermohaline Circulation, Climatic Change, 54(3), 251–267 (2002).

[Verhulst 2000] Verhulst, F. (2000). Nonlinear Differential Equations and Dynamical Systems, 2nd Ed.. Springer.

[Weber 2006] G. Weber, N. Haslam, N. Whiteford, A. Prugel-Bennett, J. Essex, and C. Neylon, Thermal equivalence of DNA duplexes without calculation of melting temperature, Nature Physics, 2, 55–59 (2006).

[Weinkauf 2007] T. Weinkauf, J. Sahner, J. Sahner, H. Theisel, H. Theisel, and H. C. Hege, Cores of Swirling Particle Motion in Unsteady Flows, Visualization and Computer Graphics, IEEE Transactions on, 13(6), 1759–1766 (2007).

[Weldon 2008] M. Weldon, T. Peacock, G. B. Jacobs, M. Helu, and G. Haller, Experimental and numerical investigation of the kinematic theory of unsteady separation, Journal of Fluid Mechanics, 611(-1), 1-11 (2008).

[Whitesides 2002] G. M. Whitesides and B. Grzybowski, Self-Assembly at All Scales, Science, 295(5564), 2418–2421 (2002).

[Wiggins 2003] Wiggins, S. (2003). Introduction to Applied Nonlinear Dynamical Systems and Chaos (Second Edition). Springer.

[Yakushevich 2004] Yakushevich, L. (2004). Nonlinear Physics of DNA. Wiley-VCH.

[Yanao 2007] T. Yanao, W. S. Koon, J. E. Marsden, and I. G. Kevrekidis, Gyration-radius dynamics in structural transitions of atomic clusters, The Journal of Chemical Physics, 126(12), 124102 (2007).